INTERROGATING THE VISCOELASTIC PROPERTIES OF TISSUE USING VISCOELASTIC RESPONSE (VISR) ULTRASOUND

Mallory Renée Selzo

A dissertation submitted to the faculty at the University of North Carolina at Chapel Hill in partial fulfillment of the requirements for the degree of Doctor of Philosophy in the Department of Biomedical Engineering in the School of Medicine.

Chapel Hill
2015

Approved by:

Caterina M. Gallippi

Paul A. Dayton

Mansoor A. Haider

Joe N. Kornegay

Timothy C. Nichols

Gregg E. Trahey

ABSTRACT

Mallory Renée Selzo: Interrogating the Viscoelastic Properties of
Tissue using Viscoelastic Response (VisR) Ultrasound
(Under the direction of Caterina M. Gallippi)

Affecting approximately 1 in 3,500 newborn males, Duchenne muscular dystrophy (DMD) is one of the most common lethal genetic disorders in humans. Boys with DMD suffer progressive loss of muscle strength and function, leading to wheelchair dependence, cardiac and respiratory compromise, and death during young adulthood. There are currently no treatments that can halt or reverse the disease progression, and translating prospective treatments into clinical trials has been delayed by inadequate outcome measures. Current outcome measures, such as functional and muscle strength assessments, lack sensitivity to individual muscles, require subjective effort of the child, and are impacted by normal childhood growth and development.

The goal of this research is to develop Viscoelastic Response (VisR) ultrasound which can be used to delineate compositional changes in muscle associated with DMD. In VisR, acoustic radiation force (ARF) is used to produce small, localized displacements within the muscle. Using conventional ultrasound to track the motion, the displacement response of the tissue can be evaluated against a mechanical model. In order to develop signal processing techniques and assess mechanical models, finite element method simulations are used to model the response of a viscoelastic material to ARF excitations. Results are then presented demonstrating VisR differentiation of viscoelastic changes with progressive dystrophic degeneration in a dog model of DMD. Finally, clinical feasibility of VisR imaging is demonstrated in two boys with DMD.

to Chris.

ACKNOWLEDGEMENTS

First, I want to thank my advisor, Dr. Caterina Gallippi. I will be forever indebted to you for introducing me to ultrasound, and for your patience and guidance throughout my graduate career. The passion you show for your research is inspiring and it has been a privilege to work with you. To my dissertation committee, Drs. Paul Dayton, Mansoor Haider, Joe Kornegay, Timothy Nichols, and Gregg Trahey, I would like to thank each of you for your time, effort, and vital feedback.

There are a number of individuals that I must acknowledge for their assistance in this project. The preclinical studies would not have been possible without Amanda Bettis, Dan Bogan, Janet Bogan, Jennifer Dow, Heather Heath-Barnett, Gayle McGhee, Dr. Kathy Spaulding, Dr. Eric Snook, Dr. Martin Styner, Dr. Jiahui Wang, and Janice Weaver. For their roles in the clinical study, thank you to Dr. Melissa Caughey, Manisha Chopra, Melrose Fisher, Dr. James Howard Jr., Regina Emmett, and Diane Meyer. Thank you also to Drs. Kathy Nightingale and Mark Palmeri for being so generous with your time and modeling expertise.

I would also like to acknowledge the members of the Gallippi lab, both past and present. Thank you for your insights, your company, and for keeping my diet coke consumption in check. Special thanks to Tomek Czernuszewicz for performing the optical experiments used in Chapters 8 and 9, and to Robert Hinson without whom I would still be waiting for my processing code to finish running.

I'm fortunate to have an amazing family that has supported me every step of the way; this dissertation is a testament to your love and unwavering belief in me. To my parents Robyn

and Bob, when you found me tracing my homework against the glass door, instead of getting mad you bought me graphics software and a light table, and for that I will always be grateful. To my sister Lindsay, you have been my biggest cheerleader since the day I was born; I would be lost without you. To my mother-in-law Sharon and brother-in-law Erick, thank you for welcoming me into the family; your love and encouragement mean the world to me. And of course, thank you to my husband Chris, who has seen me through the past 6+ years of graduate school with love and endless patience. I truly could not have done this without you and I cannot wait for what comes next.

TABLE OF CONTENTS

LIST OF TABLES

LIST OF FIGURES

LIST OF ABBREVIATIONS

6MWT	6-Minute Walk Test
ARF	Acoustic Radiation Force
ARFI	Acoustic Radiation Force Impulse
BMD	Becker Muscular Dystrophy
CK	Creatine Kinase
CNR	Contrast-to-Noise Ratio
CS	Cranial Sartorius Muscle
CV	Coefficient of Variation
DGC	Dystrophin-Glycoprotein-Complex
DMD	Duchenne Muscular Dystrophy
DOF	Depth-of-Field
FEM	Finite Element Method
FOV	Field of View
FWHM	Full Width Half Max
GAST	Gastrocnemius Muscle
GRMD	Golden Retriever Muscular Dystrophy
H&E	Hematoxylin and Eosin
HHD	Hand-Held Dynamometer
IACUC	Institutional Animal Care and Use Committee
IRB	Institutional Review Board
MHz	Megahertz
MMT	Manual Muscle Testing
MRI	Magnetic Resonance Imaging
MSD	Mass-Spring-Damper Model

MSE	Mean Squared Error
MSSER	Monitored Steady-State Excitation and Recovery
PD	Peak Displacement
PML	Perfectly Matched Layer
PRF	Pulse Repetition Frequency
PSF	Point Spread Function
QMT	Quantitative Muscle Testing
RF	Rectus Femoris Muscle
ROE	Region of Excitation
ROI	Region of Interest
RP	Run Percentage
RT	Recovery Time
SART	Sartorius Muscle
SD	Standard Deviation
SDUV	Shear Wave Dispersion Ultrasound Vibrometry
SNR	Signal-to-Noise Ratio
SSI	Supersonic Shear Imaging
ST	Semitendinosus Muscle
SWEI	Shear Wave Elasticity Imaging
SWS	Shear Wave Spectroscopy
T2w	T2-weighted
TFT	Timed Function Test
VisR	Viscoelastic Response
VL	Vastus Lateralis Muscle

CHAPTER 1

Introduction

1.1 Purpose

Affecting approximately 1 in 3,500 newborn males, Duchenne muscular dystrophy (DMD) is one of the most common lethal genetic disorders in humans.[1] The disease is caused by mutations in the dystrophin gene, which codes for the protein dystrophin, an important structural component of muscle. Muscle involvement in DMD is characterized by repetitive cycles of injury and repair that result in replacement of muscle cells by fat and fibrous tissue.[2] Boys with DMD suffer progressive loss of muscle strength and function, leading to wheelchair dependence, cardiac and respiratory compromise, and death during young adulthood.[3] There are currently no treatments that can halt or reverse the disease progression. While a wide range of treatments have been proposed in the nearly 30 years since the discovery of dystrophin, translating these prospects to clinical trials has been delayed by inadequate outcome measures.[4,5]

The purpose of this dissertation is to develop Viscoelastic Response (VisR) ultrasound - a novel, noninvasive imaging method - for detection of mechanical property changes in muscle. VisR uses acoustic radiation force (ARF) to produce small, localized displacements within the muscle. Returning echoes are processed using ultrasonic motion tracking, and the displacement response of the tissue to the ARF can be evaluated against a mechanical model. By repeating this process at a number of locations, images depicting viscoelastic properties of tissues can be formed.

While presented in the context of imaging dystrophic muscles, the work herein addresses biomechanical modeling and signal processing techniques that are relevant to many other clinical applications.

1.2 Hypothesis

To evaluate the hypothesis that **VisR ultrasound can noninvasively characterize the viscoelastic properties of soft tissue *in vivo*** the following three specific aims were addressed in this research

Aim 1. Develop, using custom finite element method (FEM) models, VisR mechanical modeling and signal processing techniques for assessing tissue viscoelasticity.

Aim 2. Demonstrate the relevance of VisR imaging for differentiating viscoelastic property with progressive dystrophic degeneration in a dog model of DMD.

Aim 3. Assess the clinical feasibility of using VisR imaging to monitor dystrophic degeneration longitudinally in one, and cross-sectionally in two juvenile males with DMD.

1.3 Overview

This dissertation encompasses the development, preclinical, and clinical elevation of a new technique for evaluating the viscoelastic properties of tissue.

This thesis is organized as follows: Chapter 2 begins with an introduction to skeletal muscle anatomy and describes the natural history of DMD. Additionally, it introduces the GRMD dog model used in Chapter 11. Chapter 3 describes the physical outcome measures currently used in DMD clinical trials, gives a brief introduction to MR imaging, and describes current efforts in developing MRI as an outcome measure for staging DMD disease progression. A brief background on ultrasound imaging is provided in Chapter 4, along with a description of ultrasound techniques that have been applied to imaging dystrophic muscles. There is also a detailed description of the fundamental concepts behind ARF and ARF-based imaging methods. In Chapter 5, VisR ultrasound is presented using the Voigt mechanical model and is demonstrated in in viscoelastic tissue-mimicking materials as well as in canine muscle, *in vivo*. The results of a pilot study in *ex vivo* muscle are presented in Chapter 6 and demonstrate that VisR's sensitivity to muscle anisotropy can be controlled by modifying the focal configuration of the ARF excitations. In Chapter 7, the mass-spring-damper model (MSD) is introduced for VisR imaging and the importance of accounting for inertia is demonstrated in FEM simulations. FEM simulations are expanded upon in Chapter 8 to investigate the impact of using an acoustic radiation force to induce displacements and determine whether VisR can generate quantitative measurements of viscoelasticity. Chapter 9 considers the impact of displacement underestimation on VisR imaging and presents a technique for using shear waves to mitigate underestimation errors. Isolation of elastic from viscous material properties relative to the magnitude of the ARF excitation is demonstrated in Chapter 10. Chapter 11 contains the results of preclinical cross-sectional and longitudinal studies of VisR imaging in affected GRMD dogs and normal controls. Chapter 12 demonstrates the clinical feasibility of VisR ultrasound in two boys with DMD. Finally, Chapter 13 presents the final conclusions of this thesis and discusses areas of future development.

CHAPTER 2

Clinical Background

Skeletal muscle makes up over 40% of the human body's mass and is crucial for function and survival.[6] In order to generate force and produce movement, skeletal muscles shorten, or contract. In Duchenne muscular dystrophy (DMD), a missing protein, dystrophin, makes muscles especially vulnerable to injury during contraction.[7] Muscles will undergo cycles of damage and repair until eventually, the muscle mass becomes replaced by fat and fibrous tissue.[2]

In order to understand the pathologic changes associated with DMD, this chapter begins with a summary of the basic anatomy of skeletal muscles and the role of dystrophin in maintaining its structural integrity. This is followed by a discussion of the clinical manifestations and progression of DMD, the experimental therapies in development, and the animal models aiding in their development.

2.1 Skeletal Muscle

Attached to the bone by tendons, skeletal muscles are responsible for voluntary movements of the body. Skeletal muscles (Figure 2.1) are encircled by the epimysium, a dense connective tissue that joins with the tendon. Internally, the muscle is composed of numerous muscle fascicles, which are separated from one another by a layer of connective tissue known as the perimysium.[8] Muscle fascicle consists of bundles of multinucleated muscle fibers which are isolated from one another by the endomysium. Within these fibers are contractile proteins

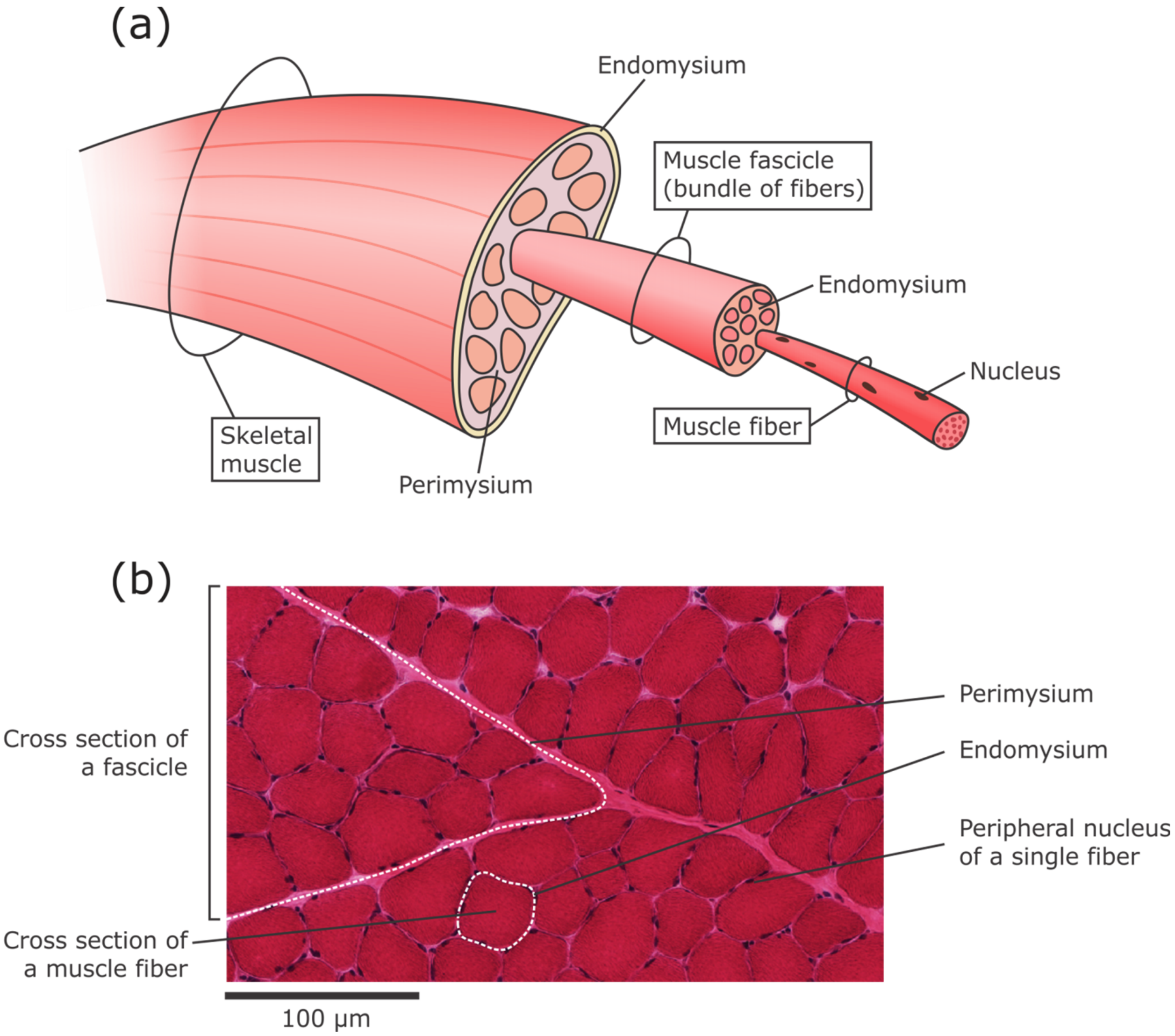

Figure 2.1: (a) Schematic drawing of the hierarchical structure of striated muscle. (b) Muscle histology stained with hematoxylin and eosin (H&E). Note the tight packing and relatively uniform diameters of the fibers, and the peripherally located nuclei. Biopsy obtained from a healthy, 3 month old dog.

called myofilaments. These proteins are responsible for the transduction of chemical energy into mechanical work during muscle contraction and relaxation.[9]

Muscle fibers make up approximately 85 percent of muscle tissue; nerves, blood supply, and connective tissue structures that provide support, elasticity, and force transmission to the skeleton constitute the remaining volume.[10] Muscle fibers are cylindrical, with a diameter ranging from about 10 µm to about 100 µm. Muscle fiber length is highly variable, depending on the muscle's architecture. Fiber arrangements fall into two major categories, parallel and pennate.[11] In a parallel arrangement, fibers run parallel to each other along the axis of the muscle, whereas fibers in the pennate arrangement insert obliquely onto a tendon that runs the length of the muscle. The geometric arrangement of fibers in the muscle has a large effect on the muscle's ability to generate force and produce movement. A muscle with parallel arrangement of fibers, for example, will have more basic contractile units in series than a similarly sized pennate muscle. This arrangement allows the parallel muscle to contract quicker, but with less force, than the pennate muscle. Muscles designed for strength (e.g. gastrocnemius) are typically pennate, whereas those designed for speed (e.g. sartorius) tend to have parallel fibers.[12]

2.1.1 Regeneration of Skeletal Muscle

Skeletal muscle contains resident stem cells called satellite cells. These cells are located between the sarcolemma of the muscle fiber and the basement membrane. Satellite cells act as a reserve population of cells that can proliferate in response to injury and regenerate muscle, as well as maintaining the number of satellite cells throughout one's life.[13]

Healthy skeletal muscle has a remarkable ability to regenerate in response to injury. In the initial phase of skeletal muscle regeneration following injury, muscle damage and disruption of muscle fiber integrity lead to an inflammatory response and an infiltration of phagocytic macrophages.[14] The macrophages persist at the injured site for several weeks removing necrotic debris. Subsequently, satellite cells are rapidly activated and then proliferate to produce committed muscle progenitor cells (myobalsts). Myogenic progenitor cells then expand and subsequently fuse with existing muscle fibers or each other to form new muscle fibers.[14]

2.1.2 Dystrophin

The structural integrity of the muscle fiber is maintained by a network of interlinking protein fibers within the muscle.[15–17] The structural protein dystrophin links the myofilaments to the plasma membrane, or sarcolemma, of the muscle fiber, as depicted in figure 2.2. Dystrophin associates which several glycoproteins to form the "dystrophin-glycoprotein-complex" (DGC), and the entire structure acts as a structural link between the contractile apparatus and the extracellular matrix, thereby stabilizing the sarcolemma during contraction and relaxation. When dystrophin is absent from muscle cells, this complex does not form, and forces are unevenly transmitted through the sarcolemma resulting in a fragile membrane that is more easily damaged during muscular contraction.[18]

2.2 Duchenne Muscular Dystrophy

2.2.1 Epidemiology and Genetics

Duchenne muscular dystrophy (DMD) results from mutations in the dystrophin gene located on the short arm of the X chromosome and is characterized by a complete absence of the dystrophin protein.[19] Becker muscular dystrophy (BMD) is a fundamentally similar disease as DMD but involves a decrease in the quantity or quality of the dystrophin protein.[20] This results in a milder and more slowly progressive course.

The dystrophin gene, which spans a genetic distance of more than 2.5 million base pairs, is the largest isolated human gene. More than 90% of DMD patients have an absence of dystrophin corresponding to a mutation that disrupts the reading frame of the mRNA, which results in the early termination of transcription.[21] As a result, an unstable dystrophin molecule is produced which will undergo rapid decay. The incidence of DMD has been estimated at approximately 1 in 3,500 male births.[19] The most common form of inheritance is X-linked recessive, but an estimated one-third of cases are spontaneous mutations with no prior family

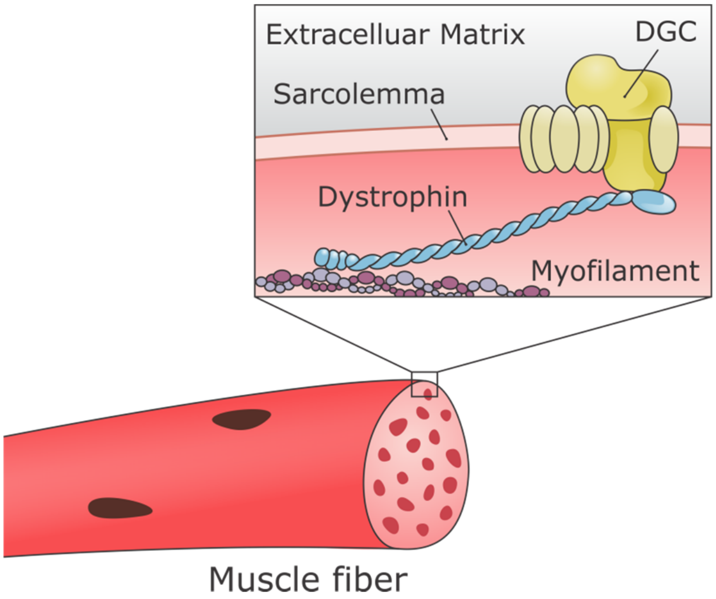

Figure 2.2: A schematic representation of dystrophin and its role in linking the myofilaments to the extracellular matrix.

history. Because the mutation is X-linked, the disease almost exclusively affects males. Females with a mutated gene are "carriers" and can pass the mutation onto her children.

2.2.2 Pathology

In DMD, the absence of dystrophin in the cell membrane will result in a fragile sarcolemma that is more easily damaged during muscle contraction. Increased membrane breakdown allows extracellular calcium to enter the cell causing the fiber to undergo necrosis.[7] As damaged muscle fibers are repaired, they still lack the missing structural component and will be torn again by future muscle activity. Following this relentless cycle of necrosis and regeneration, the proliferative capacity of the satellite cell population gradually becomes exhausted, and regeneration eventually fails.[22,23] As a result, the number of muscle fibers progressively decreases, while fibrous and fatty tissue progressively increases.

One of the most important histologic features of DMD is loss of muscle fibers. The size of individual muscle fibers displays marked variation, with fibers ranging from 10 to 230 µm. Additional histologic features include: regenerating fibers; enlarged, "hypercontracted" fibers (which may be caused by abnormally high amounts of calcium); areas of overt necrosis with macrophage infiltration; increased endomysial connective tissue; and infiltration of adipose tissue.[24,25]

Histopathology changes as a function of age, with young patients showing less fibrosis and less dramatic changes in muscle, whereas end-stage muscle shows large numbers of very small fibers that have failed to fully regenerate, extensive endomysial fibrosis, and a few remaining hypertrophic fibers.[26] No histopathologic feature is diagnostic for DMD, but immunohistochemical analysis of the muscle biopsy can show dystrophin protein content, which is considered diagnostic.

2.2.3 Clinical Diagnosis

The diagnosis of DMD is based on clinical signs and symptoms and confirmed by raised serum concentration of creatine kinase (CK), absence of dystrophin in muscle biopsy, and the finding of a mutation in the dystrophin gene. In all DMD patients serum CK, an indicator of muscle damage, is high from birth onwards.[27] The level may decline in the later stages of the disease, when the greater muscle mass has already deteriorated, and there is less breakdown of muscle mass than in the earlier stages.[28]

2.2.4 Natural History

The natural history of untreated DMD follows a predictable course. However, the disease course can be modified with aggressive pharmacologic (corticosteroids) and rehabilitation treatments. The following sequence of events occurs in both treated and untreated patients with DMD but at a later age in corticosteroid-treated boys.

Affected boys are rarely symptomatic in early infancy; however, elevated levels of serum creatine kinase (CK) enzyme are present at birth.[29,30] The most common first symptom is a delay in independent walking. Clinical evaluation is often sought when the child begins exhibiting gait abnormalities, difficulty rising from the floor, and problems climbing stairs. On average, children with DMD are diagnosed between ages 4 and 5.[31]

In general, during the early stages of the disease, the lower limbs are more affected than the upper limbs, with certain muscles more predominately affected.[27,32] This pattern of muscle involvement results in several well-defined physical features associated with the disease. Weakness of the knee and hip muscles leads to the Gowers' maneuver, in which the child rises from the floor by using his hands to "climb" up his legs. Hip extensor muscle weakness produces a waddling gait, and contractures of the achilles tendon leads to toe-walking. As the posterior hip muscles weaken, the child must arch his back when standing to maintain his center of gravity behind the hip joint leading to lumbar lordosis.[28] One of the most obvious features in the early stages of the disease is an enlargement of the calf muscles. Muscle enlargement is due, at least in part, to an excess of adipose and connective tissue.[33]

The ability to stand up from a chair is lost around age 8, followed by the inability to climb stairs.[34] The combination of muscle weakness and contractures leads to an increasing difficulty in walking. When ambulation is no longer possible, usually around age 10 in untreated DMD and about three years later in most steroid-treated DMD boys, full-time wheelchair use is required.[35–37] After loss of ambulation, joint contractures increasingly develop, particularly flexion contractures of the elbows, knees, hamstrings, and hips. Later movement of the shoulders and wrists also become limited. Cardiac and respiratory involvement often occur in this later stage of the disease.[3,38]

Patients with DMD are at risk of respiratory complications as their condition deteriorates.[39] Pulmonary function becomes compromised because of weakness of intercostal and diaphragmatic muscles. Scoliosis is common in affected boys and usually progresses more rapidly after the child becomes non-ambulatory. This thoracic deformity further compromises pulmonary capacity. DMD patients are also at risk for cardiac disease. Cardiac disease usually consists of dilated cardiomyopathy, which causes a progressive decline in the ejection fraction, and generally evolves to heart failure.[40] The mean age of death is 19 in untreated patients, with approximately ninety percent of deaths attributed to respiratory and ten percent to cardiac causes. Ventilation use extends mean life expectancy to 25.[41]

Patients can show other symptoms in addition to skeletal and cardiac muscle involvement. Intellectual impairment occurs in most patients. The IQ of boys with DMD is typically one standard deviation below the general population, but cognitive impairment is not progressive and not correlated with weakness.[42,43] Smooth muscle dysfunction is also present and can lead to digestive and urinary tract complications.[44]

2.2.5 Treatment

There is no cure for DMD. Treatment goals are to maintain function, prevent contractures, and provide psychological support for children and their families.[3] Main efforts are directed towards keeping children standing and walking as long as possible. Passive stretching exercises, use of splints to maintain the feet in a neutral position during the night, and use of long-leg braces for walking are important in this respect. Scoliosis cannot be prevented and, if progressive, surgical correction is the only effective way to straighten the spine.[28]

Corticosteroids

Daily prednisone stabilizes or improves the strength of boys with DMD and is currently the only proven treatment for the disease. DMD boys treated with prednisone from an early age generally remain ambulatory longer, have less incidence of scoliosis and contractures, and maintain normal or near-normal respiratory function.[3,37,45] Despite the evidence in favor of daily prednisone there are numerous potential side effects caused by this treatment. Most commonly seen are excessive weight gain, behavioral changes, excessive hair growth, gastrointestinal symptoms, and decreased linear growth. The synthetic steroid, deflazacort, has shown similar clinical efficacy in slowing the disease, and is thought to have fewer side effects than prednisone, particularly with regard to weight gain.[46] Deflazacort is available in Europe and Central and South America but is not currently available in the United States.

Experimental Therapies

Rather than addressing the primary defect, traditional pharmacological strategies reduce or postpone symptoms by targeting the secondary effects of the disease. Thus, there is significant interest in developing therapies for DMD that would treat the underlying genetic defect and result in the production of functional dystrophin.[47] Genetic treatments must overcome significant challenges: treatment must restore dystrophin to both skeletal and cardiac muscles, patients will need to receive treatment the entirety of their lives, and immune response must be minimized.[48]

Several therapeutic approaches are being developed, and clinical trials are in progress. Approaches currently being investigated include gene replacement of dystrophin using viral vectors, and upregulation of proteins, such as utrophin, to act as dystrophin surrogates. A number of gene-specific approaches, which manipulate mRNA processing, are also being explored. These include antisense oligonucleotides to induce exon skipping and restore the reading frame in boys with eligible out-of-frame deletions, and agents, such as aminoglycoside antibiotics, which promote the read-through of premature stop codons.[49–52]

2.2.6 Animal Models

The availability of animal models for DMD constitutes a critical asset, as they allow for extensive pre-clinical studies on the safety and functionality of the various therapeutic approaches as well as understanding the mechanism of muscle degeneration.[53] The most commonly used models are the mouse and dog model. The preclinical studies described in this dissertation were performed using the GRMD dog model.

Mouse Models

Mouse models have been used extensively to understand the pathologic mechanism of DMD and have been crucial in the development of therapeutic approaches. Many mouse models with mutations in the DMD gene have been identified. Among these models, the mdx mouse is most commonly used laboratory model of DMD.[54] The mdx mutation consists of a single base substitution in exon 23, resulting in a premature stop codon in the dystrophin gene.[55] This mutation leads to the absence of detectable dystrophin in the muscle, except in rare revertant muscle fibers. Despite being a genetic and biochemical homologue of DMD in humans, the mdx mouse exhibits a milder phenotype. Muscle pathology is comparatively moderate, and mechanical function is less seriously compromised, resulting in an almost normal lifespan.[55]

While the genetic tractability and convenient size of mice make them invaluable tools in DMD research, their inability to address certain issues associated with DMD, such as the challenges associated with performing gene or cell therapy on large volumes of muscle, and their differing pathological expression of the disease, limits their relevance for clinical evaluation in therapeutic trials. In contrast, dystrophin deficient dogs have a body size closer to humans and develop a progressive disease similar to DMD.[54]

Dog Models

Spontaneous mutations of the dystrophin gene resulting in X-linked muscular dystrophy have been identified in several breeds of dogs: Golden Retrievers, Rottweilers, Pembroke Welsh Corgis, Cavalier King Charles Spaniels, and the German Shorthaired Pointer.[56] Of these, the Golden Retriever muscular dystrophic (GRMD) dog has been the most extensively studied and best characterized.[57–65] GRMD dogs have a point mutation in intron 6 in the canine dystrophin gene, resulting in a premature stop codon, and consequentially, in a non-functional protein.[66]

Dogs with GRMD undergo a clinical progression that closely resembles human DMD. CK levels are elevated and extensive muscle necrosis can be identified in GRMD dogs from birth onwards.[67] By 6 months of age, severe fibrosis and joint contractures develop. Affected dogs have a stiff gait and tire easily. As the disease progresses, muscle contractures lead to reduced range of motion of joints, and dogs frequently develop spinal column and thoracic wall deformities. GRMD dogs frequently develop cardiomyopathy which can lead to heart failure.[56,67] The histopathological changes in the muscles are also similar to the ones seen in humans and include muscle fiber degeneration and regeneration, fiber splitting, numerous fibers with centrally located myonuclei, and intense connective tissue replacement. An important confounding factor for studies using the GRMD dog model is the high degree of variability in disease severity. Despite having the same genetic mutation, some dogs with GRMD are only mildly affected; while others die soon after birth due to extreme respiratory compromise.[56]

2.3 Summary

DMD is a devastating muscle wasting disease caused by mutations in the gene encoding dystrophin, a muscle cytoskeletal protein. The disease is characterized by progressive muscle weakness and degeneration stemming from progressive loss of contractile function. Current drug selections for DMD patients are primarily limited to corticosteroids, however, several novel treatments, aided in their development by animal models of DMD, are in early clinical trials.

CHAPTER 3

Outcome Measures in DMD

The increasing number of potential therapies for treating DMD in recent years has highlighted the need for validated outcome measures that can reliably assess possible changes following treatment. Defining proper outcome measures is crucial for demonstrating drug efficacy in clinical trials; they should have high sensitivity, and reproducibility. Despite the fact that DMD is one of the most common neuromuscular diseases, patient numbers are limited often requiring that clinical trials involve multiple trial sites, emphasizing the need for outcome measures which can be standardized between institutions.[68] Furthermore, treatment options may only result in mild improvement, so outcome measures will need to able to detect minimal changes in natural history.

Additional challenges in DMD occur due to the young age of the patient population. Obtaining reliable outcome measures in patients with DMD can be difficult because of the unique challenges inherent in testing children and because of the associated cognitive deficits seen in approximately one-third of DMD patients. Moreover, loss of muscle function in DMD occurs against the background of normal childhood growth and development, this may manifest as an improvement in physical ability despite progressive muscle impairment.[69] This chapter describes the current surrogate biomarkers for DMD currently employed in clinical trials as well as imaging techniques that are being developed for outcome measures in DMD.[70]

3.1 Physical Outcome Measures

Physical outcome including the 6-minute walk test, muscle strength tests, and timed function tests have been used in the majority of clinical trials. A limitation of these physical tests is that the measurements rely on voluntary efforts of the patient. Consistency of the measurements between trials and between test sessions can be significantly affected by the attention, cooperation, and motivation of the child.[69,71] The strengths and weaknesses of the specific physical tests are reviewed below.

6-minute walk test

The 6-minute walk test (6MWT) measures the distance that a patient can walk in a period of 6 minutes. Studies documenting the sensitivity and reproducibility of the 6MWT have led to its common use as the primary clinical endpoint in DMD trials worldwide.[72,73] Given that difficulty walking is an important manifestation of the disease process, improvements in the 6MWT with treatment relative to placebo constitutes evidence of therapeutic value. In clinical trials, a difference of 30 meters between drug and placebo is generally required for a clinically meaningful functional change.[74,75]

While the 6MWT is useful, it has a number of limitations. First, it has inherent variability; distance walked can by effected by the patient's mood and effort. Parents and clinical evaluators have observed that verbal encouragement of the child can significantly increase their distance.[76] In addition, the 6MWT can only be completed in ambulatory boys, severely limiting the length of time that the test is applicable. Moreover, children with DMD under age 7 have demonstrated yearly improvements in 6MWT distance despite progressive muscular impairment.[77] Evidence from recent trials in exon skipping has shown that early intervention may be necessary to maximize treatment before extensive muscle loss has occurred. Thus, the 6-minute walk test may not be a suitable primary endpoint in these trials moving forward.[78]

Muscle strength testing

Manual muscle testing (MMT) is a procedure for evaluating strength and function of an individual muscle or muscle group in which the patient voluntarily contracts the muscle against the manual resistance of a clinician. The clinician assigns the muscle strength a grade between 0-5 based on the on the patient's ability to hold against the applied pressure. MMT is the simplest and most common method used to evaluate muscle strength in a clinical setting. However, the questionable reliability and sensitivity of MMT limits its usefulness as an outcome measure.[79] Additionally, the nonlinearity of the grading limits the use of MMT for following disease progression or treatment response in a given patient longitudinally.

In order to overcome the limitations associated with MMT, isometric hand-held dynamometers (HHD) have been developed to provide objective and continuous measurements of muscle strength. HHDs are generally portable, relatively inexpensive, and measure strength as a unit of force. To perform quantitative muscle testing with an HHD, the patient is positioned in a standardized position for the muscle group being tested. The clinician holds the HHD stable while the patient exerts their maximum force against it for a period of 3 to 5 seconds.

The current literature indicates that HHD testing provides reliable measurement in children and adolescents with and without neuromuscular disorders.[80] However, reliability is dependent upon consistent testing techniques and protocols, and accurate positioning of the patient. Like other physical tests, muscle strength testing is critically dependent upon the effort and cooperation of the patient. It is also crucial that the patient understand the required movement. Because of these requirements, HHD testing is difficult to perform in children under 5.[71] Limitations with HHD testing also occur in later stages of the disease when severe contractures restrict the positioning of the patient.[81] Furthermore, these tests cannot isolate the behavior of an individual muscle, but rather they represent the global behavior of several muscles acting on a given joint.

Timed function testing

The measurement of the time that a child takes to perform a given activity is a commonly used means for assessing the functional abilities in boys with DMD. These activities can include the time to climb a short flight of stairs, walk a short distance, or sit and stand up from a chair. Muscle degeneration is shown as an increase in the time it takes the patient to perform the activity and generally reflect the increasing weakness of the involved muscles. These tests are convenient to use in a clinical setting, easy to administer, and result in a qualitative and continuous measure of progression. However, there is potential error in clinician timing, which may reduce the test-retest reliability of the measures.[75] Furthermore, the number of activities that the patient can perform is reduced as the disease progresses, reducing the relevance of these tests in older patients.

3.2 Imaging Techniques

3.2.1 Magnetic Resonance Imaging

Magnetic resonance imaging (MRI) is a noninvasive imaging method which uses a powerful magnet to produce high resolution images and is increasingly being used in the evaluation of disease severity in neuromuscular diseases.

Basic Physics of MRI

The signal acquired from MRI systems predominately comes from the hydrogen protons within the body, specifically, those from water and fat. All protons inherently have a nuclear “spin” and a resulting intrinsic magnetic field. In the presence of a strong external magnetic field, the interaction between the external magnetic field and the magnetic field of the proton will cause the proton to precess at a frequency directly related to the strength of the external magnetic field. The protons will also align with the external magnetic field, creating a net longitudinal magnetic vector directed along the axis of the external magnetic field.[82,83]

A radiofrequency (RF) pulse is then applied which excites the protons to a higher energy level. Simultaneously, there is a gain in the protons' phase coherence. This produces a loss of longitudinal magnetization and a gain in transverse magnetization, respectively. When the RF pulse is turned off, the excited hydrogen protons undergo relaxation back to their original lower energy level. [84] The relaxation process of the protons back into their equilibrium state occurs by two mechanisms: longitudinal (T1) and transverse (T2) relaxation. In T1 relaxation, the proton returns to its equilibrium state by transferring energy to the other nuclei in its surroundings, or lattice. This mechanism is also referred to as spin-lattice relaxation, and results in a net increase in longitudinal magnetization. T2 relaxation reflects the loss of phase coherence due to interactions between spinning protons. Also known as spin-spin relaxation, T2 relaxation leads to a net decrease in transverse magnetization.[83]

Different tissues will exhibit different T1 and T2 relaxation times. By varying the scanning parameters, images are generated so that the signal is primarily due to the T1 or T2 relaxation times of the tissue. The signal intensity of normal skeletal muscle is similar to that of water, and lower than that of fat on T1-weighted images. In T2-weighted images, the signal of skeletal muscle is lower than that of both water and fat. Table 3.1 summarizes the appearance of muscle, fat, and water in T1- and T2-weighted images. Fat suppressed images can be generated by using short τ inversion recovery (STIR) or by using a pre-saturation pulse to suppress the fat signal. Fat suppressed T2-weighted images are much more sensitive in detecting subtle muscle edema.[70,85]

Table 3.1: MRI signal characteristics of muscle components

	T1-weighted	**T2-weighted**
Water	Low to intermediate	High
Fat	High	Intermediate
Muscle	Intermediate	Intermediate

MRI in DMD

Because healthy skeletal muscle and fat exhibit very different T1 relaxation times, T1-weighted imaging is very sensitive to intramuscular fatty deposition.[86] T1 signals have been shown to be significantly higher in the muscles of boys with DMD compared to normal control.[86] T1 intensity has also been shown to increase during the course of the disease, associated with the increasing replacement of muscle by fat.[87] However, water has a T1 relaxation time that is similar to normal muscle, thus T1-weighted images are insensitive at detecting increased water in muscle, making T1-weighted images less relevant in young DMD patients. It has been hypothesized that T2-weighted images, which are sensitive to both fat and water, may be more appropriate for evaluating DMD patients early in the course of the disease, before fatty infiltration is significant.[88] Acute muscle damage, inflammation, and fat have been characterized in dystrophic muscle using T2-weighted imaging.[89]

A number of approaches have utilized MRI to measure muscle size in DMD. Muscle cross-sectional area is a quantitative measurement and can show differential involvement of muscle groups in disease progression. Researchers at the University of Florida have used muscle cross-sectional area to compare boys with DMD to age matched controls.[90] They found that muscle cross-sectional area of the calf muscles were larger in DMD patients compared with controls. In another study by the same group, tissue within the cross-sectional area was classified as contractile (muscle tissue) and non-contractile (fatty tissue) based on T1 signal intensity. Comparing 28 boys with DMD and 10 control subjects, they showed that the DMD patients had a significantly greater proportion of non-contractile tissue. The proportion of non-contractile tissue in boys with DMD was shown to increase significantly with age.[91]

Muscle size is typically calculated by manually tracing individual muscles in axial slices from T1- or T2-weighted images. Because this manual assessment is time consuming, muscles are generally only segmented in a limited number of slices. To address this need, the Neuro

Image Research and Analysis Laboratory at the University of North Carolina has recently developed a semi-automated segmentation method for segmenting the full length of individual muscles. They found that utilizing the full volume of muscle resulted in significantly less error and variability in measurements, compared to the standard, limited range, muscle segmentation.[92] Further, they showed that distribution of T2 values could be analyzed in three dimensions throughout the full muscle to provide information of muscle heterogeneity, and have demonstrated that MRI texture features are capable of distinguishing longitudinal progression between GRMD and normal dogs.[93]

Overall, MRI is a powerful and sensitive technique for evaluating skeletal muscle involvement in DMD. The major disadvantages of MRI as a biomarker for disease progression or therapeutic response in clinical trials are associated with the high cost, and the necessity of sedation or anesthesia in young children to prevent motion artifacts.[94] This is especially undesirable in this patient population as anesthesia is potentially more hazardous in boys with DMD.[95] Furthermore, MRI is not capable of directly measuring fibrosis, which is a critical characteristic of degenerated dystrophic muscle.[96]

3.2.2 Ultrasound Imaging

Medical ultrasound, discussed in detail in Chapter 4, provides a safe and relatively inexpensive alternative to the high cost of MRI. Moreover, the rapid acquisition time make ultrasound less susceptible to motion artifacts, eliminating the need for sedation in pediatric patients.

3.3 Summary

The current outcome measures primarily used in DMD include the 6-minute walk test, muscle strength tests, and timed function tests. These tests lack sensitivity to individual muscles, are dependent upon the effort and cooperation of the child, and are only applicable for a limited period of time. MRI and ultrasound imaging techniques that can noninvasively and quantitatively describe individual muscle involvement and longitudinal disease progression are emerging as new outcome measures.

CHAPTER 4

Ultrasound Imaging

Medical ultrasound is a technique for generating images of soft tissue. Because ultrasound is relatively inexpensive, portable, noninvasive, and real-time, it is attractive modality for a wide variety of clinical applications, including imaging muscles affected by neuromuscular diseases such as DMD.

4.1 Basics of Ultrasound Imaging

The major components of a basic ultrasound system are shown in Figure 4.1. Ultrasonic imaging operates by transmitting high-frequency acoustic pulses into the body. To generate this acoustic wave, computer-controlled electric voltage waveforms are applied across piezoelectric elements in a transducer array. The elements vibrate at megahertz (MHz) frequency, generating pressure waves, which emanate from the transducer surface into soft tissue. As the sound waves propagate, they are attenuated, scattered, and reflected, producing echoes from the various interfaces. The transducer receives the returned echoes, which are digitalized and sent to the receive beamformer. The beamformer combines the signals from each of the array elements and sums them, forming one signal (A-line) for each transmit pulse. Focal delays and apodization applied within the beamformers are used to independently focus and/or steer the A-lines on transmit and receive. Post-processing steps include envelope detection and compression of the beamformed signal. Typically, 2D images are presented in brightness mode

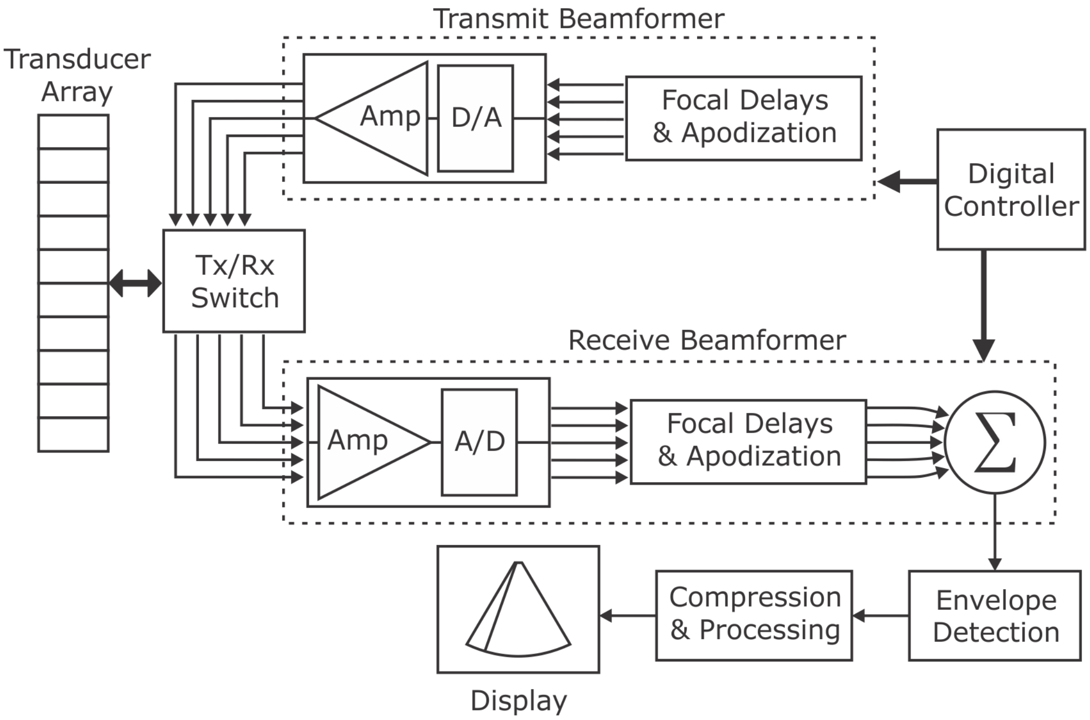

Figure 4.1: Major components of a basic ultrasonic imaging system.

(B-mode) images that depict the relative strength and location of received echoes. These images, which are made up of hundreds A-lines, are created by transmitting on a subset of the elements and translating the active aperture across the transducer array.[97,98]

4.1.1 Spatial Resolution

Spatial resolution describes the minimum spacing needed between two reflectors to have them distinguishable in the image. Image resolution can be described in the axial, lateral, and elevational dimensions as depicted in figure 4.2. Axial resolution, or the resolution along the ultrasound beam, is dependent on the pulse duration of the transmitted pulse and is defined as

$$Axial\ Resolution = \frac{\lambda \cdot n_c}{2} \tag{4.1}$$

where λ is the wavelength of the pulse and n_c is the number of cycles of the ultrasound pulse.

The lateral and elevational resolution are determined by the λ, the acoustic focal distance (z), and the width of source aperture (D) in the lateral or elevation dimension, respectively, as given by equation 4.2. The ratio of the focal distance to the aperture width is known as the f-number (F/#), and describes the focal configuration or spatial geometry of the acoustic pulse. Typically, for a 1D imaging linear array transducer, the F/# in the lateral dimension can be adjusted for the specific application by changing the number of elements excited (to change D) and the focal delays applied to them (to change z). However, the focusing in the elevational dimension is accomplished by a mechanical lens, thus the F/# is fixed and dependent on the specific transducer.

$$Lateral/Elevational\ Resolution = \frac{\lambda \cdot z}{D} = \lambda \cdot F/\# \tag{4.2}$$

$$F/\# = \frac{z}{D} \tag{4.3}$$

Depth-of-field (DOF), illustrated in figure 4.3, is another parameter used for describing the focal configuration of the acoustic pulse, and is defined by the following equation,

$$DOF = 8 \cdot (F/\#)^2 \cdot \lambda \tag{4.4}$$

The DOF describes the axial distance over which the acoustic beam maintains its approximate focal size. Consequently, for a small F/# the resolution at the focal depth will be good, but the distance over which this focusing is maintained will be small.

From equation (4.1) and (4.2), it is clear that resolution in all three dimensions is closely related to the wave length of the acoustic wave. As frequency and wave length are inversely

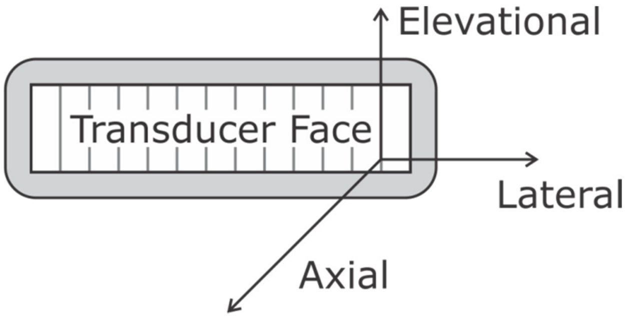

Figure 4.2: Ultrasound coordinate system relative to the imaging transducer. A standard imaging slice represents the axial-lateral plane.

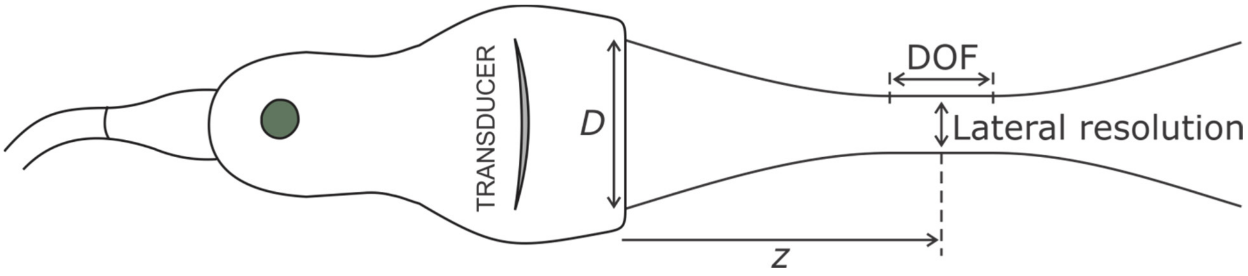

Figure 4.3: Relationship between the aperture width (D), the focal depth (z), lateral resolution, and depth of field (DOF). The DOF describes the axial distance over which the beam maintains its lateral resolution; it gets shorter for more tightly focused beams.

proportional ($f = c/\lambda$ where f is frequency and c is the speed of sound in the medium), the use of a higher frequency will produce better spatial resolution. However, depth dependent attenuation of acoustic waves also increases with an increasing frequency. This tradeoff between depth penetration and spatial resolution must be considered for each ultrasound application.

4.2 Ultrasound in DMD

Under normal circumstances, skeletal muscle tissue has low echogenicity (Figure 4.4 (a)). Perimysial connective tissue between fiber bundles are depicted as echogenetic lines on longitudinal scans (transducer parallel to muscle fibers) and small spots in transverse scans (transducer perpendicular to muscle fibers), giving the muscle a speckled appearance. The epimysium surrounding the muscle is highly echogenic, clearly demarcating the muscle boundaries. Bones are highly reflective, resulting in well-defined, hyperechoic lines with posterior acoustic shadowing.

Ultrasound can detect pathology and characterize the pattern of muscle involvement in skeletal muscle. In DMD, muscle appears more echogenic due to the increase in the fat and fibrous content in the muscle (Figure 4.4 (b)). Attenuation also increases, resulting in a decreased reflection from the underlying bone and poorer visualization of deep tissue. As the disease progresses, muscle signal increases, and the bone echo become less defined and bright, and eventually cannot be visualized.

Visual detection of increased muscle echogenicity in DMD can be difficult, and its accurate interpretation depends on the experience of the observer. To overcome this problem, techniques are being developed to make quantitative measurements of muscle echogenicity. Quantification of muscle echogenicity can be achieved with simple gray scale analysis of detected ultrasound data. Another quantification technique, backscatter analysis, converts gray-scale values to decibels by comparing measured echo intensity with phantom measurements. Both gray-scale analysis and backscatter analysis have shown a significant increase in the echo intensity of the muscles of DMD boys compared to healthy controls.[99,100] Both techniques were also sensitive to increases in intensity corresponding to patient severity. Other studies using radio frequency (RF) data with an entropy-based signal receiver have shown larger scatterer sizes in DMD versus control muscles, consistent with the pathologic changes of muscle.[101,102] These techniques show promise in assessing degradation of dystrophic muscles; however, while they are sensitive to both fibrous and fatty deposition, they are unable to distinguish between them.

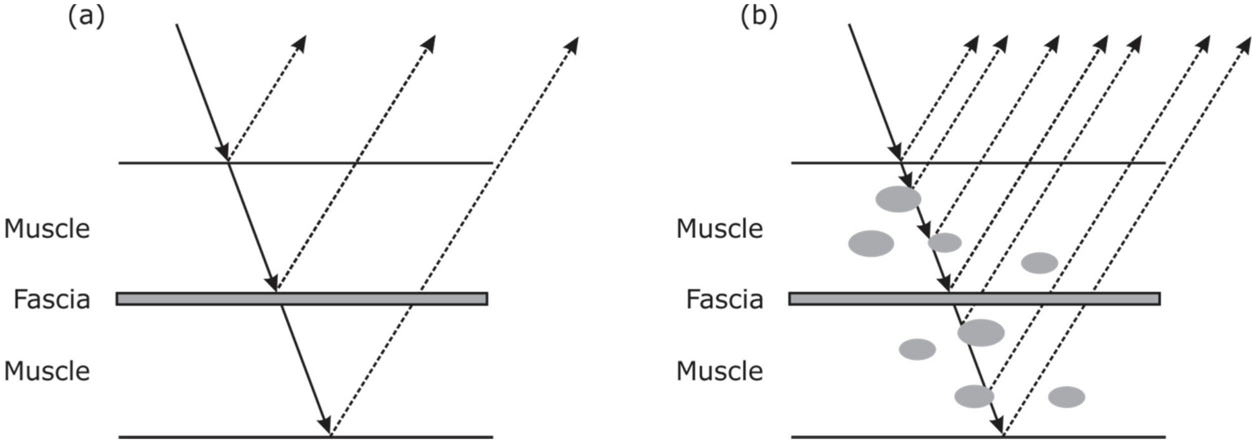

Figure 4.4: The interaction between the ultrasound beam and (a) normal and (b) dystrophic muscle. When the ultrasound beam encounters the transition from muscle to fascia, a part of the sound is reflected. Because normal muscle contains little fibrous tissue, only a few reflections occur, resulting in relatively low echogenicity. In DMD, muscle tissue is replaced by fat and fibrous tissue, resulting in many transitions with different acoustic impedance and increased reflection of the ultrasound beam.

4.3 Ultrasound Elasticity Imaging

Unlike conventional B-mode ultrasound imaging that differentiates features with dissimilar acoustic properties; elasticity imaging methods differentiate features and/or structures with different mechanical properties. Because malignancies and pathologies, such as fat and fibrosis, will exhibit different mechanical properties than the surrounding tissue, elasticity imaging methods are being developed to examine tissue health and monitor disease progression. To do this, these methods involve the exciting of the soft tissue and then monitoring the deformation response. The source of the excitation used to produce the tissue deformation can be applied externally, as in compressive elastography, or can be generated internally using radiation force.

4.3.1 Compressive Elastography

External methods apply a compressive force on the skin to deform the tissue beneath. This is often implemented by pressing down and holding the ultrasound transducer against the skin. A map of tissue strain can be formed by comparing RF data pre and post compression.[103] By assuming the applied stress is uniform and the material is elastic, differences in the measured strain are attributed to differences in the elasticity of the tissue.

Ultrasound elastography has demonstrated promising clinical applications for evaluating thyroid, breast, lymph nodes, and prostate lesions.[104] Elastography has also been applied to muscle disease assessment. In a case report of a patient with Bethlem myopathy, a congenital muscular dystrophy, elastography showed that hyperechoic areas of the affected muscle exhibited lower strain than the normal appearing tissue, a finding suggesting increased stiffness due to the presence of fibrosis in the affected areas.[105]

Elastography is intuitive and can be performed in real-time. Unfortunately, tissue compression causes signal decorrelation, limiting the accuracy of displacement estimates and the strain estimates formed from them. Elastography is also limited because the deformation field decreases with depth, making it difficult to make measurements in deep tissue. Furthermore, in compressive elastography where pressure is applied by using a free-hand technique the measurements are operator dependent, which might affect reproducibility.[106,107]

4.3.2 Acoustic Radiation Force

Rather than applying stress at the skin surface, Acoustic Radiation Force (ARF) based methods generate a localized stress field within the tissue.

Theory

As an acoustic wave propagates through a medium its intensity decreases, or attenuates, with increasing distance. Attenuation of ultrasound beams is caused by the reflection and scattering of waves and by the absorption of ultrasonic energy. This absorption of energy from the traveling wave results in the transfer of momentum and generates a body force, known as an acoustic radiation force (ARF).[108] In a medium such as soft tissue, the majority of attenuation is due to absorption. By assuming that tissue behaves as an incompressible, linearly viscous fluid at ultrasonic frequencies and that the ultrasound wave propagates as a plane wave, the magnitude of the radiation force (F) can be described as

$$F = \frac{2\alpha I}{c} \tag{4.5}$$

where α (m^{-1}) and c (m/s) are the absorption coefficient and speed of sound in the medium, respectively, and I (W/cm^2) is the temporal average intensity of the acoustic beam at a given spatial location.[109,110] The volume and geometry of the force field is spatially distributed under the active transducer aperture and is dependent on the material properties and characteristics of the transmitted beam. The geometry of a typical radiation force field is shown in Figure 4.5.

In conventional ultrasound imaging, the magnitude of the acoustic radiation force is relatively small, producing negligible displacements in tissue (< 1 μm). To generate measurable displacements, ARF methods use longer and/or higher intensity acoustic pulses than what is used for B-Mode imaging. In practice, acoustic radiation force magnitudes on the order of dynes can produce displacements in the range of 1-10 μm. The amount the tissue displaces and the time needed for the subsequent recovery are dependent upon the mechanical properties of the tissue, which is exploited in the imaging techniques described in later sections.

Acoustic Radiation Force Impulse (ARFI) Imaging

In Acoustic Radiation Force Impulse (ARFI) imaging, ultrasound is used to induce displacement and then monitor the tissue response in the same lateral location, or region of excitation (ROE). Because the measured response is dependent on the magnitude of the radiation force, which is unknown *in vivo*, ARFI methods generally only provide relative measures of the tissue mechanics.

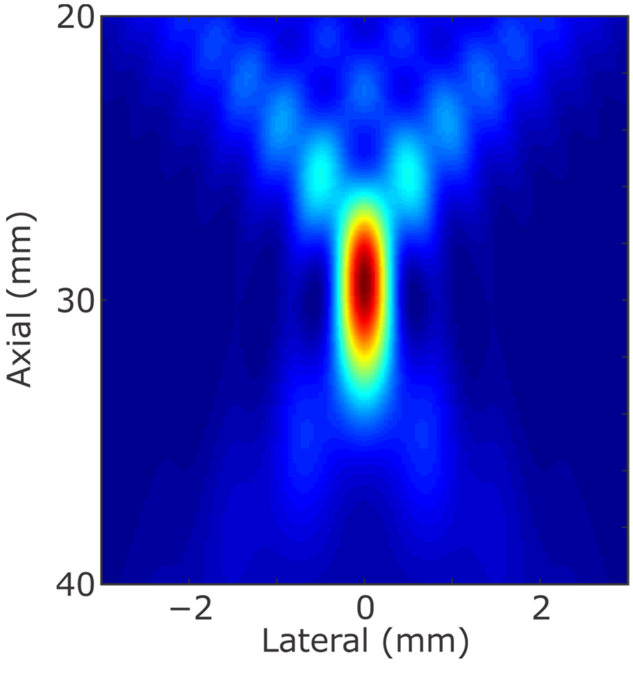

Figure 4.5: Field II generated 2D (axial versus lateral) image of the temporal average intensity of a 192 element, linear array transmitting a 300-cycle pulse at 4.21 MHz, and focused at 30 mm. From equation 4.5, assuming a constant absorption coefficient and speed of sound, the geometry of the acoustic radiation force field is the same as the intensity.

A typical ARFI imaging sequence consists of three pulse types: reference pulses are used to establish a baseline position prior to the acoustic radiation force; an excitation (push) pulse, typically between 30 μs to 1 ms in length, is used to generate the acoustic radiation force; and finally, tracking pulses applied immediately following the pushing pulse are used to monitor the deformation response and recovery of the soft tissue. This ensemble of reference, pushing, and tracking pulses can be translated across the aperture, as in B-Mode imaging, to acquire information throughout the field-of-view. A displacement estimation method, such as normalized cross correlation, can be applied to calculate axial displacements between two pulses. By estimating the displacements from a reference pulse to each of the tracking pulses, a data set of displacement though time can be generated. From this data set, parametric images can be created by analyzing properties of the individual displacement profiles, such as the peak ARFI-induced displacement, the time to peak displacement, and the time to 67% recovery from peak ARFI-induced displacement or recovery time. In general, softer regions will displace farther, take longer to reach a maximum displacement, and recover more slowly than stiffer tissues.[111–113]

ARFI imaging has been shown to be clinically useful in a variety of applications including breast,[114] atherosclerotic arteries,[115] gastrointestinal tract,[116] liver, [117] kidney, [117] and prostate.[118] Nightengale et. al. demonstrated ARFI *in vivo* in the human vastus medialis muscle and showed that muscle stiffness increased with increasing isometric loading.[119] Specifically, they showed that the peak displacement, the time to reach peak, and the time to recovery decreased with the increasing load.

Shear Wave Imaging

Along with localized displacement within the region of ultrasonic beam propagation, an ARFI excitation produces shear waves that propagate perpendicularly to the direction of the ultrasound wave propagation. The phase velocity of generated shear waves has been shown to be related to the stiffness of the material. In a homogeneous, linear, elastic medium, the speed of the shear wave (c_T) can be expressed as

$$c_T = \sqrt{\frac{G}{\rho}} = \sqrt{\frac{E}{2(1+\upsilon)\rho}} \tag{4.6}$$

where G is the shear modulus, E is the Young's modulus, υ is the Poisson's ratio, and ρ is the density of the tissue. Shear Wave Elasticity Imaging (SWEI) uses an impulse radiation force to generate shear waves and quantify tissue stiffness based on their propagation speed. As with ARFI, SWEI imaging sequences consist of reference, pushing, and tracking pulses, except unlike ARFI, the tracking beams are positioned outside the ROE. With the displacement through time information at multiple lateral locations separated by a known distance from the pushing pulse, the speed of the propagating shear waves can be estimated.[120]

In Supersonic Shear Imaging (SSI), multiple acoustic radiation force excitations are applied at increasing focal depths to create a quasi-plane shear wave source. The method relies on applying the excitations such that shear waves propagating away from the ROE sum constructively to create an axially extended cylindrical shear wave. Utilizing extensively parallel beamforming and plane wave transmits SSI methods are capable of monitoring the deformation response simultaneously across a large field of view (FOV) at ultrafast frame rates. Quantitative estimates of tissue stiffness are made from measured shear wave speeds.[121]

Clinically, shear wave imaging has been utilized for detecting breast cancer lesions,[122] monitoring liver fibrosis,[123] and for assessing thermal ablations.[124] Gennisson et al. demonstrated that shear wave imaging was sensitive to muscle anisotropy, and found that shear waves traveled four times faster along muscle fibers than across them in a human bicep muscle.[125] Lacourpaille et al. and Dastgir et al. both investigated shear wave imaging in boys with DMD and found an increase in velocity in the muscles of affected boys compared to healthy control.[126,127]

Viscosity

Conventional elasticity methods have largely ignored viscous losses, considering tissue to be purely elastic. All biologic tissues, however, exhibit some combination of elastic and viscous characteristics in response to an applied force. Viscosity is a measure of a material's resistance to flow or deformation, and if ignored, can bias the estimates of elasticity.[128] Therefore, a viscoelastic model is more appropriate for describing soft tissue deformation. Recently, a number of groups have developed methods for estimating the viscosity of tissue. In Shear Wave Dispersion Ultrasound Vibrometry (SDUV) repeated radiation forces pushes are used to generate harmonic shear waves.[129] Elasticity and viscosity are derived by measuring shear wave velocities at multiple frequencies and fitting to a mechanical model. Catheline et al. measured viscoelastic properties by analyzing the speed and attenuation of a transverse waves generated by an external mechanical plate vibrator.[130] Shear Wave Spectroscopy (SWS) uses a broad-band, quasi-plane shear wave source to induce displacements.[131] To assess viscous dispersion, the method applies Fourier transforms to the propagating shear waves and evaluates the phase difference as a function of frequency. Because these methods all rely on shear wave propagation, they all assume homogeneity over a millimeter-scale measurement region, and lack the ability to access the viscoelastic properties directly in the ROE.[132]

Other approaches to viscoelastic property assessment within the region of excitation apply sustained stress to induce displacements and solve for elastic and viscous parameters using established viscoelastic models. Monitored Steady-State Excitation and Recovery (MSSER) ultrasound intersperses multiple ARF pulses and tracking pulses to observe tissue as it displaces to a steady-state level, then monitors the recovery of the tissue following the cessation of force. Tissue displacement and recovery can be fit to a mechanical model to quantify the mechanical parameters.[133] However, MSSER may suffer from slow frame rate and/or undesired bioeffects from the duration and amplitude of ARF excitations necessary to achieve steady-state displacement under physiologically relevant conditions.

4.4 Summary

This chapter described the fundamental concepts underlying medical ultrasound imaging. These principles are applied to study muscle in the context of muscular dystrophy. A brief review of ultrasound-based elasticity imaging methods including compressive elastography and acoustic radiation force is also provided. In addition, the need for considering biological tissues as viscoelastic rather than purely elastic was presented.

CHAPTER 5

Viscoelastic Response (VisR) Ultrasound

5.1 Introduction

As discussed in Section 4.3.2, monitored steady-state excitation and recovery (MSSER) is a method developed by Mauldin et al. that uses acoustic radiation force (ARF) to simulate a material creep test.[133] In MSSER, many successive ARF impulses are applied to fully displace tissue to a steady-state level. The observed displacement and subsequent recovery are then fit to the Voigt or standard linear viscoelastic model to estimate the mechanical parameters of the material. However, due to the duration and amplitude of ARF excitations necessary to achieve steady-state displacement in an *in vivo* environment, MSSER may suffer from slow frame rate, motion artifacts, and/or undesired heating.

Viscoelastic Response (VisR) ultrasound is a faster alternative to MSSER which assesses the viscoelastic properties of tissue using two successive ARF impulses and monitoring induced displacements in only the region of ARF excitation. In this chapter VisR methods are mathematically derived using the Voigt viscoelastic model and are demonstrated in viscoelastic tissue-mimicking materials as well as in canine muscle, *in vivo*, with spatially matched histochemical validation.

© 2013. Portions reprinted, with permission, from Selzo, M. & Gallippi, C. Viscoelastic Response (VisR) Imaging for Assessment of Viscoelasticity in Voigt Materials. IEEE Trans. Ultrason. Ferroelectr. Freq. Control 60, 2488–500 (2013).

5.2 Background

Viscoelastic Creep

Viscoelasticity is the property of materials that exhibit both viscous and elastic characteristics when undergoing deformation. Biological tissues exhibit a significant amount of viscoelastic, or time-dependent, behavior, such as creep. Creep describes a progressive deformation of a material when exposed to a constant force over time. In a creep test, the displacement will tend towards a constant, or steady-state value, as illustrated in Figure 5.1. When the force is removed, the material will undergo progressive recovery. The creep and recovery response of a viscoelastic material is time dependent and related to the characteristic recovery time parameter, or τ, of the material.[134]

VisR Ultrasound

Rather than pushing the tissue fully to steady-state, as in MSSER, VisR assesses viscoelasticity by observing only a short portion of the viscoelastic creep profile predicted by the

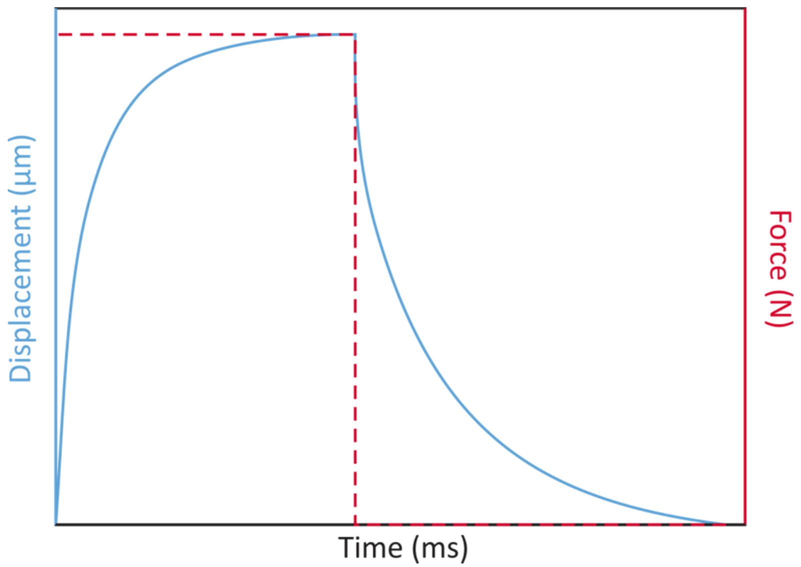

Figure 5.1: Creep behavior. If a constant force is instantaneously applied to a viscoelastic material (red), the resulting displacement will increase (or creep) over time (blue) until reaching a steady-state level of displacement.

Voigt model. The Voigt model is a mechanical model that describes the response of a viscoelastic medium to external stimuli[135] and has been used extensively in literature to characterize the mechanical properties of soft tissue, including muscle tissue.[129,136–138] The model consists of an elastic spring in parallel with a viscous damper. The constitutive relation between the applied force, F(t), and displacement, x(t), in the Voigt model is a linear first order differential equation, given by:

$$\eta \frac{d}{dt} x(t) + \mu x(t) = F(t) \tag{5.1}$$

where η is the coefficient of viscosity of the damper and μ is the elastic constant of the spring. This can be rewritten as:

$$x(t) + \tau \frac{d}{dt} x(t) = \frac{F(t)}{\mu} \tag{5.2}$$

where τ is the relaxation time constant for constant stress of the material, and is equal to the ratio of viscosity to elasticity.

Acoustic radiation force can be used to apply a step-stress input that causes creep in a viscoelastic medium. If the ARF excitation is described as a rectangular function of force magnitude A and t_{ARF} duration, then the two ARF excitations can be described as two rectangular pulses of duration t_{ARF} and amplitude A, and separated by t_s in time, and are defined as below:

$$F(t) = A\big(H(t) - H(t - t_{ARF})\big) + A(H(t - t_{ARF} - t_s) - H(t - 2t_{ARF} - t_s)) \tag{5.3}$$

where $H(t)$ is the Heaviside unit function and is given by:

$$H(t) = \begin{cases} 0, & t < 0 \\ 1, & t \geq 0\,. \end{cases} \tag{5.4}$$

Substituting (5.3) into (5.2) yields:

$$x(t) + \tau \frac{d}{dt} x(t) = s\big(H(t) - H(t - t_{ARF})\big) + A(H(t - t_{ARF} - t_s) - H(t - 2t_{ARF} - t_s)) \tag{5.5}$$

$$s = \frac{A}{\mu}. \tag{5.6}$$

Equation (5.5) can be solved for displacement as a function of τ, and s. Displacement versus time profiles can be fit using to this equation using nonlinear regression in order to generate estimates of these two parameters. Figure 5.2 (a) depicts the tissue response to the two ARF excitations.

An alternative approach to assessing τ exploits only one ARF excitation (as in ARFI). The differential equation describing the response of the Voigt material to a single ARF excitation is described by:

$$x(t) + \tau \frac{d}{dt} x(t) = s\big(H(t) - H(t - t_{ARF})\big). \tag{5.7}$$

The performance of VisR using two pushes and (5.6) to estimate τ versus using one push and (5.7) to estimate τ will be compared.

5.3 Methods

Imaging was performed using a Siemens Acuson Antares imaging system (Siemens Medical Solutions USA, Inc., Ultrasound Division), which has been adapted to provide users with the ability to modify acoustic beam sequences, and a VF7-3 linear array transducer. ARF excitations were 300 cycles (tARF = 70 μs) in duration centered at 4.21 MHz with an F/1.5 focal configuration and 6.5 mm depth of field. Tracking pulses were conventional B-mode beams centered at 6.15 MHz with an F/1.5 focal configuration and 11 kHz pulse repetition frequency. VisR beam sequences consisted of two reference tracking lines preceding a first ARF excitation, then 4 tracking lines followed by a second ARF excitation and 40 additional tracking lines.

For comparative purposes, MSSER, conventional ARFI, and single-push VisR imaging were also performed. The MSSER beam sequence consisted of two reference tracking pulses, followed by 30 ten-cycle ARF excitations interspersed by 30 tracking pulses for a total of 62 pulses (5.64 ms). Conventional ARFI imaging was performed with a beam sequence that used the same excitation and tracking beams described for VisR, but with only one ARF excitation followed by an ensemble of 59 tracking lines for a total of 62 pulses. Double-push VisR, MSSER, and ARFI beam sequences are illustrated in Figure 5.2 (b).

Two-dimensional imaging was achieved by administering the VisR, MSSER, or ARFI beam sequence in 40 lateral locations evenly spaced across a 2-cm lateral field of view. Frame rates for 2-D double-push VisR, MSSER, ARFI, and single-push VisR imaging were 27.3, 4.4, 4.4, and 31.2 frames per second, respectively. Immediately before each 2-D data acquisition, a B-mode frame was acquired. RF echo data were acquired at a 40 MHz sampling frequency and transferred to a computation workstation for processing and analysis. Displacement tracking in the region of excitation was performed using 1-D cross-correlation in the axial dimension between sequentially acquired tracking lines.[139] Each tracking line was up-sampled using cubic spline interpolation by a factor of 4 and divided into a series of 80-μm search regions; the location of the peak in the cross-correlation function between a 38-μm kernel in the first

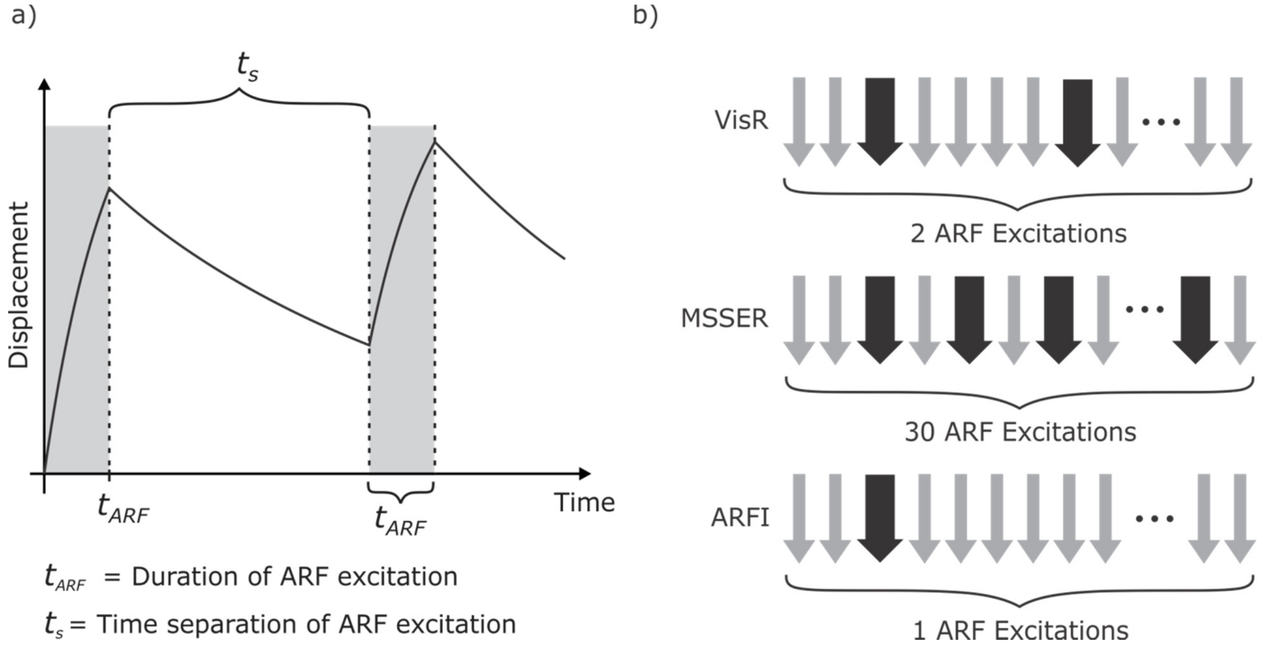

Figure 5.2: (a) Illustration of displacement versus time profile of a Voigt material in response to two ARF excitations. (b) A VisR beam sequence is illustrated in comparison to MSSER and conventional ARFI beam sequences. The large black arrows represent ARF excitation pulses, the gray arrows represent tracking pulses, and the pulses are separated in time by the pulse repetition period.

tracking line and a search region in the next tracking line was used to estimate axial tissue displacement in that region.

VisR and MSSER imaging were performed in six cylindrical (6.5 cm diameter × 6 cm height), homogeneous tissue-mimicking phantoms, and VisR and ARFI were performed in one structured (spherical inclusion) tissue-mimicking phantom (10 cm diameter × 6 cm height). The background and inclusion had comparable elasticities, but the inclusion had increased viscosity. Phantom gelatin and xantham gum concentrations were varied to alter elasticity and viscosity, respectively,[140] and were prepared as follows: 200 mL of deionized water was heated to 60°C then gelatin (Type A, Acros Organics, Geel, Belgium) was added and stirred until clarified. 5.5 mL of surfactant (Photo-flo 200, Kodak, Rochester, NY), to minimize air bubbles, and 0.65 mL of N-propanol (Fisher Scientific, Waltham, MA), to increase sound speed, were added. When the mixture had cooled to 40°C, 2 g of agar powder (Fisher Scientific) for ultrasound scattering was added. At this point, 1 g of xanthan gum (Spectrum Chemicals & Laboratory Products, New Brunswick, NJ) was added to viscous phantoms and stirred until fully dispersed. The solution was then poured into a mold for cooling and congealing overnight to room temperature. Phantom gelatin and xantham gum formulations are reported in Table 5.1.

MSSER estimates of τ were found by fitting MSSER displacement profiles to the equation for creep displacement[133]

$$x(t) = s\left(1 - e^{-t/\tau}\right) \tag{5.8}$$

using nonlinear regression. Mean and standard deviations of MSSER τ were measured in a 20 mm lateral by 4.5 mm axial region. In addition, a normalized mean displacement profile was found by averaging measured displacements in this region at each time point, and dividing by the maximum mean displacement.

For VisR imaging, τ was estimated using double- and single-push pulse sequences from the measured axial displacement profiles using (5.5) and (5.7), respectively. Parametric images of τ were rendered. In homogeneous phantoms, VisR τ mean and standard deviation were calculated in a 20 mm laterally by 4.5 mm axially region positioned just above the focal depth (24 mm). The VisR τ estimates were then statistically compared with the MSSER-derived τ values using paired t-tests. In addition, predicted normalized creep displacement curves were generated from (5.9) using the VisR-derived values of τ and an *s* of 1. These VisR-predicted curves were compared with the MSSER-observed normalized mean displacement profiles by calculating an R^2 value. In the structured phantom, parametric images of double-push VisR τ, ARFI displacement (PD) and time to 67% recovery (RT), and single-push VisR τ were generated. Contrast-to-noise ratio (CNR) for the spherical inclusion was calculated as

Table 5.1: Phantom formulations

Phantom Number	**Gelatin Concentration (g/liter)**	**Xanthan Gum Concentration (g/liter)**
1	266	0
2	82	0
3	165	0
4	82	5
5	165	5
6	266	5

$$CNR = \frac{|\mu_i - \mu_b|}{\sqrt{\sigma_i^2 + \sigma_b^2}} \tag{5.9}$$

where μ_i and μ_b denote the means and σ_i and μ_b denote the standard deviations of the parameter inside and outside the inclusion, respectively. CNR versus distance from the imaging focus (34 mm) resulting from single- and double-push VisR τ versus ARFI PD and RT parameters were compared using 3 mm lateral by 1 mm axial kernels inside and outside the lesion at each depth.

Using the same imaging methods as in the phantom experiments, double-push VisR imaging was performed *in vivo* in the right semitendinosus (ST) muscle of an approximately 13-

kg golden retriever cross-bred dog with no known musculoskeletal disorders. The Institutional Animal Care and Use Committee (IACUC) of the University of North Carolina at Chapel Hill approved all procedures. The dog was premedicated with acepromazine maleate (0.2 mg/kg), butorphanol (0.4 mg/kg), and atropine sulfate (0.04 mg/kg), masked, and then intubated and maintained with isoflurane. For imaging, the anesthetized dog was positioned in lateral recumbency. The muscle was imaged in a plane approximately transverse to the muscle fiber orientation, and the imaging plane was marked with methylene blue dye injected under B- mode image guidance.[141] The methylene blue dye was visible both macroscopically at necropsy and microscopically after sectioning and staining and did not interfere with histochemical processing. The marking was used to spatially align histological sections to the imaging plane. The extracted, marked sample was frozen, embedded, sectioned, and stained with hematoxylin and eosin, Oil Red O for fat, and Masson's trichrome for collagen. Microscopy of the stained sections was performed using an Aperio Scanscope microscope (Vista, CA) at 20× magnification. Microscopy and parametric double-push VisR τ images were aligned using the methylene blue dye as a fiducial marker and spatially compared.

5.4 Results

Representative double-push VisR profiles of axial displacement versus time observed in viscoelastic phantoms are illustrated in Figure 5.3. Figure 5.3 (a) shows profiles measured in phantoms with different elasticity but comparable viscosity (phantoms 3 and 1 in Table 5.1), whereas Figure 5.3(b) depicts profiles measured in phantoms with comparable elasticity but different viscosity (phantoms 3 and 6 in Table 5.1). The associated double-push VisR τ estimates for each profile are listed.

Representative profiles of axial displacement versus time for ARFI and VisR in a viscoelastic phantom (phantom 4 in Table 5.1) are shown in Figure 5.4. Figure 5.4(a) shows ARFI and single-push VisR profiles taken at the focal depth (24 mm), profiles 15 mm above the

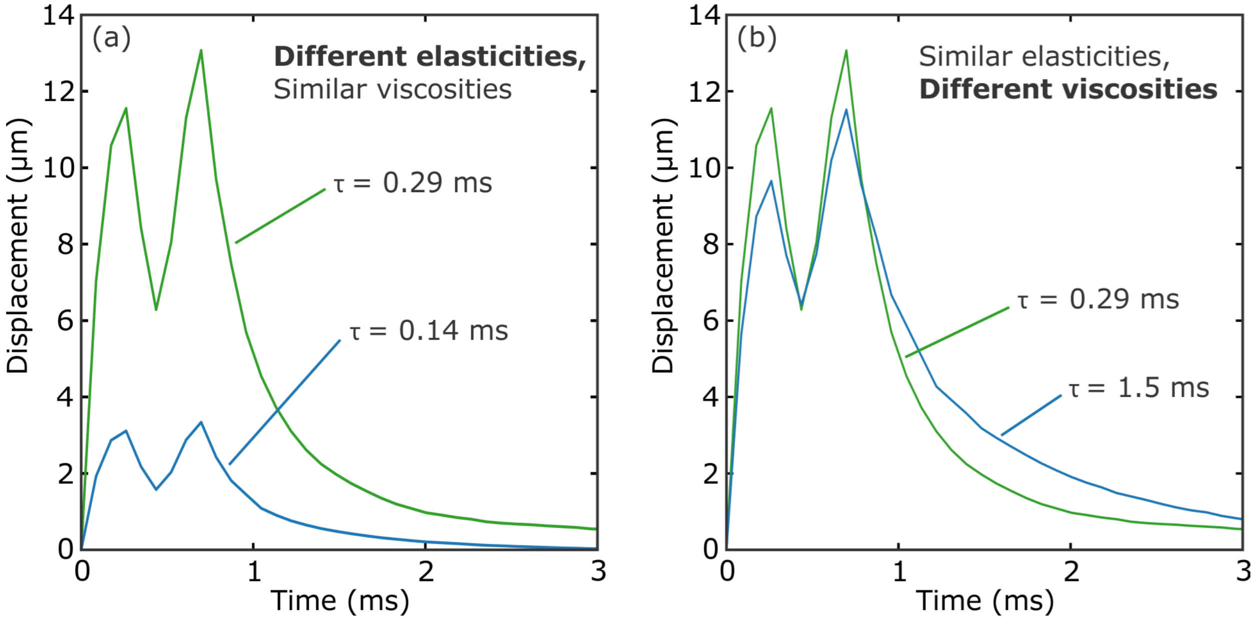

Figure 5.3: Representative double-push VisR one-dimensional axial displacement profiles measured in homogeneous tissue mimicking phantoms. In panel (a), phantoms have different elasticities, but similar viscosities (green: phantom 3, blue: phantom 1). In panel (b), phantoms have similar elasticities, but different viscosities (green: phantom 3, blue: phantom 6).

focal depth, and 5 mm below the focal depth, whereas Figure 5.4(b) shows the corresponding double-push VisR profiles at the three depths. The associated ARFI PD and RT as well as VisR τ estimates are listed at each axial depth.

In Figure 5.5 (a), double- and single-push VisR τ estimates (circles and diamonds, respectively) for all 6 homogeneous tissue-mimicking phantoms are plotted in comparison to the corresponding MSSER τ estimates (triangles). Double-push VisR τ estimates are not statistically significantly different from those generated MSSER ($p < 0.02$). However, single-push VisR τ values statistically differ from those of MSSER in phantoms 2 and 4. The agreement between VisR and MSSER τ measurements is further illustrated in Figure 5.5(b), in which VisR τ values are used to predict creep displacement curves and are plotted against the creep displacement curves observed experimentally using MSSER in each of the 6 phantoms. The accuracy of the VisR method is indicated by the closeness of fit between the experimental

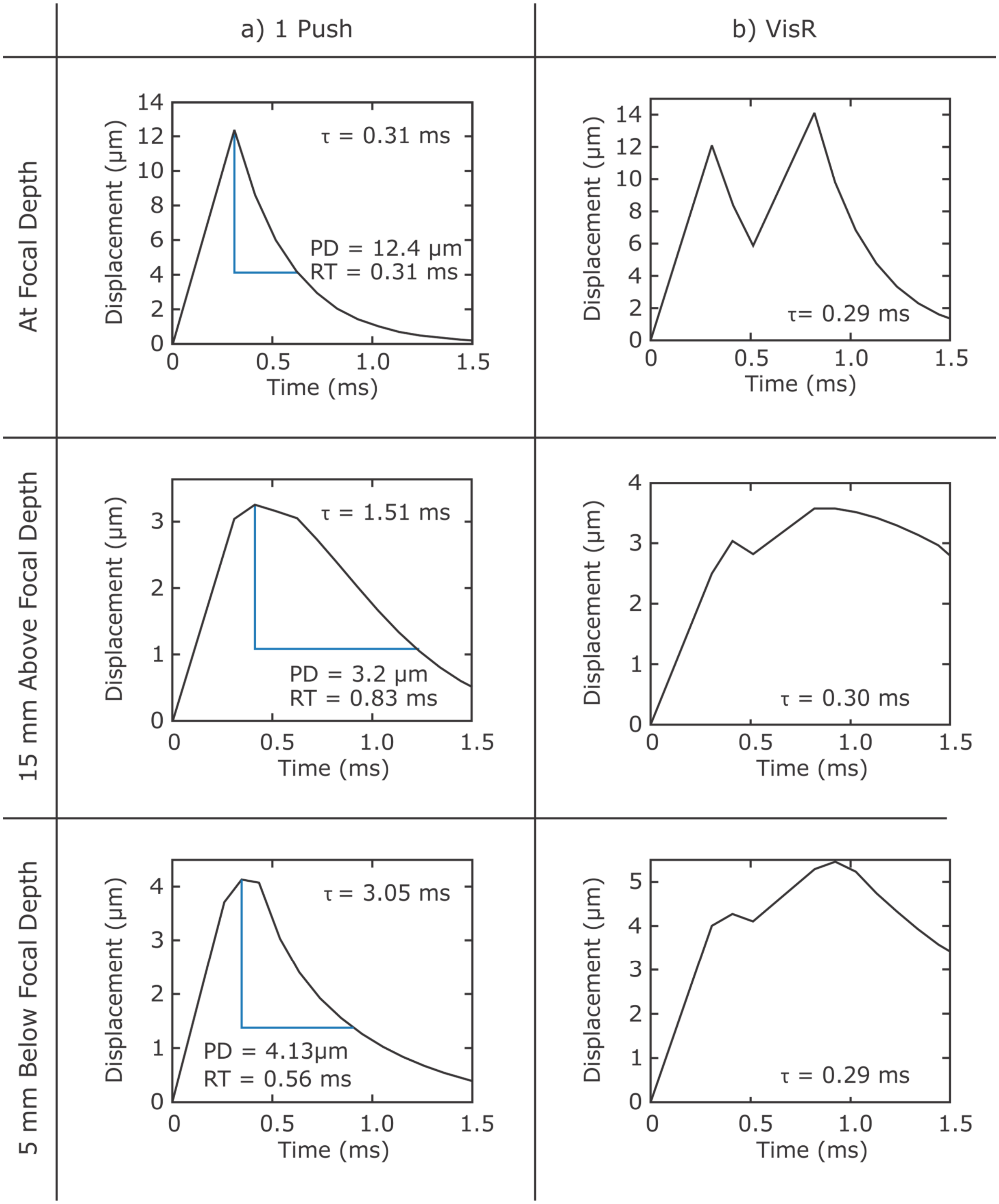

Figure 5.4: Representative (a) ARFI and single-push VisR and (b) double-push VisR one-dimensional axial displacement profiles measured in a homogeneous tissue mimicking phantom at the focal depth, 15 mm above and 5 mm below the focal depth. For each depth, ARFI peak displacement (PD) and recovery time (RT) measures (column a), single-push VisR τ values (column a), and double-push VisR τ values (column b) are shown. Although ARFI PD and RT and single-push VisR τ values vary with depth, double-push VisR τ values are more consistent.

data and predicted data, given by the R^2 statistic. R^2 values ranged from 0.955 to 0.999 for the double-push method and from 0.944 to 0.986 for the single push method.

VisR, ARFI, and B-mode imaging results in the structured phantom are shown in Figure 5.6. Recall that phantom background and spherical inclusion have comparable stiffness, but the background viscosity is lower than that of the inclusion (background is phantom formulation 1 and the inclusion is phantom formulation 6). For all three imaging methods, the focal depth was 34 mm. In the B-mode image [Figure 5.6(a)], the spherical inclusion is evident as the hyperechoic spherical structure spanning 24 to 39 mm axially and –10 to –1 mm laterally. The two boxes represent the positions of the ROIs within and outside the inclusion for CNR

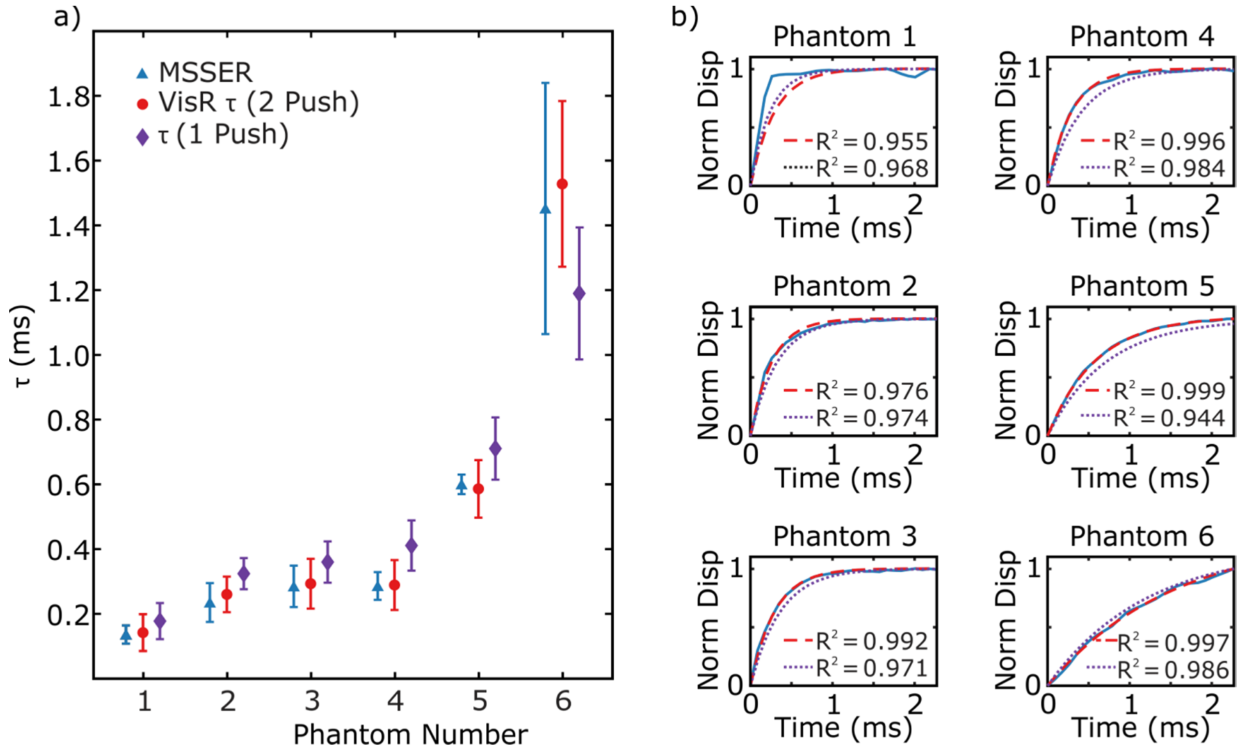

Figure 5.5: (a) Monitored steady-state excitation recovery (MSSER; triangles), double-push VisR (circles) τ values (mean ± standard deviation) estimated in the six examined homogeneous tissue phantoms at the focal depth are consistent ($p < 0.02$, paired t-test). Single-push VisR τ values (diamonds) are statistically different from those of MSSER in phantoms 2 and 4. (b) Double- (red, dashed) and single-push (purple, dotted) VisR τ values predict viscoelastic creep profiles by the Voigt model that follow the creep profile experimentally observed during MSSER imaging (blue, solid) in the six homogeneous phantoms. Similarity between creep profiles predicted by single- and double-push VisR and experimentally observed by MSSER is indicated by the R^2 value included in the corresponding panels.

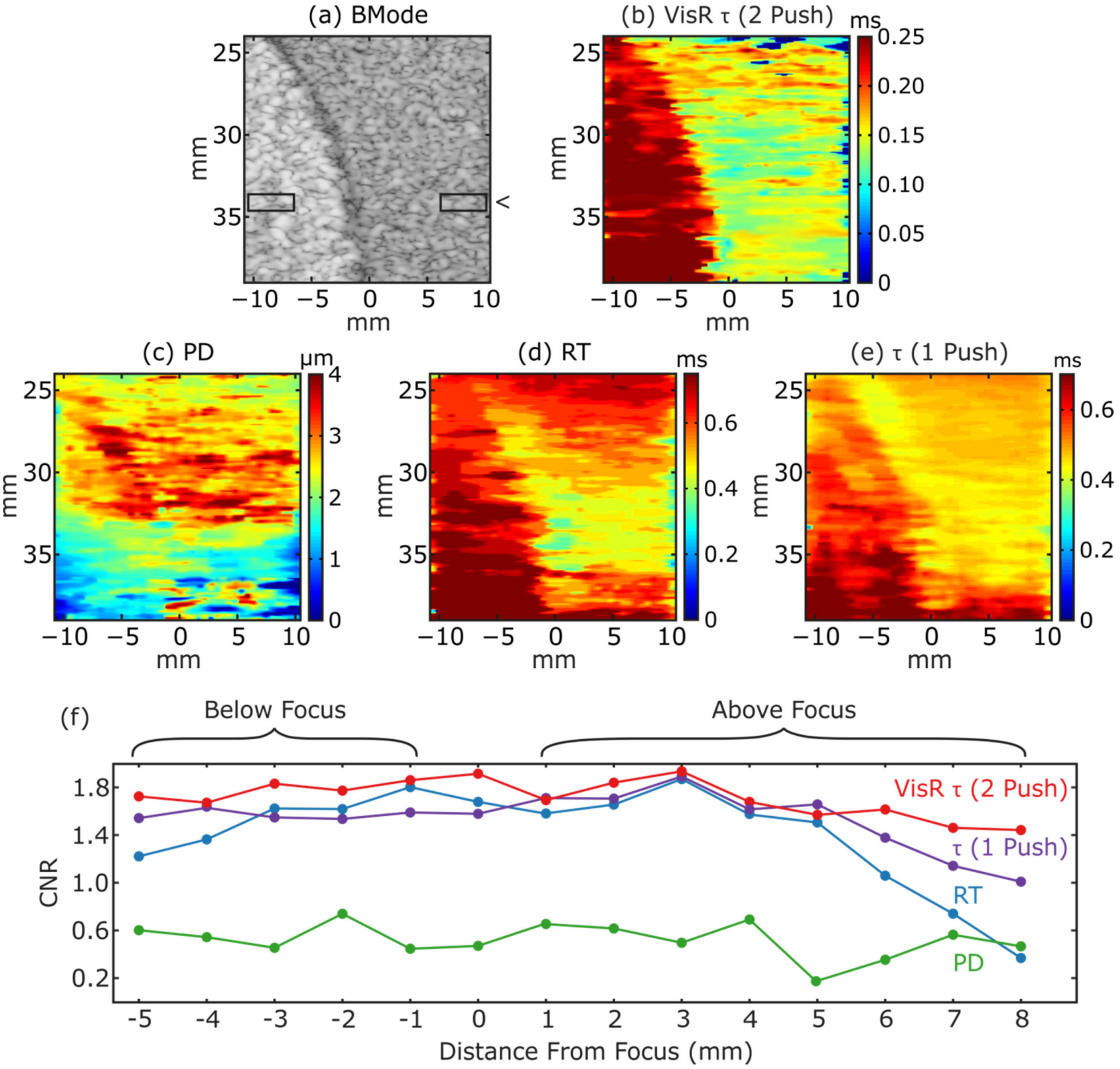

Figure 5.6: (a) B-mode, (b) double-push VisR τ, (c) ARFI peak displacement (PD), (d) ARFI recovery time (RT), and (e) single-push VisR τ images of a tissue-mimicking phantom with a spherical inclusion that is comparably stiff but more viscous than the background. The boxes in the B-mode image represent the 3 mm laterally by 1 mm axially ROIs used to calculate contrast-to-noise ratio (CNR). (f) CNR is plotted versus distance from the focus for the double-push VisR τ (red), ARFI PD (green), RT (blue) images, and single-push VisR τ (purple).

calculations. The boxes were moved axially in 1-mm steps to evaluate CNR as a function of distance from the imaging focus. In the double-push VisR τ image Figure 5.6(b), the lesion is clearly delineated across its 24 to 39 mm axial range; however, the lesion is not well distinguished from background in the parametric ARFI peak displacement (PD) image [Figure 5.6(c)]. The parametric ARFI recovery time (RT) image [Figure 5.6(d)] delineates the spherical inclusion better than the ARFI PD image, but CNR diminishes with distance from the focal depth, as is described by the graph of CNR versus distance from focus in Figure 5.6(f). Although ARFI RT yields comparable CNR to double-push VisR near the imaging focus, RT CNR drops 5 mm above the focus and 4 mm below the focus. This is not the case for double-push VisR, which maintains generally constant CNR across the 14 mm axial range of the inclusion. The single-push VisR image [Figure 5.6(e)] discriminates the inclusion with generally lower CNR than the double-push VisR method, but CNR is improved over that of RT alone from approximately 5 mm above the focus.

In vivo double-push VisR imaging in a canine semitendinosus (ST) muscle is shown with spatially-matched histochemistry in Figure 5.7. Figure 5.7 (a) shows the B-Mode image acquired during injection of the methylene blue dye to mark the imaging plane. The needle is evident in the upper right portion of the B-mode image (blue arrow). The corresponding gross muscle is shown in the top of Figure 7(b), with methylene blue dye macroscopically visible (blue arrow). Also observable are white anatomical features confirmed by Masson's trichrome stain [Figure 5.7(b) bottom] to be perimysial connective tissue outlining an area where three separate fascicles come into contact. This connective tissue is highly collagenated according to the Masson's stain and hyperechoic in the B-mode image [Figure 5.7(c)]. The connective tissue also yields low τ values in the spatially matched VisR image [Figure 5.7(d)]. The VisR image is superimposed with transparency on the B-mode image in Figure 5.7(e) to highlight the spatial alignment of low VisR τ estimates to the hyperechoic connective tissue in the B-mode image.

5.5 Discussion

VisR is a novel approach to elastographic imaging that estimates τ, the viscoelastic stress relaxation time constant in the Voigt biomechanical model, by delivering to the same region of

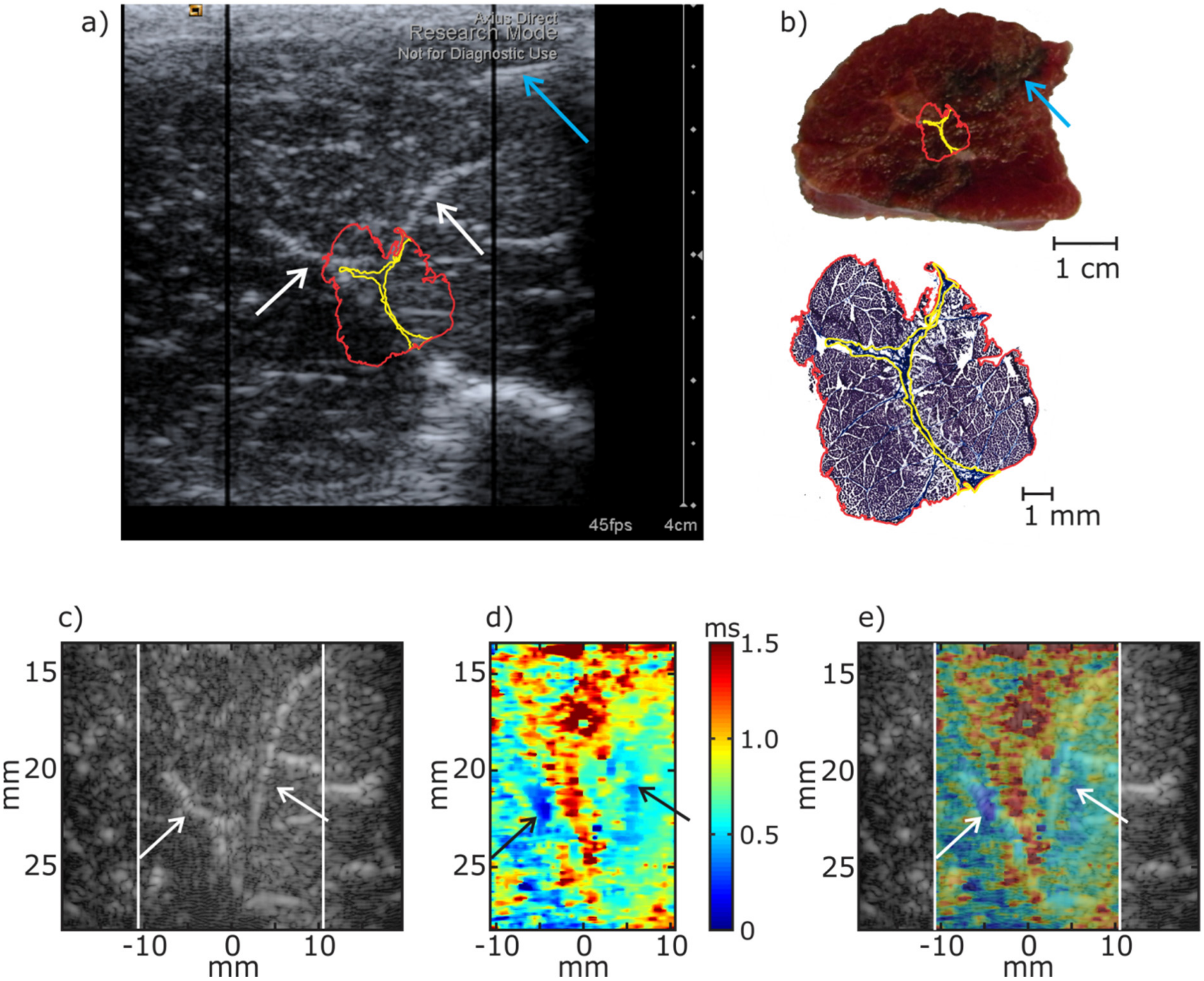

Figure 5.7: In vivo double-push VisR imaging in normal canine semitendinosis muscle: (a) The B-mode image captured from the system display shows the needle injecting methylene blue dye to mark the VisR imaging plane (blue arrow), and hyperechoic structures (white arrows). The hyperechoic structures and position of methylene blue injection are used to align the B-mode image to histology. The red polygon denotes the corresponding tissue in the histology section (panel 5.7b) with the hyperechoic structure contained within the histology section outlined in yellow. (b) In the gross image of the dissected muscle (top), the methylene blue mark is apparent (blue arrow). Also evident is white tissue spatially corresponding to the hyperechoic structures highlighted in the B-mode image, which are confirmed by Masson's trichrome stain to be highly collagenated connective tissue (bottom). The red polygon on the gross image denotes corresponding tissue in the Masson's stain, with the highly collagenated structure outlined in yellow. (c) The B-mode image rendered by envelope detection of the raw RF B-mode data acquired immediately before VisR imaging is shown with hyperechoic connective tissue structures again apparent (arrows). Note the injection needle was removed before VisR imaging to avoid disruption of ARF propagation beyond the needle. (d) The VisR τ image shows low τ spatially corresponding to the position of the connective tissue structures (arrows). (e) The spatial correspondence of low VisR τ estimates to the connective tissue structures is further demonstrated by overlaying the VisR transparency on the B-mode.

excitation one or two successive ARF excitations. Although the single-push VisR approach yields τ estimates that are similar to the double-push approach at the focal depth, the double-push approach supports a larger axial range over which τ estimates are valid. Figure 5.4 shows that in a homogeneous tissue-mimicking phantom, double-push τ values remained relatively constant from 5 mm below the focus (0.29 ms) to the focus (0.29 ms) to 15 mm above the focus (0.30 ms). On the contrary, the single-push VisR τ values varied from 3.05 ms below the focus to 0.31 ms at the focus to 1.51 ms 15 mm above the focus. This represents a 10-fold and 5-fold increase in single-push VisR τ values 5 mm below and 15 mm above the focus, respectively. The impact of single-push VisR's depth dependence on two-dimensional imaging is demonstrated in Figure 5.6, which shows that double-push VisR yields higher CNR over a larger axial range than single-push VisR, although in the axial range of 1 to 5 mm above the focal depth, single- and double-push VisR perform comparably in terms of CNR. These data demonstrate an important advantage to double-push VisR, which is the extended axial range over which its τ estimates are consistent. It could be possible to interrogate a 20 mm axial range using single-push VisR in the phantoms if an ARF excitation and tracking were performed every 4 mm axially. However, this would require a total of 6 ARF excitations, as opposed to 2 ARF excitations for the double-push VisR approach, to interrogate the same axial range.

Both single- and double-push VisR τ values estimated at the focal depth are compared with MSSER (which measures τ by pushing to steady-state displacement) in Figure 5.5. Figure 5.5(a) shows that single- and double-push VisR τ estimates are generally similar to each other and to MSSER-derived τ values in all phantoms. Double-push VisR τ estimates were not statistically different ($p < 0.02$) from MSSER τ values in any phantom. However, single-push VisR yielded τ estimates that were statistically different from MSSER τ estimates in phantoms 2 and 4. Moreover, single-push and double-push VisR τ estimates were statistically different from each other in phantom 6. Overall, the differences between τ estimated at the focal depth using single- or double-push VisR appear minor, which suggests that single-push VisR may be a useful tool if the desired axial range for imaging is limited to a few millimeters above the focal depth.

Although the methods of VisR support important ad vantages, including fast frame rates and independence from tissue inhomogeneity surrounding the ARF region of excitation, the VisR approach is associated with a critical limitation as it pertains to imaging tissue. Specifically, the Voigt model, upon which the VisR method is based, does not account for material mass, and therefore, no inertial terms are associated with the observed displacements. However, tissue is not massless, and neglecting contributions from inertia distorts VisR τ estimates. This is the topic of Chapter 7.

Another limitation to VisR is that it does not isolate the viscosity coefficient from the elastic modulus. Rather, VisR estimates τ, the ratio of viscosity coefficient to the elastic modulus. In this regard, VisR may be limited in scenarios in which discriminating changes in viscosity coefficient from changes in elastic modulus are diagnostically meaningful. For example, using VisR as described in this Chapter, it would not be possible to determine if a given tissue A has half the elastic modulus or twice the coefficient of viscosity of tissue B with a two-fold difference in τ.

The statistical sameness of double-push VisR and MSSER imaging methods in Figure 5.5 demonstrates that VisR, which exploits the Voigt biomechanical model in a manner similar to MSSER imaging but with far fewer ARF excitation and tracking pulses, achieves τ estimation much more efficiently than MSSER. Moreover, independence from pushing to a steady-state level of displacement and from observing undisturbed progression to steady-state in VisR makes its clinical implementation lower energy and more tractable than that of MSSER.

Another advantage of VisR is its independence from the applied ARF magnitude and from the impulsive nature of the ARF excitation. This is not the case for conventional ARFI imaging, in which induced peak displacement is proportional to the applied force magnitude that diminishes with distance from the ARF region of excitation. Further, ARFI recovery time measures are distorted away from the region of ARF excitation where the propagating excitation is no longer impulsive. This phenomena is illustrated in Figure 5.4. Figure 5.4(a) shows that with conventional ARFI, a point 15 mm above the focal depth exhibited a PD that was 74% smaller and an RT that was 167% longer than a point at the focus; similarly, PD was 67% smaller and RT was 81% longer in a point 5 mm below the focal depth compared with the point at the focus. In double-push VisR [shown in Figure 5.4(b)], despite decreases in achieved displacement, τ estimates at 15 mm above the focus and 5 mm below the focal depth were 3% smaller and equal to τ estimated at the focus, respectively.

It is important to consider that double-push VisR assumes that the two successively applied ARF excitation impulses are identical in a given region of excitation. Although this assumption is generally reasonable, variations in system output and/or shear wave reflections that are immediately coincident with (and inconsistently augment) one of the two successive excitation impulses may corrupt VisR τ estimates. In our preliminary experience to date, VisR τ estimates were not statistically significantly different ($p < 0.2$) over 10 repeated measures in the examined tissue-mimicking phantoms (data not shown), but a more thorough analysis of repeatability with specific attention given to the potential impact of system variation in force output on VisR τ estimates is warranted.

5.6 Conclusion

VisR, a new ARF-based elastographic imaging method that estimates the relaxation time for constant stress (τ) in viscoelastic materials, is presented with mathematical derivation based on the Voigt biomechanical model. Data acquired in tissue-mimicking phantoms highlight the key advantages to VisR. First, τ is estimated using displacement tracked in only the ARF region of excitation, so VisR is faster, lower energy, and less susceptible to corruption from tissue inhomogeneity than approaches that rely on measuring shear wave propagation over a millimeter-scale lateral distance from the ARF region of excitation. Second, double-push VisR is relatively independent from the magnitude of the ARF excitation, which results in a greater axial range than possible with conventional ARFI methods. Preliminary results in normal canine semitendinosus muscle suggest the clinical relevance of double-push VisR to muscle. VisR imaging in muscle is further explored in Chapter 6; specifically, VisR's sensitivity to muscle anisotropy is explored.

CHAPTER 6

VisR Ultrasound in Muscle: a Pilot Study

6.1 Introduction

In Duchenne muscular dystrophy (DMD) muscle tissue is progressively replaced by fibrous tissue and fat.[26] Therefore, serially evaluating muscle composition within a given individual is relevant to monitoring disease progression and to assessing the efficacy of treatment regimens. Similarly, comparing affected muscles across groups of individuals at various stages of disease progression or following different courses of therapy can offer insights to the natural history of the disease or differentiate treatment responses, respectively. Both serial and cross-sectional analyses require consistent tissue interrogation methods to ensure that measured changes are predominantly related to differences in the tissue itself rather than variations in the measurement technique.

As discussed in Section 2.1, skeletal muscle is composed of long muscle fibers which are aligned parallel to each other. Due to this geometric structure, the mechanical properties of the muscle are dependent on the orientation of the muscle fibers relative to the displacing force. Using an asymmetric indenter, Namani et al. demonstrated that fibered materials appeared stiffer when the long axis of the rectangular indenter was aligned perpendicular to the dominant fiber direction.[142,143] Therefore, if inconsistently aligned with respect to the asymmetric displacing force, muscle fiber orientation may confound both longitudinal and cross-sectional comparisons of muscle mechanical property. Controlling muscle fiber alignment relative to transcutaneous probing devices is nontrivial in an *in vivo* imaging environment in which muscles anatomically bend and twist. Rather than trying to control fiber orientation, its confounding effects may be obviated by utilizing a symmetric displacing force applied equally along fiber directions.

This chapter presents the results of a pilot study using VisR to image muscle tissue. VisR independence from muscle fiber direction is achieved by utilizing a symmetric focal configuration for the ARF excitation pulse.

6.2 Background

ARF Spatial Distribution

The spatial distribution of the applied ARF field is related to the focal configuration of the acoustic pulse, or F/# (see Section 4.1.1). When scaled by the center wavelength, the F/# approximates the full width at half max (FWHM) beam width in the lateral or elevational dimension.[144] For a standard 1-D linear array, lateral F/# (and lateral FWHM beam width) may be adjusted by electronically selecting the number of active elements; an F/1.5 lateral focal configuration is commonly used for the ARF excitation.[115,133,145–147] However, in the elevation dimension, F/# is static and set by the height of the transducer elements and the fixed-focus acoustic lens. For example, elements of the Siemens VF7–3 linear array transducer are 7.5 mm in height, and the elevation focus is fixed at 37.5 mm, giving the transducer an elevation focal configuration of F/5.[148] This elevation focus, paired with the F/1.5 lateral focal configuration typically used for the ARF excitation, results in an asymmetric pushing beam that is more tightly focused in the lateral dimension than in the elevation dimension.

With respect to using such an asymmetric ARF pushing beam for probing the mechanical properties of muscle, when the transducer face is oriented parallel to muscle fibers, as in Figure 6.1 (a), the long axis (elevation) of the ARF pushing beam will be perpendicular to the muscle fibers, and the interrogated tissue will be stiffer, resulting in a smaller VisR τ. Conversely, when the transducer is oriented perpendicular to muscle fibers, as in Figure 6.1 (b), the long axis (elevation) of the ARF pushing beam will be parallel to the muscle fibers, and the interrogated tissue will be less stiff, resulting in a larger VisR τ. On the contrary, a symmetrical ARF pushing beam, as in Figure 6.1 (c), will apply the ARF excitation equally along and across fibers, resulting in constant values of VisR τ regardless of transducer orientation. A symmetric ARF pushing beam is achieved in this work by using a standard 1-D linear array and adjusting the lateral focal configuration to match that of the fixed elevational focal configuration. VisR τ measures obtained for various muscle fiber orientations are compared across increasing ARF lateral focal configuration.

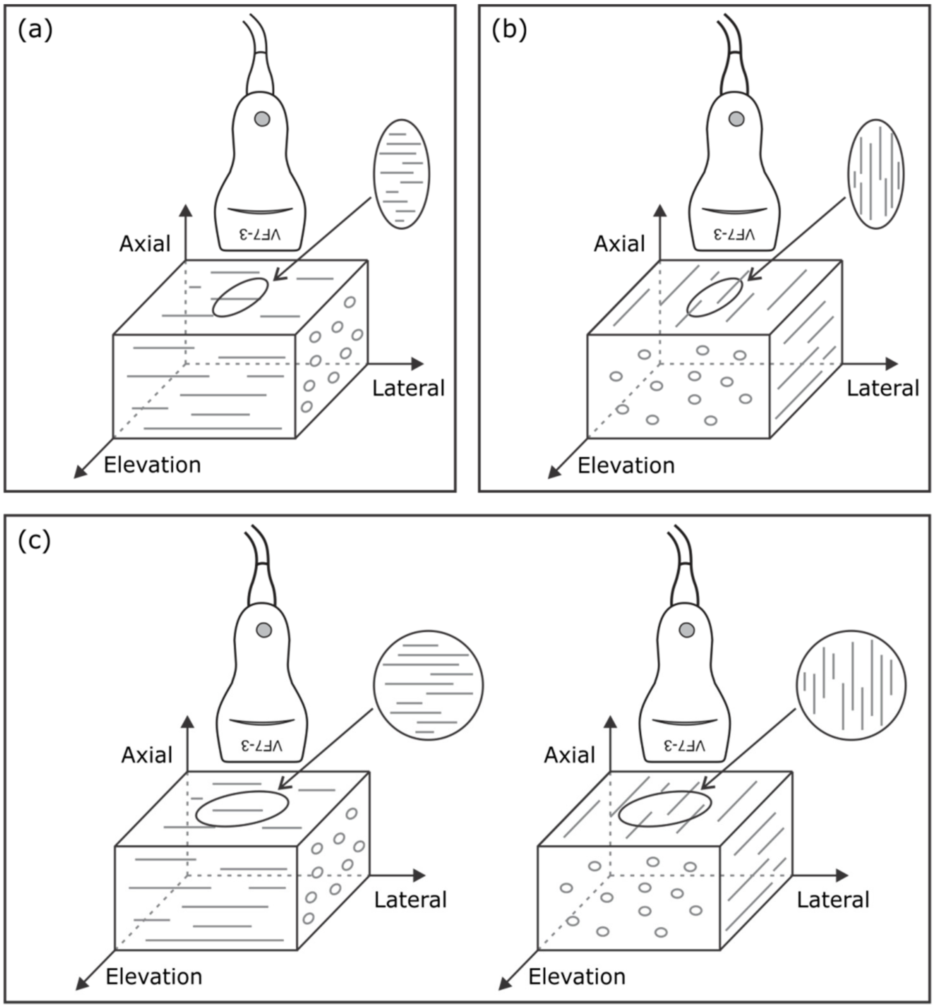

Figure 6.1: Simple model of muscle. (a) The long axis of the asymmetric focal region is oriented perpendicularly to muscle fibers. (b) The long axis of the asymmetric focal region is oriented parallel to muscle fibers. (c) The symmetric focal region interrogates the same tissue, regardless of the angle between the transducer and the muscle fibers.

6.3 Methods

A Siemens SONOLINE Antares ultrasound system equipped for research purposes (Siemens Medical Solutions USA, Inc., Ultrasound Division) and a VF7-3 linear array transducer were used for all experiments. Imaging was performed at an axial focal distance of 34 mm. ARF excitations were 300 cycles (70 µs) in duration and centered at 4.21 MHz with variable focal configuration (see below). Tracking pulses were centered at 6.15 MHz with an F/1.5 lateral focal configuration and an 11 kHz pulse repetition frequency. VisR beam sequences consisted of two reference tracking lines preceding a first ARF excitation, then 8 tracking lines followed by a second ARF excitation and two additional tracking lines for a total of 14 pulses. Four different ARF pushing beam focal configurations were used for VisR imaging during separate image acquisitions and included F/1.5, F/3, F/4, and F/5. ARF-induced displacement tracking in the region of excitation was performed using 1-D cross-correlation in the axial dimension between sequentially acquired tracking lines.[139] Each tracking line was up-sampled using cubic spline interpolation by a factor of 4 and divided into a series of 80 µm search regions; the location of the peak in the cross-correlation function between a 38 µm kernel in the first tracking line and a search region in the next tracking line was used to estimate axial tissue displacement in that region.

The effect of changing the lateral F/# on the FWHM of the ARF excitation was confirmed experimentally. The transducer was connected to a Newport ESP 300 programmable translation stage (Newport corp., Irvine, CA, USA), submerged in a water tank, and aligned with an Onda HGL-0200 hydrophone (Onda Corp., Sunnyvale, CA, USA). The hydrophone was connected to a Signatec PDA14A analog-to-digital (A/D) convertor (Signatec Inc., Newport Beach, CA, USA), and using a custom program developed in LabVIEW (National Instruments, Austin, TX, USA), the transducer was swept across the hydrophone in the lateral and elevation dimensions. In each position, a single 2-cycle A-line centered at 4.21 MHz and focused at 34 mm was transmitted to generate a 2D (lateral-elevational) map of the acoustic point spread function (PSF). The pressure values were averaged for 10 measurements, converted to decibels, and displayed as a contour map. The -6 dB level was selected as the FWHM dimensions of the PSF. This process was repeated for F/1.5, F/3, F/4, and F/5 lateral focal configurations.

To observe the impact of ARF focal configuration on VisR τ measures in isotropic material, VisR ultrasound was performed using all four ARF focal configurations in a homogeneous agar-gelatin, control phantom. The phantom was produced according to methods described by Hall et al. using 200 mL of deionized water, 36 g of gelatin (Type A, Acros Organics), 10 mL of N-propanol, and 2 grams of agar powder to induce scattering.[149] The phantom was placed on a turntable (shown in Figure 6.2) with the transducer fixed in place above it. Imaging then proceeded with F/1.5, F/3, F/4 and F/5 focal configurations for angles of rotation ranging from 0° to 90° with a 10° step.

In addition to the phantom studies, VisR imaging was performed *ex vivo* in anisotropic porcine muscle (psoas major). For muscle, the angles of rotation ranged from -10° to 110° in 10° steps, with an angle of 0° referring to when the transducer face was parallel to muscle

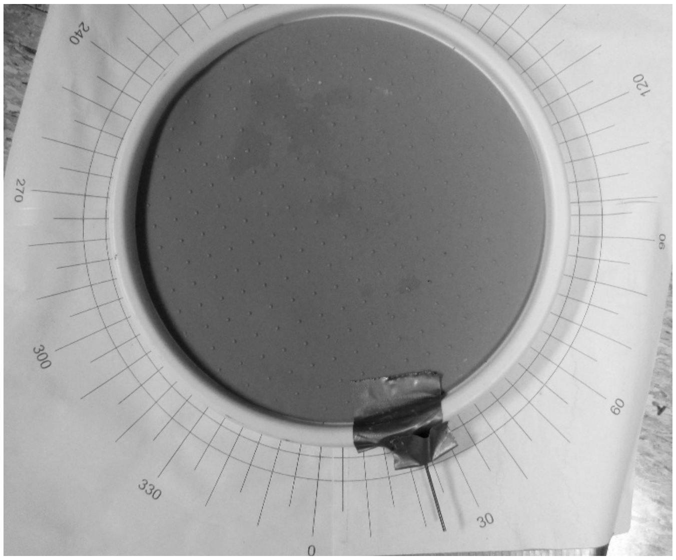

Figure 6.2: Picture of the turntable used in the experimental setup. Pork muscle was placed in center of turntable and transducer was mounted overhead.

fibers (determined by maximizing the length of hyperechoic lines in B-Mode imaging, Figure 6.7). Following the complete rotation, the turntable was returned to -10°, the transducer was manually lifted and then placed back down in approximately the same location, and imaging was repeated for the full range of angles. This was repeated for a total of three sets of acquisitions, with each set consisting of one VisR frame per angle.

For both phantom and muscle data, the mean and standard deviation (SD) of VisR τ in a 20 mm laterally by 2 mm axially region of interest (ROI) located just above the focal depth (34 mm) were calculated in each VisR frame. The variability of τ measurements within a single VisR frame was calculated as the coefficient of variation (CV), where CV = SD/mean. The mean, SD, and CV were then compared across all rotation angles in a single (the first for muscle) acquisition set. In addition, for each focal configuration and angle of rotation in the muscle, VisR τ values within the 20mm x 2mm ROI across the three repeated acquisitions were aggregated, and the aggregate mean, SD, and CV were calculated and compared across rotation angles.

Statistical Analysis

Descriptive statistics are expressed as mean ± SD. The paired t-test was used for comparisons between angles. A p value of < 0.05 was defined as significant.

6.4 Results

The measured PSFs for the F/1.5, F/3, F/4, and F/5 focal configurations are shown in Figure 6.3. The -6dB level is bold, and the associated ratios of the lateral beamwidth to the elevation beamwidth are listed. As expected, the lateral beamwidth is 73% smaller than the elevation beamwidth in the F/1.5 case, while the two are approximately equal in the F/5 case.

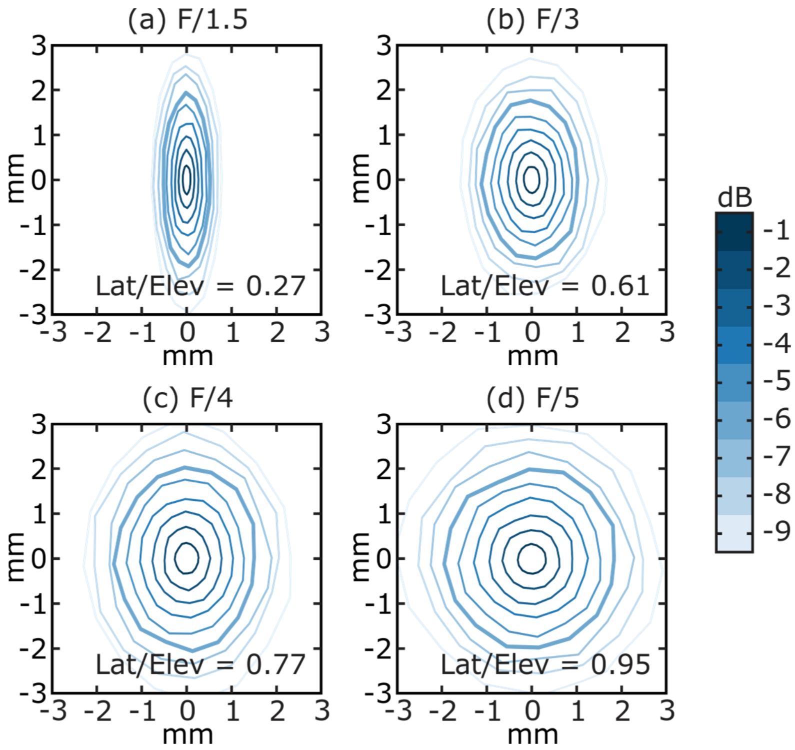

Figure 6.3: Point spread functions (PSF) measured experimentally, transmitting at 4.21MHz and using (a) F/1.5, (b) F/3, (c) F/4, and (d) F/5 focal configurations. Symmetry is indicated by the ratio of the lateral width to elevation height included in the corresponding panels.

Figure 6.4 panels (a) - (d) depict graphs of VisR τ value versus angle of rotation for the 4 ARF lateral focal configurations in the isotropic control phantom. Within any focal configuration, VisR τ measures are not statistically significantly different over the full range of rotation angles. Across focal configurations, the mean VisR τ value increases and the SD decreases with increasing F/#. Panel (e) illustrates the VisR τ CV versus rotation angle for the four ARF focal configurations. CV values are consistent across rotation angles for any single focal configuration but decrease with increasing F/#. Numerical VisR τ results in the isotropic control phantom are summarized in Table 6.1.

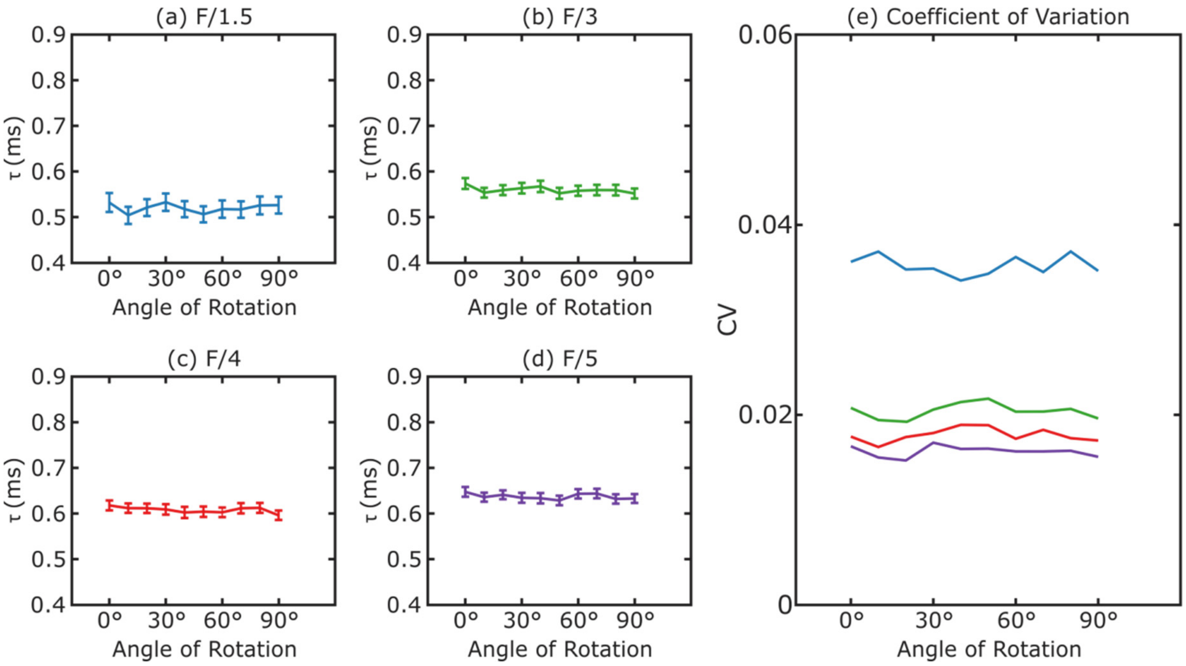

Figure 6.4: VisR τ (mean ± SD) measurements at angles of rotations from 0° to 90°, with 10° steps, in the homogenous, control phantom using (a) F/1.5, (b) F/3, (c) F/4, and (d) F/5 focal configurations. For all configurations, VisR measurements are consistent through all angles. (e) Coefficient of variation (CV) is highest in F/1.5 (blue), and decreases in F/3 (green), F/4 (red), F/5 (purple) focal configurations.

Figure 6.5 depicts VisR outcomes similarly to Figure 5 but for a single acquisition in excised pig muscle; numerical VisR τ results are given in Table 6.2. For the F/1.5 ARF focal configuration (panel a), VisR τ values increase with increasing angle of rotation from 0° to 90°, with VisR τ values measured at 30° and higher rotation angles statistically significantly different from that at 0°. A direct relationship between VisR τ values and rotation angle is also observed for the F/3 ARF focal configuration (panel b), although the difference between τ measured at 0° and 90° is smaller than in the case of the F/1.5 focal configuration. VisR τ measurements at rotation angles greater than 60° are statistically different from the 0° measurement. The difference in VisR τ values with rotation angle is further minimized for the F/4 focal configuration, with only measurements at 90° and 100° statistically different from the 0° measurement, and no statistically significant difference in VisR τ values with rotation angle is observed with the F/5 focal configuration. Comparing across focal configurations, trends toward increasing mean VisR τ values at 0°and decreasing SD with increasing F/# are observed,

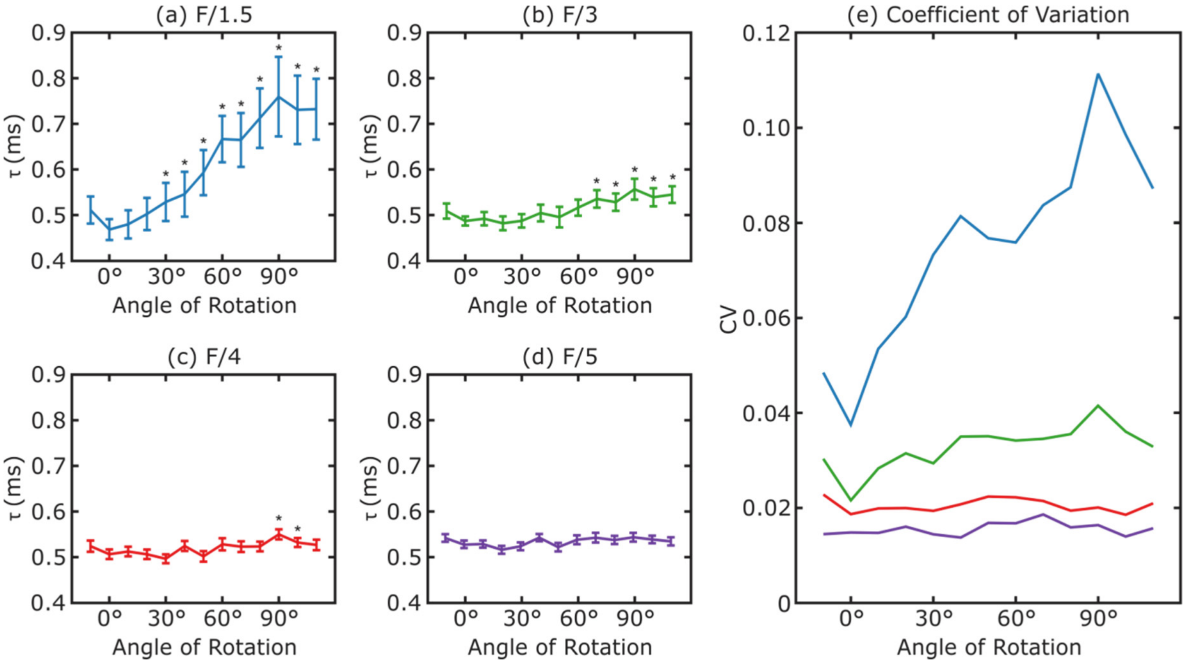

Figure 6.5: VisR τ measurements at angles of rotations from -10° to 110°, with 10° steps, in a single acquisition in the excised pig muscle. (a) For F/1.5, τ at 0° is significantly smaller than τ at angles > 20°. (b) For F/3, τ at 0° is significantly smaller than τ at angles > 60°. (c) For F/4, τ at 0° is significantly smaller than τ at 90° and 100°. (d) In F/5, τ at 0° is consistent through all angles. (e) Coefficient of variation (CV) is highest in F/1.5 (blue), and decreases in F/3 (green), F/4 (red), F/5 (purple) focal configurations.
*Signifies a statistically significant difference from 0° ($p<0.05$)

consistent with results in the isotropic phantom. CVs (panel e) increase with rotation angle between 0° and 90° for F/1.5 and F/3 focal configurations but remain relatively stable for the F/4 and F/5 focal configurations. Across focal configurations, CVs decrease with increasing F/#.

Aggregated results from the three repeated VisR acquisitions in the excised pig muscle are shown in Figure 6.6. Measurements of τ at 0° were significantly smaller than measurements at angles 50°-110° using F/1.5 (panel a), 80°-110° using F/3 (panel b), and 90° using F/4 (panel c). With the F/5 configuration (panel d), τ at 0° was not significantly different from τ at any other angle. Panel (e) shows the combined CVs for the three repeated acquisitions versus rotation angle using the four ARF focal configurations. The CVs of the F/1.5 (solid) and F/3 (dashed) configurations had local maxima at 0° and 90° and minimums at 50°. No significant trends

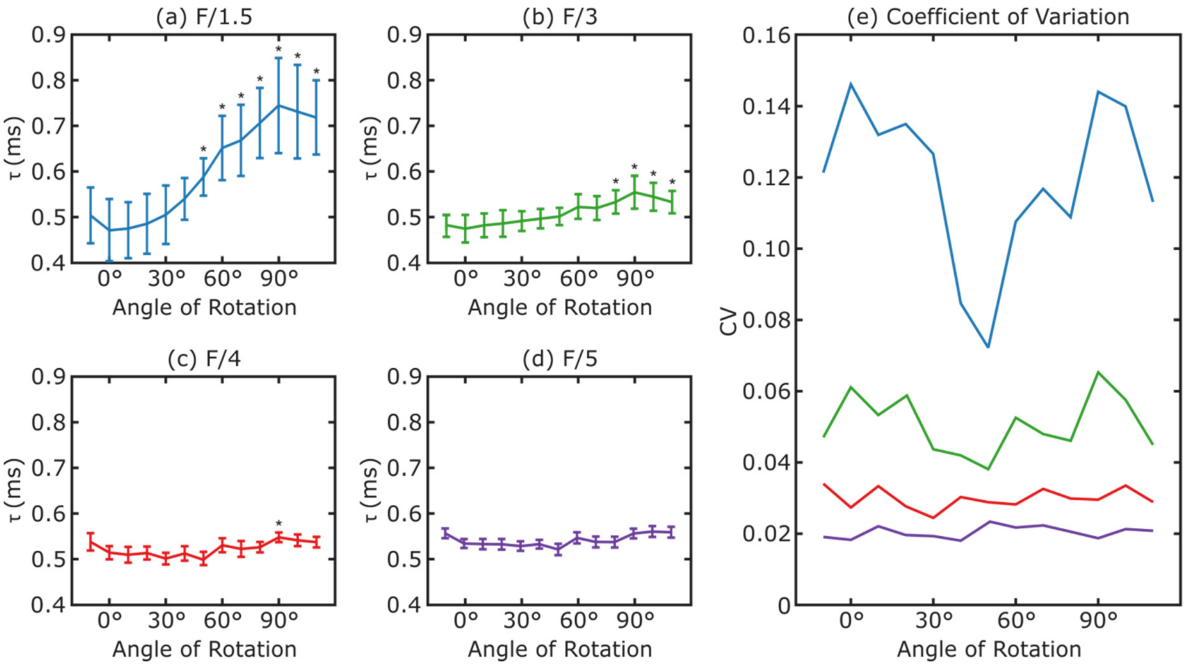

Figure 6.6: VisR τ measurements at angles of rotations from -10° to 110°, with 10° steps, in three repeated acquisitions in the excised pig muscle. (a) For F/1.5, τ at 0° is significantly smaller than τ at angles > 40°. (b) For F/3, τ at 0° is significantly smaller than τ at angles >70°. (c) For F/4, τ at 0° is significantly smaller than τ at 90°. (d) In F/5, τ at 0° is consistent through all angles. (e) Coefficient of variation (CV) is highest in F/1.5 (blue), and decreases in F/3 (green), F/4 (red), F/5 (purple) focal configurations. *Signifies a statistically significant difference from 0° ($p<0.05$)

were observed in the CVs of either the F/4 (dotted) or F/5 (dot-dash) focal configurations. Further, F/1.5 had the largest CV at every angle of rotation, followed by the F/3, F/4, and F/5, respectively. Numerical results of the repeated acquisitions in the muscle are summarized in Table 6.3.

Figure 6.7 shows B-Mode images (panel a) in the excised pig muscle with the transducer orientated at 0° and 90° relative to muscle fibers. The corresponding VisR τ images for the F/1.5 focal configurations are shown in panel (b), and depict VisR τ values which are appreciably larger at 90° versus 0°. Images generated with the F/5 focal configuration (panel c) show no significant differences in VisR τ values between the 0° and 90° transducer orientations.

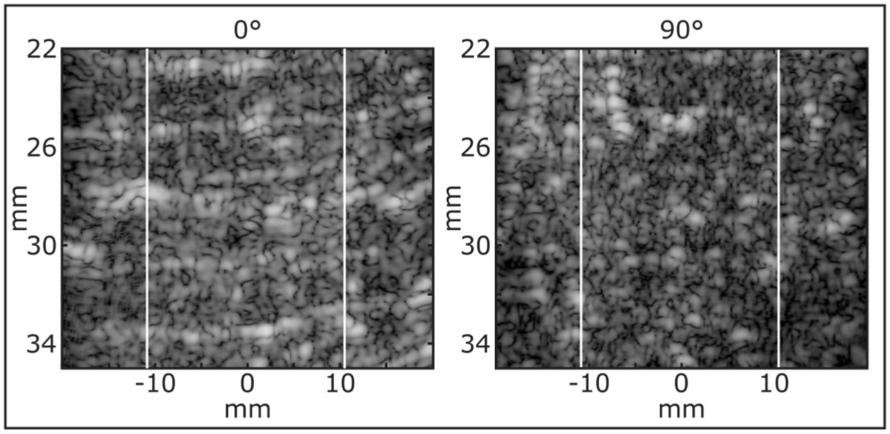
(a) B-Mode

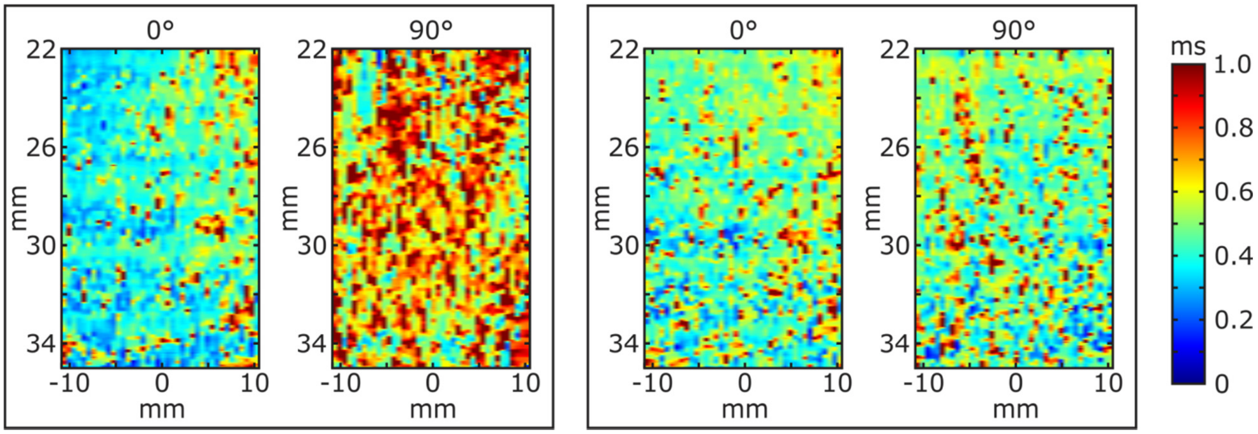
(b) F/1.5

(c) F/5

Figure 6.7: (a) B-Mode and VisR τ images in the excised pig muscle for (b) F/1.5 and (c) F/5 focal configurations with transducer oriented at 0° and 90° relative to muscle fibers.

6.5 Discussion

The expectation that muscle fiber orientation alters VisR τ measurements when using an asymmetric ARF excitation impulse was realized in these results. Figures 6.4 and 6.5 show that when using an F/1.5 lateral focal configuration for the ARF excitation, where the long axis (elevation) of the PSF is approximately 75% longer than the short axis (lateral), τ measurements at 0° were significantly different than 75% of the other examined rotation angles in the muscle, while no significant differences were measured in the control phantom; this suggests that VisR is sensitive to fiber orientation when using an ARF lateral focal configuration that is small relative to the elevational one. At 0° VisR τ was significantly different than 42%, 17%, and 0% of the other measurements when using F/3, F/4, and F/5, respectively, signifying consistency of τ values over a greater range of angles as ARF F/# increased and the ARF PSF became more symmetric.

Figures 6.4-6.6 show that the CVs of τ measurements were largest when using the F/1.5 ARF focal configuration and that CV decreased with larger F/#s. This is likely attributable to displacement estimation variance, or jitter. Walker et al. showed that jitter is increased with greater displacement magnitude.[150] Due to the tighter focusing and increase in the active aperture area (and thus transmit power) associated with the smaller focal configurations, larger displacements are induced by ARF excitations with lower F/#s; therefore, jitter in the displacement measurements are largest in the F/1.5 focal configuration and smallest in the F/5 focal configuration. The jitter in the displacement measurements will result in higher SD of τ measurements. Higher SD with smaller F/#s would account for the trend of CV decreasing with increasing F/#.

CV of VisR τ measurements in the muscle are depicted in Figures 6.5 (e) and 6.6 (e). In the single acquisition data set (Figure 6.6 (e)), the CVs of F/1.5 and F/3 were minimized at 0° where the muscle is stiffest and undergoes the smallest displacements with the lowest jitter. Conversely, the CVs of F/1.5 and F/3 were maximized at 90°, where the muscle is softest and undergoes the largest displacements and highest jitter. In the repeated acquisition data set (Figure 6.7 (e)), CVs of F/1.5 and F/3 were large at 0° and 90°. Since the muscle undergoes small displacements at 0°, this high variation in VisR τ measurements cannot be explained by jitter alone. Rather, we believe the higher variation at 0° and 90° in the repeated acquisition data is due to small changes in orientation of the muscles fibers after repositioning the transducer. With both the F/1.5 and F/3 configurations, the CV decreases as the angle approaches 45° where the muscle fibers are aligned approximately symmetrically within the asymmetric ARF PSF. Further, CVs become more consistent across angles as F/# increases in both the single and repeated acquisition data sets, suggesting that as the focal region becomes more symmetric, VisR measurements become more repeatable and less sensitive to variations in fiber orientations.

Taken together, these results suggest a critical finding in regard to interrogating anisotropic materials with ARF as in VisR ultrasound. For serial studies and for comparisons between individuals, symmetric focal configurations are needed to obviate the confounding effects of anisotropic feature alignment with respect to the ARF PSF shape. However, for studies aiming to exploit anisotropy, asymmetric focal configurations are needed to highlight different mechanical properties associated with different orientations. Therefore, focal configuration is an important consideration when evaluating muscle or other anisotropic tissues.

A limitation of the present work is that muscle fiber orientation in only the lateral-elevational 2-D plane was considered. This is a reasonable approach for the psoas major muscle, in which muscle fibers are primarily aligned parallel along a single axis. However, in many muscles and other anisotropic tissues, the orientation of anisotropic features in the axial dimension will also impact response to ARF excitation and influence VisR τ outcomes.

An important consideration is the apparent increase in VisR τ as the F/# increases. In the control phantom statistically significant differences in mean τ between focal configurations are measured at each angle (Figure 6.4 (a)-(d)). For instance, at 0° VisR τ is measured to be 0.53 ± 0.02 ms, 0.57 ± 0.01 ms, 0.62 ± 0.01 ms, 0.65 ± 0.01 ms using F/1.5, F/3, F/4, and F/5 configurations, respectively. As the F/# increases, the volume of the ARF focal region will increase. Palmeri et al. and Czernuszewicz et al. have both shown that recovery times are increased when using larger F/# focal configurations due to the increased time needed for a larger volume of tissue to stop moving.[112,151] This increase in the recovery time makes tissue appear more viscous, resulting in higher values of τ. Equation (5.4) is based on the Voigt model, which assumes a massless material; a model which incorporates a mass-term is needed to describe these inertial effects. This is the topic of Chapter 7.

6.6 Conclusion

This study demonstrated the dependence of VisR τ measurements on muscle fiber orientation as a function of ARF lateral-elevational PSF symmetry. Results showed that VisR τ values were dependent on fiber orientation with an asymmetric ARF focal configuration, but VisR τ measurements became increasingly less dependent on fiber orientation as the focal configuration was made more symmetric. This data also demonstrated a dependence of VisR τ estimates on the focal configuration in a homogeneous material, indicating the need for a mechanical model which accounts for inertia. In the next chapter the Voigt model, upon which VisR is based, is expanded to include a mass element.

Table 6.1: VisR in control phantom

F/#	τ at 0° (ms)	τ at 90° (ms)	p-value	Mean CV
1.5	0.532 ± 0.021	0.527 ± 0.018	0.385	0.036 ± 0.003
3.0	0.574 ± 0.012	0.552 ± 0.011	0.229	0.021 ± 0.002
4.0	0.618 ± 0.011	0.597 ± 0.010	0.291	0.017 ± 0.002
5.0	0.648 ± 0.011	0.633 ± 0.010	0.3219	0.013 ± 0.002

Table 6.2: Single acquisition of VisR in porcine muscle

F/#	τ at 0° (ms)	τ at 90° (ms)	p-value	Mean CV
1.5	0.469 ± 0.023	0.760 ± 0.087	0.006	0.074 ± 0.037
3.0	0.488 ± 0.010	0.557 ± 0.023	0.013	0.033 ± 0.020
4.0	0.507 ± 0.011	0.550 ± 0.011	0.034	0.021 ± 0.004
5.0	0.527 ± 0.008	0.544 ± 0.009	0.207	0.016 ± 0.005

Table 6.3: 3 Repeated acquisitions of VisR in pig muscle

F/#	τ at 0° (ms)	τ at 90° (ms)	p-value	Mean CV
1.5	0.472 ± 0.068	0.745 ± 0.104	0.004	0.119 ± 0.074
3.0	0.475 ± 0.030	0.555 ± 0.077	0.024	0.051 ± 0.027
4.0	0.515 ± 0.015	0.548 ± 0.011	0.033	0.029 ± 0.010
5.0	0.535 ± 0.010	0.556 ± 0.011	0.106	0.021 ± 0.005

CHAPTER 7

Accounting for Mass in VisR Ultrasound

7.1 Introduction

Viscoelastic Response (VisR) ultrasound is a method for quantitatively assessing the viscoelastic properties of tissue. Using two successive ARF impulses and monitoring induced displacements in the region of excitation, VisR fits displacements to a mechanical model to measure the relaxation time constant, τ, given by the ratio of viscosity to elasticity. In Chapter 6, VisR was demonstrated for characterizing the mechanical properties of gelatin phantoms and muscle by fitting displacements using the Voigt model; however the Voigt model assumes a massless material. In reality, all biological tissue has mass. The mass density of most soft tissues is slightly higher than that of water, typically lying in the range of 1.00-1.07 g/cm^3.[97]

Inertia is the tendency of a body to resist any change in its motion. In ARF applications, inertia will manifest as a delay in the time it takes for the material to reach its peak displacement and an increase in time needed to recover.[112] When inertial effects are ignored, these changes in the response of the material will be interpreted as an increase in the viscosity and/or a decrease in the stiffness of the material, both of which will result in an increase in τ.

This chapter extends VisR to account for inertial forces through the use of the mass-spring-damper (MSD) model. Using finite element method (FEM) modeling, the MSD and Voigt models are compared for their ability to describe the deformation induced by a focused, impulsive force and to discriminate τ in viscoelastic materials.

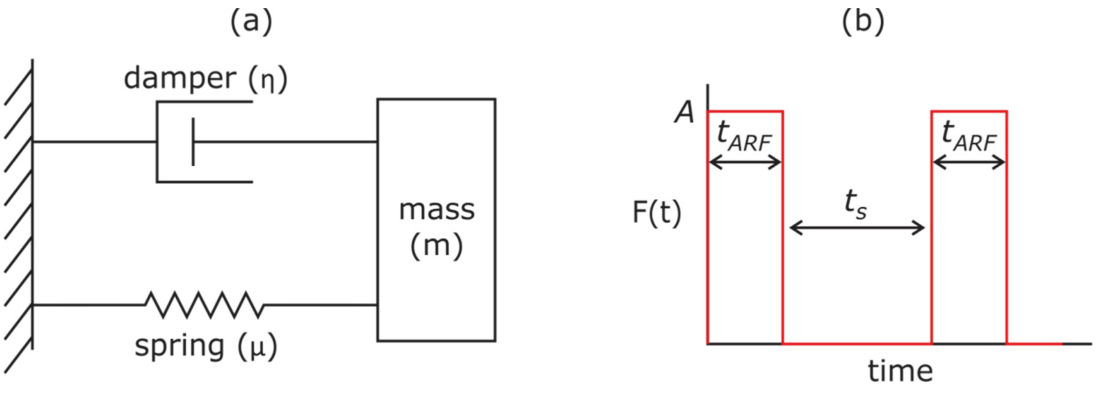

Figure 7.1: (a) A schematic of the mass-spring-damper (MSD) model and (b) a graphical illustration of the forcing function input

7.2 Background

The MSD is an alternative to the Voigt model, which places an inertial component in series with the Voigt model. A schematic for the MSD model is shown in Figure 7.1. The governing differential equation is given by:

$$m\frac{d^2}{dt^2}x(t) + \eta\frac{d}{dt}x(t) + \mu x(t) = F(t) \tag{7.1}$$

where F(t) is the applied force, x(t) is the induced displacement, μ is the elastic constant of the spring, η is the coefficient of viscosity of the damper, and m is the effective mass of the system. In standard form this becomes:

$$\frac{d^2}{dt^2}x(t) + \omega^2\tau\frac{d}{dt}x(t) + \omega^2 x(t) = \frac{F(t)}{m} \tag{7.2}$$

where ω is the natural frequency (in radians/ms), and τ is the relaxation time constant (in ms). These material parameters are defined as:

$$\omega = \sqrt{\frac{\mu}{m}} \quad , \quad \tau = \frac{\eta}{\mu}. \tag{7.3}$$

As in Section 5.2, the two ARF excitations, depicted in Figure 7.2, can be described as two rectangular pulses of duration t_{ARF} and amplitude A, and separated by t_s in time, and are defined as below:

$$F(t) = A\big(H(t) - H(t - t_{ARF})\big) + A(H(t - t_{ARF} - t_s) - H(t - 2t_{ARF} - t_s)) \tag{7.4}$$

where $H(t)$ is the Heaviside unit function and is given by:

$$H(t) = \begin{cases} 0, & t < 0 \\ 1, & t \geq 0\,. \end{cases} \tag{7.5}$$

Substituting (7.4) into (7.2) yields:

$$\begin{aligned} &\frac{d^2}{dt^2}x(t) + \omega^2\tau\frac{d}{dt}x(t) + \omega^2 x(t) \\ &\qquad = s\omega^2\big(H(t) - H(t - t_{ARF}) - H(t - t_{ARF} - t_s) + H(t - 2t_{ARF} - t_s)\big) \end{aligned} \tag{7.6}$$

$$s = \frac{A}{\mu}\,. \tag{7.7}$$

Equation (7.6) can be solved for displacement as a function of ω, τ, and s. Displacement versus time profiles can be fit to this equation in order to generate estimates of these three parameters.

7.3 Methods

The FEM models used have been adapted from models previously developed by Palmeri at al. for investigating the response of an elastic material to an ARF excitation.[111] In Chapter 8, Palmeri et al.'s methods for simulating the focal geometry of an ARF excitation pulse are implemented; however, for clarity, the excitation is approximated as a concentrated force on a single node at a given focal depth in this chapter.

FEM Mesh Generation

A three-dimensional, rectangular, solid mesh was assembled from 0.5 mm, cubic elements using LS-PREPOST (Livermore Software Technology Corp., Livermore, CA). The mesh extended 5 mm in elevation, 7.5 mm laterally, and 40 mm axially. A 5 elements thick, perfectly matched layer (PML) was added to the exterior boundaries of the mesh to absorb any waves generated during the simulation and ensure that they were not reflected back into the region of interest (ROI).[152] As a requirement of the PML, all nodes on outer faces were fully constrained. Quarter-symmetry was assumed in both the lateral and elevation dimensions, requiring only a quarter of the field to be modeled, and thus reducing the computational requirements of the simulation.

Material Properties

Tissue was modeled as a Voigt, viscoelastic material using the MAT_KELVIN-MAXWELL_VISCOELASTIC material model (See Appendix A). Young's modulus of the material was varied from 10 to 50 kPa, by steps of 10 kPa, and the viscoelastic coefficient was varied from 3 to 7 Pa·s, by steps of 2 Pa·s. The MAT_PML_ELASTIC material model was employed for the PML, with the elasticity set to match that of Voigt material. The density of the material was varied from nearly massless at 0.05 g/cm^3 to a physiologically relevant value of 1.0 g/cm^3. A Poisson's ratio of 0.499 was used for all simulations.

Forcing Function

Displacement was induced using a concentrated force on the single node centered laterally and elevationally and at an axial depth of 25 mm. Field II[153] was used to simulate the pressure field of a linear array transducer transmitting at 4.21 MHz, with an F/1.5 focal configuration, and focused at 25 mm, in order to determine the magnitude of the force. In time, the force was described according to Equation (7.4), with t_{ARF} equal to 70 µs and t_s equal to 0.4 ms.

FEM Implementation and Data Analysis

The FEM simulations were performed using the commercially available FEM package, LS-DYNA, using an explicit, time-domain, integration method. For each simulation, a dataset describing the axial displacements at the focal node was obtained. Axial displacement versus time profiles were fit to the Voigt and MSD models using nonlinear regression (fminsearch in Matlab, The MathWorks Inc., Natick, MA) to solve inversely for τ.

Statistical Analysis

VisR τ estimates from Voigt and MSD models were statistically compared with the ratios of viscosity to elastic modulus of the materials using the Wilcoxon two-sample test. A p value of < 0.05 was defined as significant.

7.4 Results

Representative displacement profiles from VisR simulations in the 20 kPa, 5 Pa·s viscoelastic material are shown in Figure 7.2 for densities of (panel a) 0.05 g/cm^3 and (panel b) 1.0 g/cm^3. The fitted Voigt and MSD models are shown as blue and green dashed lines respectively, while the FEM displacement is displayed in red. The accuracy of the model in describing the dynamics of the deformation was determined by the closeness of fit between the FEM simulated displacement and the model predicted displacement, given by the mean squared error (MSE) statistic. For the 0.05 g/cm^3 density material, the MSE of the Voigt fit was 0.0029

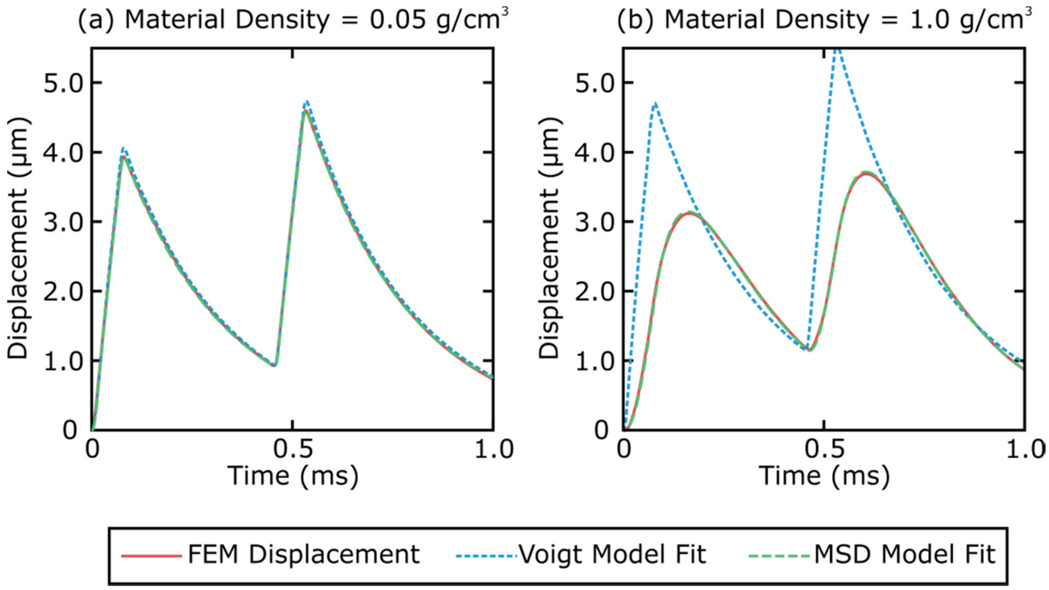

Figure 7.2: Simulated displacement profiles (blue, solid) in a 20 kPa, 5 Pa·s material with a mass density of (a) 0.05 g/cm^3 and (b) 1.0 g/cm^3 and the predicted displacement using the Voigt (green, dashed) and MSD (red, dashed) models.

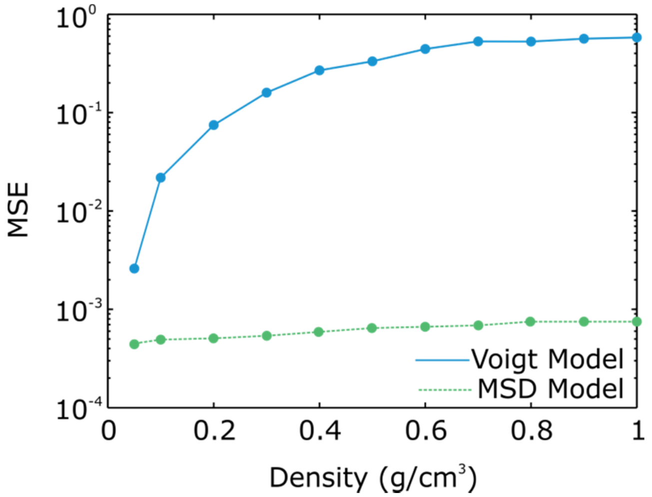

Figure 7.3: Mean squared error (MSE) metric describing the similarity between the FEM displacement profile and the displacement profile predicted by the Voigt (blue) and MSD (green) models in the 20 kPa, 5 Pa·s material at densities ranging from 0.05 g/cm^3 – 1.0 g/cm^3. Note the log scale on the y-axis. MSEs ranged from ranged from 0.0029 to 0.5794 μm^2 using the Voigt model and from 0.00044 to 0.00075 using the MSD μm^2 model.

μm^2 and the MSE of the MSD model fit was 0.00044 μm^2. The MSE values in the 1.0 g/cm^3 density material, increased to 0.5794 μm^2 using the Voigt model and 0.00075 μm^2 with the MSD model. The MSE values using the two models in the 20 kPa, 5 Pa·s material are plotted against mass density in Figure 7.3.

Figure 7.4 (a-b) shows the VisR τ measurements in all 15 viscoelastic materials plotted against the simulated material τ when the density of the materials was (a-b) 0.05 g/cm^3 and (c-d) 1.0 g/cm^3. The elasticity of the material is indicated by color, while the viscosity of the material is indicated by symbol. Using the Voigt model, τ estimates were not statistically significantly ($p>0.05$) different from the programmed material τ values when the density was 0.05 g/cm^3 (panel a), however when density was increased to 1.0 g/cm^3 the Voigt model produced τ estimates that were significantly larger ($p<0.05$) than the true τ of the material (panel c). For both densities, the MSD model generated τ values that were consistent with the material τ values (panels b & d).

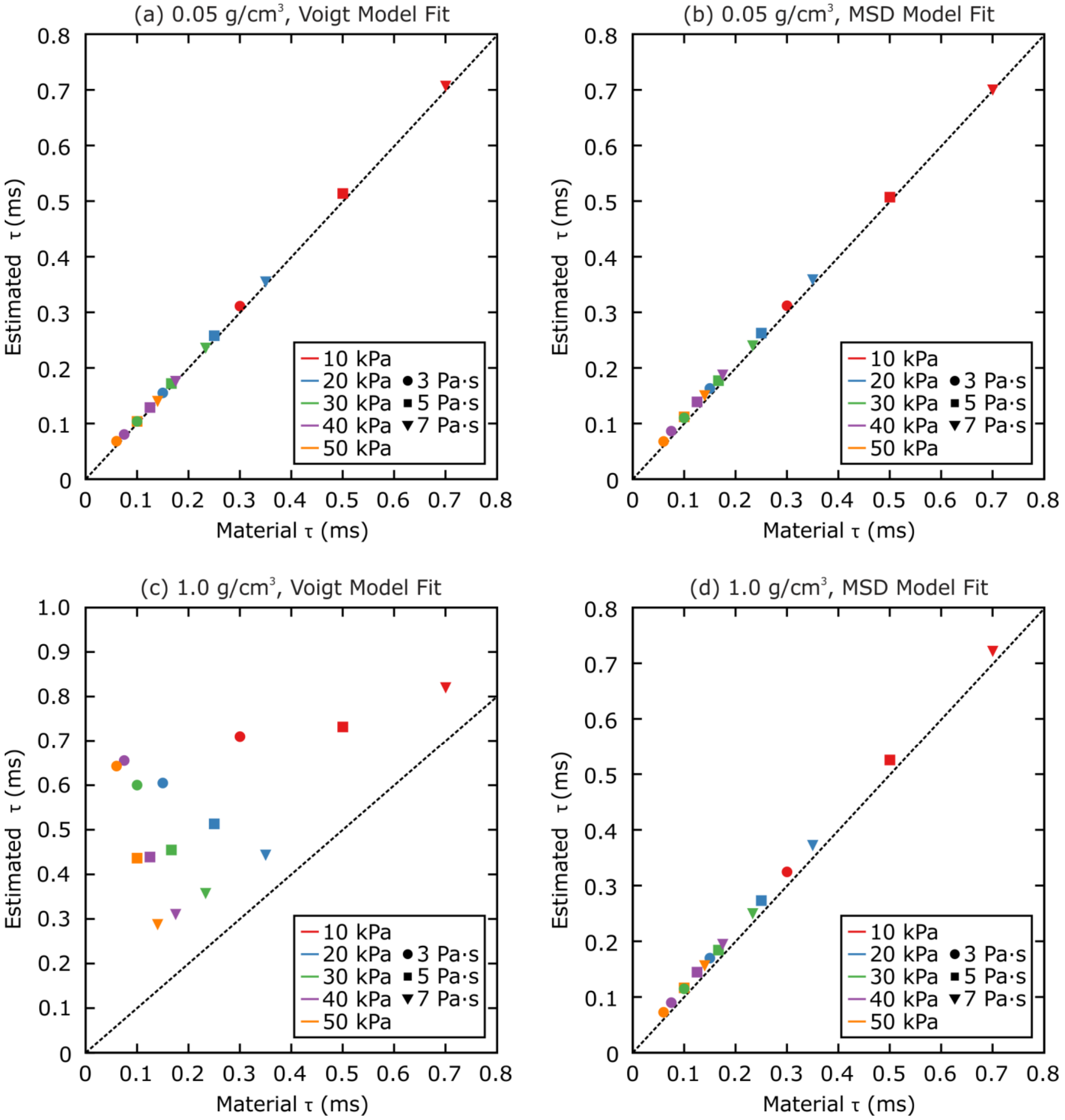

Figure 7.4: Scatter plots of VisR τ estimates versus the simulated material τ for the 15 viscoelastic materials with a density of (top row) 0.05 g/cm^3 or (bottom row) 1.0 g/cm^3. The elasticity of the material is indicated by color and viscosity is indicated by symbol. The dashed black line indicates the line of equality. Estimates of τ in the 0.05 g/cm^3 dense materials were consistent with the material τ ($p > 0.05$, Wilcoxon two-sample test) using both the Voigt (a) and MSD (b) models. In the 1.0 g/cm^3 dense materials, τ estimations were statistically different from the material τ when made using the Voigt (c) model but consistent with the material τ when using the MSD model (d).

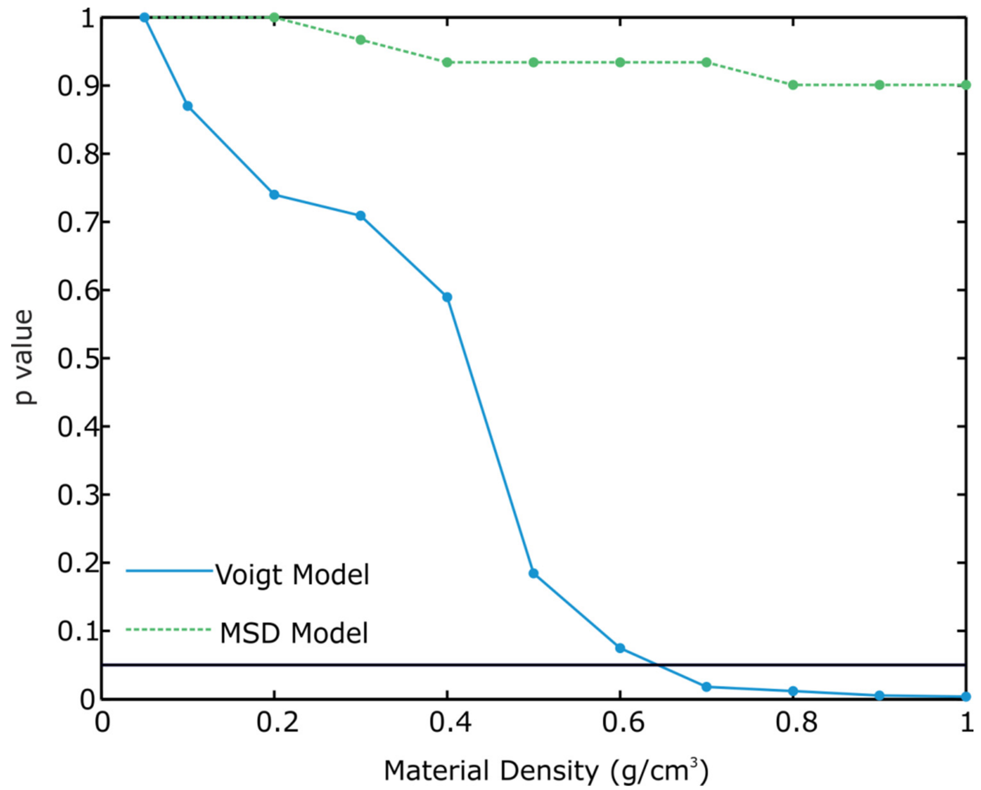

Figure 7.5: Wilcoxon two-sample test p values of the τ estimates generated by the Voigt (blue) and MSD (green) model at each of the density values. The black line represents statistical significance at the 0.05 level. Voigt model derived τ estimates were statistically significantly different from the real τ of the materials for density > 0.6 g/cm^3. Estimates of τ generated using the MSD model were consistent with the material τ values at all densities.

Statistical significance of the τ estimates generated with the two models relative to the density of the medium is illustrated in Figure 7.5. Values below the black horizontal line indicate τ values that are statistically significantly different from the true τ values at the 0.05 level. When material densities were 0.7 g/cm^3 and greater, τ estimates from the Voigt model (blue) were significantly different from the material τ values. Meanwhile, MSD model (green) derived τ estimates were not statistically significantly different from the material τ value at any density between 0.05 – 1.0 g/cm^3.

The error in τ measurements when density was 1.0 g/cm^3 is shown in Figure 7.6. Using the Voigt model τ was overestimated from the true value by 126.804 ± 155.846% on average (panel a). The average error in τ estimated using the MSD model was 15.344 ± 3.693% (panel b).

7.5 Discussion

VisR is a novel approach to elastographic imaging that approximates a creep test using only two successive excitations. The accuracy of VisR at estimating τ, the ratio of viscosity to elasticity is, however, dependent on the viscoelastic model chosen to describe the response of the material.

The Voigt model assumes a massless material. This assumption was valid when a density of 0.05 g/cm^3 was used. In Figure 7.2 (a) there is very little observable difference between the FEM displacement and the Voigt predicted displacement, and as shown in Figure 7.4 (a), the Voigt model accurately estimated τ values in all 15 viscoelastic materials. This was not the case when density was increased to 1.0 g/cm^3. The effects of inertia on the dynamic response of the

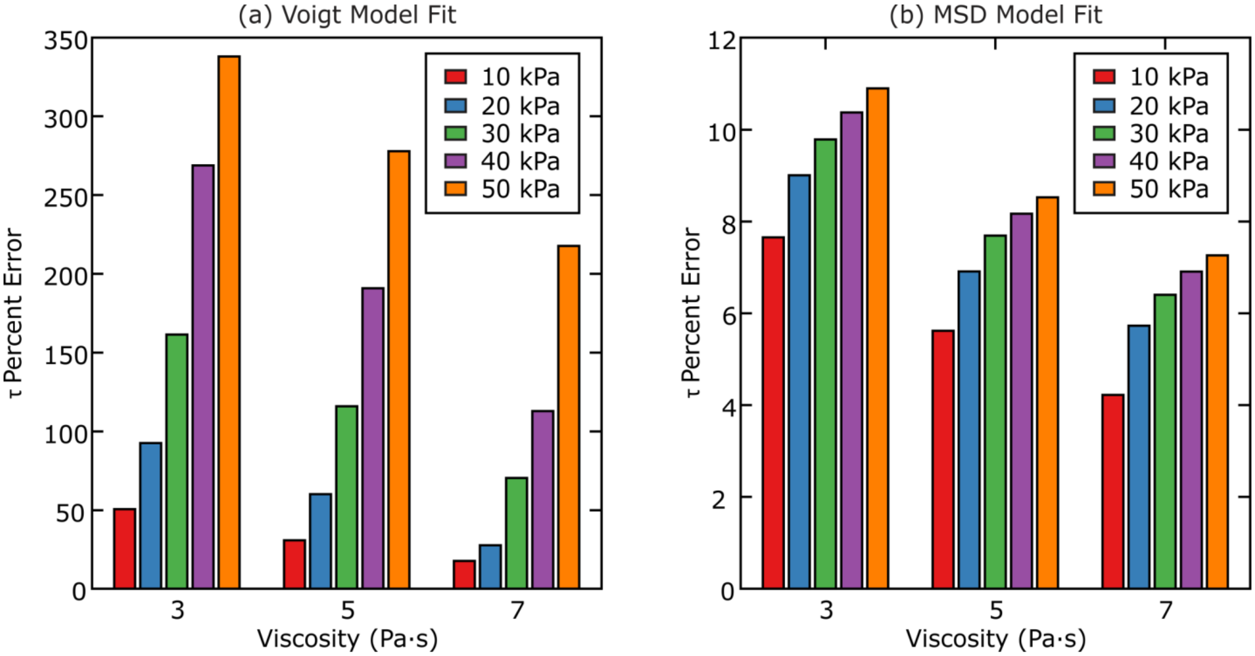

Figure 7.6: Percent error in estimated τ values using the (a) Voigt and (b) MSD model to generate τ when material density was 1.0 g/cm^3. Error in τ values from Voigt model ranged from 17.7%-339.4% with a mean 126.8%. Using the MSD model, error ranged from 4.2%-10.9% with an average of 15.3%. Note the different vertical axes in panels (a) and (b).

material can be seen in Figure 7.2 (b) and are manifested as a delay in response to the initiation and cessation of force. The Voigt model is unable to account for the change in the displacement profile due to inertia; the delay in the time for the material to reach its peak and to recover is attributed to increase in material viscosity and/or a decrease in the stiffness of the material. This is reflected in an increase in estimated τ relative to the true value (Figure 7.4 (c)). This supports the results in Chapter 6, which showed that increasing the F/# of the ARF excitation (resulting in an increased mass of tissue being displaced) in a homogeneous phantom will result in an increase in estimated τ using the Voigt model. The fact that the Voigt model could only generate τ values that were not significantly different from the real values when mass density was below 0.7 g/cm^3 (Figure 7.5) limits its use for imaging soft tissue, as the density of these tissues is between 0.9-1.1 g/cm^3.

Because the MSD model involves an inertial component it is able to compensate for changes in the density the medium. As illustrated in Figure 7.3, there is little difference in the model's ability to describe the dynamics of a material regardless of whether the material has a mass density of 0.05 g/cm^3 or 1.0 g/cm^3. The MSD model was able to accurately estimate the τ values of all 15 viscoelastic materials at all investigated densities. When the density of the materials was 1.0 g/cm^3, τ was estimated to within 11% of the true τ values. The highest error in estimated τ was in the 50 kPa, 3 Pa·s material in which τ was estimated to be 0.0066 ms higher than the true value 0.060 ms.

Unlike MSSER, which displaces material to a steady-state level and uses the full creep and recovery profile to fit to the mechanical model, VisR only observes displacements prior to steady-state displacement where inertia is relevant. Thus, the Voigt model, which was used successfully in MSSER, is no longer appropriate. Rather, the MSD model, which accounts for material mass, should be used for VisR ultrasound. These data show that when used in concert with two successive impulses, the MSD model can quantitatively describe τ, the relaxation time constant of a viscoelastic material. It is important to note, however, that these simulations were performed by applying force to a single node; whether VisR can remain quantitative when using a volumetric ARF body force excitation is the topic of Chapter 8.

7.6 Conclusion

VisR, a new ARF-based elastographic imaging method that estimates the relaxation time for constant stress (τ) in viscoelastic materials, is presented with mathematical derivation based on the MSD mechanical model. The MSD model outperformed the Voigt model in terms of fitting displacement profiles and accurately describing τ in FEM simulated viscoelastic materials when materials had a density comparable to human soft tissue, signifying the need to account for mass in VisR. These data show that the relevance of the VisR imaging technique is critically dependent on the choice of mechanical model; moving forward, VisR ultrasound will utilize the MSD model to describe soft tissue.

CHAPTER 8

Quantitative VisR Ultrasound

8.1 Introduction

As previously discussed, Viscoelastic Response (VisR) ultrasound is a method for quantitatively assessing the viscoelastic properties of tissue. It was demonstrated in Chapter 7 that using two successive force impulses and monitoring induced displacements in the region of excitation, displacements could be fit to the mass-spring-damper model to accurately measure the relaxation time constant, τ, given by the ratio of viscosity to elasticity. However, the force impulses used in Chapter 7 represented highly idealized point forces with no lateral, elevational, or axial extent. Such highly focused force impulses cannot be generated physically using conventional ultrasound linear array transducers. Rather, the ARF impulses generated using conventional linear arrays are volumetric and span millimeters in axial, lateral and elevation dimensions, as depicted in Figure 8.1 (a).

The volumetric nature of the ARF impulses results in force application outside the tracking focal position, which, we hypothesize, generates shear and longitudinal waves that propagate through the medium and interact with the displacing material at the focus. This interaction extends the duration of the force experienced at the focus beyond that of the applied ARF excitation. An excitation force that persists longer than modeled prolongs the displacement and recovery behavior of the material, as depicted in Figure 8.1 (b), and, thus, falsely indicates lower elasticity and/or higher viscosity, causing VisR to overestimate τ.

Correcting VisR's τ overestimation would ideally be achieved by appropriately modifying the modeled forcing function (Equation 7.2), but this would require *a priori* knowledge of the duration and amplitude of the shear and longitudinal wave interactions at the focus - parameters that are materially and geometrically dependent and generally unknown. Instead of relying on *a priori* material property estimates, this chapter aims to correct VisR τ overestimation by using an empirically determined correction factor generated from FEM models in representative viscoelastic materials. This method of error correction is then demonstrated experimentally in a gelatin phantom using a high-speed camera to optically track the ARF-induced displacements. Optical tracking is used in this proof of feasibility study because acoustically tracked ARF displacements are susceptible to underestimation, which is topic of Chapter 9.

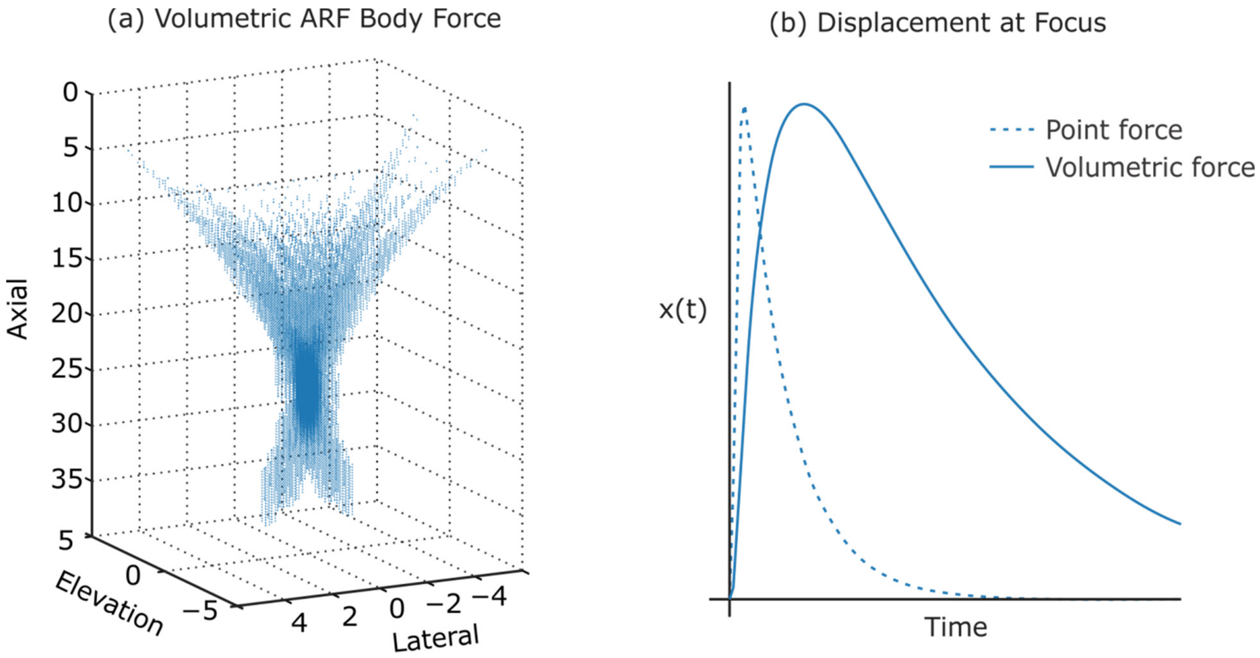

Figure 8.1: (a) Spatial distribution of force using a volumetric ARF body force. (b) Axial displacement at focus induced by a single point force (dashed) and induced by a volumetric ARF body force (solid).

8.2 Methods

8.2.1 FEM Simulations

Mesh Generation

LS-PREPOST (Livermore Software Technology Corp., Livermore, CA) was used to generate a three-dimensional, rectangular, solid mesh consisting of 0.25mm, cubic elements. The spatial extent of the mesh was 4 mm (elevation), by 10 mm (lateral), by 45 mm (axial). As in Chapter 7, a 5 element thick PML was added to the exterior to prevent wave reflections from boundaries, and quarter-symmetry was assumed.

Material Properties

Tissue was modeled as a Voigt, viscoelastic material using the MAT_KELVIN-MAXWELL_VISCOELASTIC material model. Young’s modulus of the material was varied from 5 to 100 kPa, by steps of 5 kPa, and the viscoelastic coefficient was varied from .5 to 9.5 Pa·s, by steps of 1 Pa·s. A density of 1.0 g/cm^3 and a Poisson's ratio of 0.499 were used for all simulations.

Acoustic Radiation Force Excitation

Field II[153] was used to simulate the acoustic intensity fields associated for a Siemens VF7-3 linear transducer (Siemens Medical Solutions USA, Inc., Ultrasound Division). The transducer was simulated as transmitting at 4.21 MHz, with a lateral focal configuration of F/1.5, and a lateral focal depth of 25 mm. This corresponds to the experimental setup currently utilized to perform VisR ultrasound.

Three-dimensional intensity fields were computed, normalized, and scaled to a peak, pulse-average intensity value of 1000 W/cm^2. The corresponding radiation body force values, as determined by Equation (4.5) assuming a tissue attenuation of 0.5dB/cm/MHz, were then converted to nodal point loads by concentrating the body force contributions over an element volume.

FEM Implementation and Data Analysis

The FEM simulations were performed using LS- DYNA (Livermore Software Technology Corporation, Livermore, CA). For each simulation, a dataset describing the axial displacements was obtained. Axial displacement versus time profiles were fit to the MSD models using nonlinear regression (fminsearch in Matlab, The MathWorks Inc., Natick, MA) to solve inversely for τ, ω, and s according to Section 7.2.

Error Assessment

To create an error correction function, the material τ values were plotted (Figure 8.2) as a function of VisR estimated τ and ω values. The resulting 3D surface was fit (Table Curve 3D, Systat, Inc., San Jose, CA) to over 3000 linear and nonlinear equations to determine one possible optimal error model, utilizing a minimum number of parameters (e.g. simplest model possible) while maximizing the model fit (R^2). The equation for the best-fit surface of Figure 8.2 was determined to be of the form:

$$\tau_{material}(\tau_{estimated}, \omega_{estimated}) = a \times \tau_{estimated} - {}^{b}/_{\omega_{estimated}} - c \tag{8.1}$$

and with coefficient values of

$$\tau_{material}(\tau_{estimated}, \omega_{estimated}) = 1.063 \times \tau_{estimated} - {}^{2.614}/_{\omega_{estimated}} - 0.01742 \tag{8.2}$$

VisR τ and ω estimates were input into Equation (8.2) to calculate “corrected τ” values.

K-Fold cross-validation is a model validation technique for assessing how the results of a statistical analysis will generalize to an independent data set. In k-fold cross-validation the data is randomly divided into k subsets, the model is fit using (k-1) subsets as the training set, and validation is performed on the one (kth) omitted subset. The procedure is then repeated k times, with each of the k folds used exactly once as validation data.[154] K-fold validation (k=10)

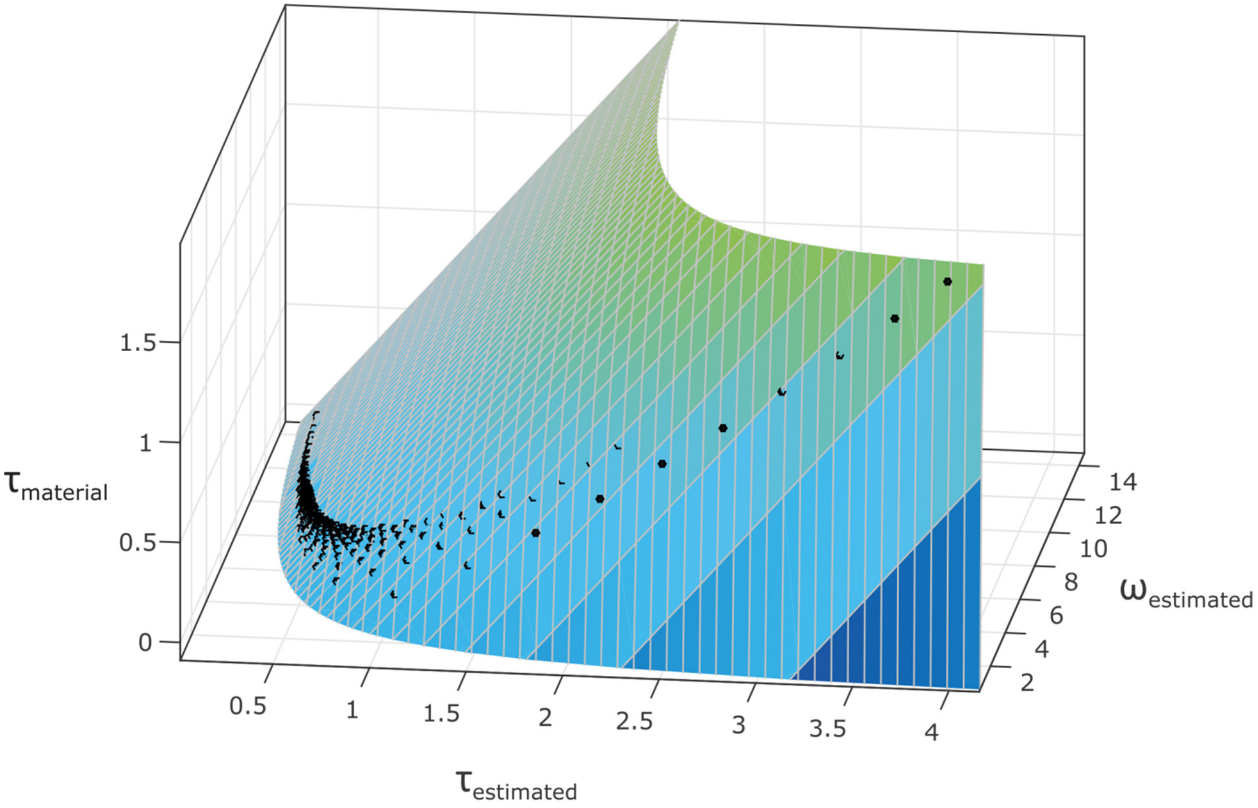

Figure 8.2: True material τ plotted as a function of the estimated τ and ω material parameters. The resulting 3-dimensional surface fits the error data well, $R^2 = 0.999$.

was performed on the simulated measurements to validate the error correction function and determine the stability of the coefficients in Equation 8.1.

8.2.2 Experimental Validation with Optical Tracking

Optical Phantom Construction

A translucent, gelatin-based, tissue-mimicking phantom was constructed according to Czernuszewicz et al.[151] The phantom recipes consisted of the following ingredients: type-A gelatin (Acros Organics, Geel, Belgium), agar (Fisher Scientific, Fair Lawn, New Jersey, USA), black polystyrene microspheres (10-µm, Polysciences Inc., Warrington, Pennsylvania, USA), n-propanol, and deionized water (concentrations are given in Table 8.1). The agar powder was

Table 8.1: Phantom Ingredients

Type-A gelatin (g)	12
n-propanol (mL)	10
Water (mL)	190
Agar (g)	1
Polystyrene microspheres (drops)	10

added to each phantom for acoustic scattering while the polystyrene beads served as markers for optical tracking.

Experimental Setup

VisR was implemented using a Siemens Acuson Antares Scanner, specially equipped for research purposes, and a VF7-3 transducer (Siemens Medical Solutions, UNC Inc. Ultrasound Division). VisR was implemented using two 300- cycle ARF excitations, separated by 0.6 ms in time and delivered to the same region of excitation. Two different focal configurations of the ARF excitations were employed (F/1.5 and F/3) in order to vary the volume of displaced tissue.

The experimental setup used to achieve optical tracking of ARF-induced displacement is shown in Figure 8.3 and is described by Czernuszewicz et al.[151] The optical focus of a microscope fitted with a 10x objective and coupled to a 150 kHz Fastcam SA1 high-speed camera (Photron USA Inc., San Diego, California, USA) was aligned with the acoustic focus of the ultrasound transducer using a needle hydrophone.

The high-speed camera was configured to acquire frames at a 150 kHz frame rate, across a 128 × 128 pixel FOV. VisR was performed for 10 different polystyrene beads within the phantom. Optical motion tracking was performed by 2D normalized cross-correlation. Optically tracking displacement versus time profiles were fit to the MSD to estimate τ, ω, and s and Equation (8.2) was used to calculate a corrected τ value.

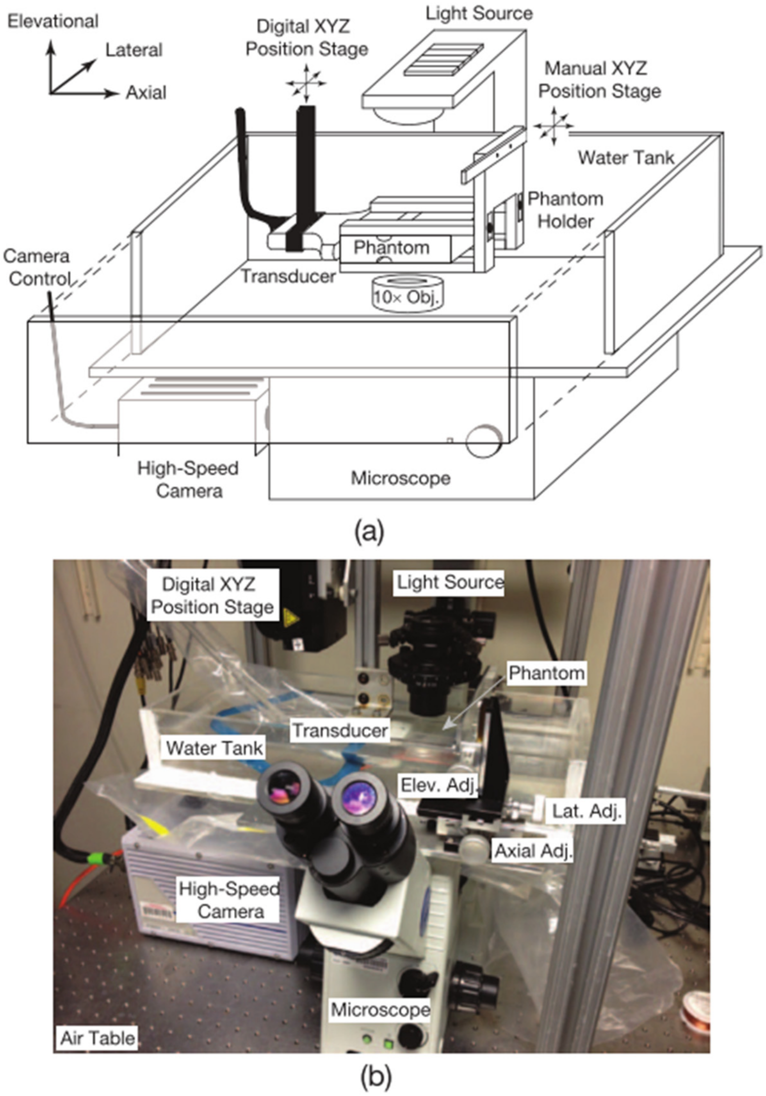

Figure 8.3: Schematic of experimental setup is shown in (a) with a photograph of the actual setup in (b).

Statistical Analysis

Descriptive statistics are expressed as mean ± SD. The statistical significance was assessed using the Wilcoxon two-sample test.

8.3 Results

8.3.1 FEM Results

Figure 8.4 shows representative ‘uncorrected’ τ estimates measured at the axial focus of viscoelastic materials. As the elasticity was increased in materials with a constant viscosity of 2.5 Pa·s (panel a), τ estimates decreased as expected. Similarly, when holding the elasticity of the materials constant at 15 kPa, τ estimates increased with increasing viscosity. However, when plotted relative to the real τ of the material, as shown in Figure 8.5, uncorrected τ estimates exhibited large errors from the real material τ. Estimated τ had a median error of 373.7%. The largest error in estimated τ was 4067% and occurred in the 100 kPa, 0.5 Pa·s material, where τ was estimated as 0.208 ms in this 0.005 ms material.

The accuracy of τ estimates was significantly improved after applying the error correction function. Corrected τ estimates are shown in Figure 8.6. After applying Equation (8.2), τ in the 100 kPa, 0.5 Pa·s was 0.019 ms reducing the error to 318%. The median error across all

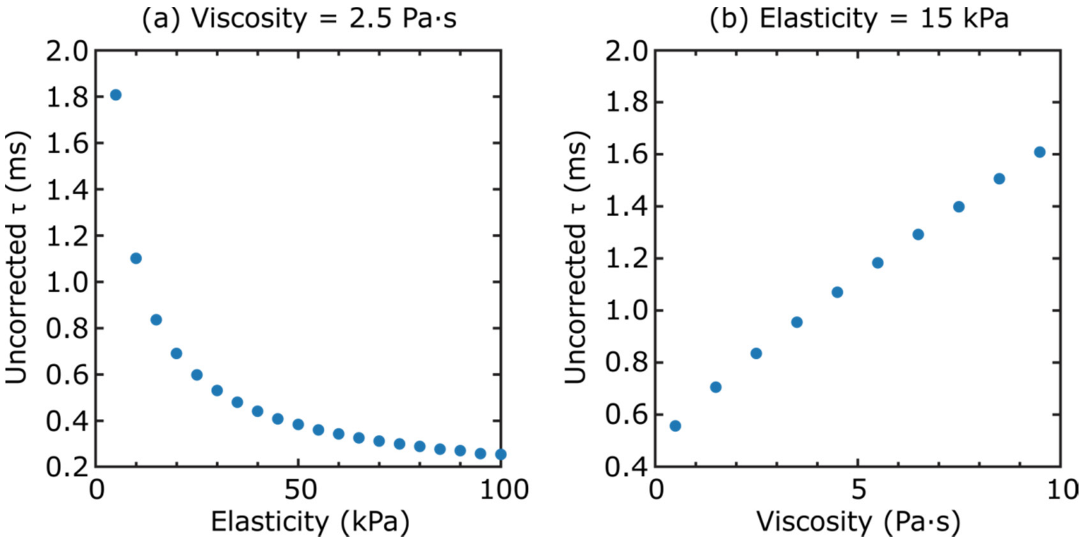

Figure 8.4: Plot of uncorrected τ estimates when (a) the viscosity is held constant (2.5 Pa·s) and elasticity is increased and (b) the elasticity is held constant (15 Pa·s) and viscosity is increased. Estimates of τ trend as expected for the ratio of viscosity to elasticity.

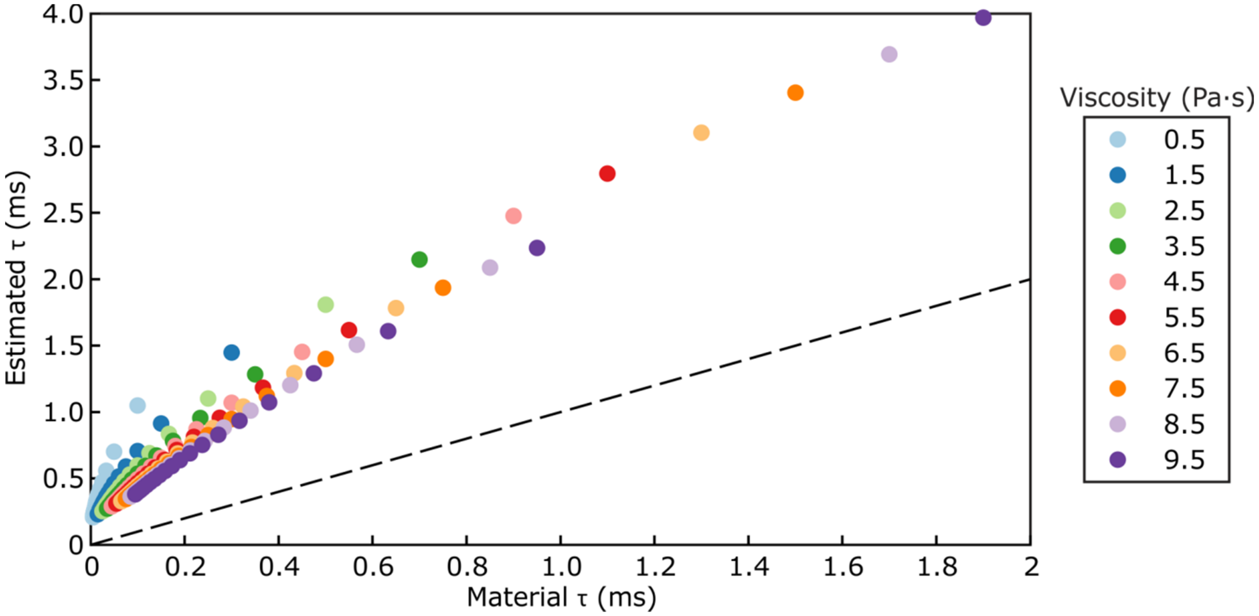

Figure 8.5: Uncorrected τ estimates in the 200 simulated viscoelastic materials plotted relative to the real τ of the material. The viscosity of the material is indicated by color and the dashed black line indicates the line of equality. Uncorrected τ estimates were overestimated from the material τ and had a median error of 373.7%.

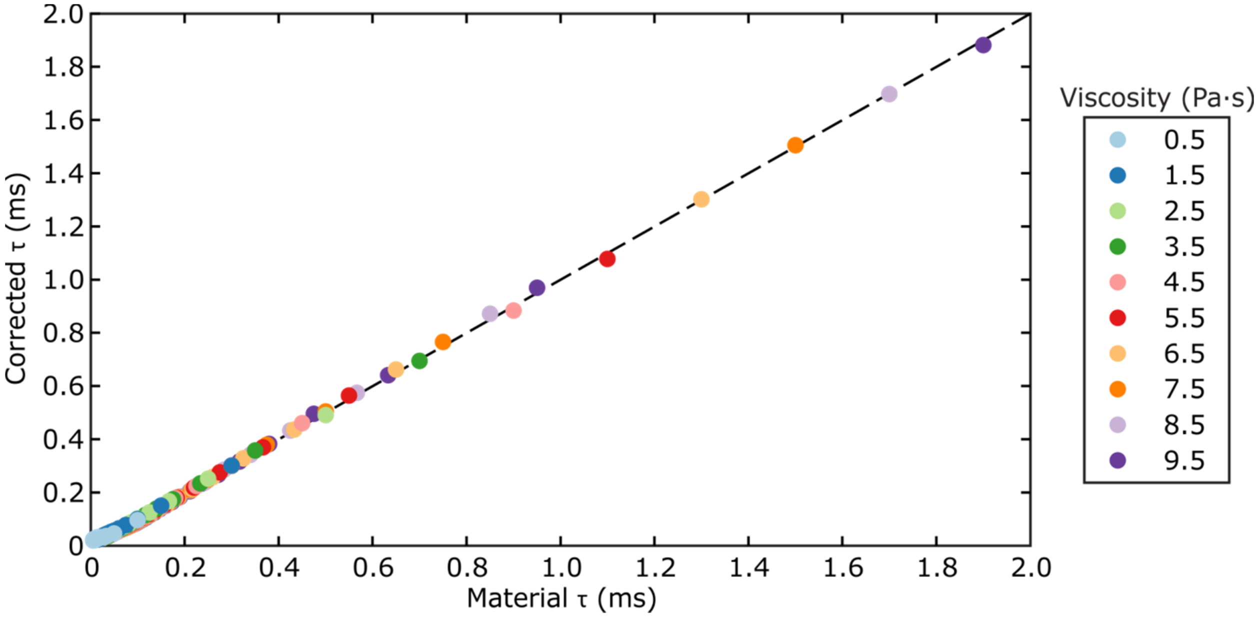

Figure 8.6: τ estimates in the 200 simulated viscoelastic materials after applying the error correction function plotted relative to the real τ of the material. The viscosity of the material is indicated by color and the dashed black line indicates the line of equality. The difference between estimated τ measurements and the τ values of the materials was significantly reduced. The median error in corrected τ values across all materials was 5.1%.

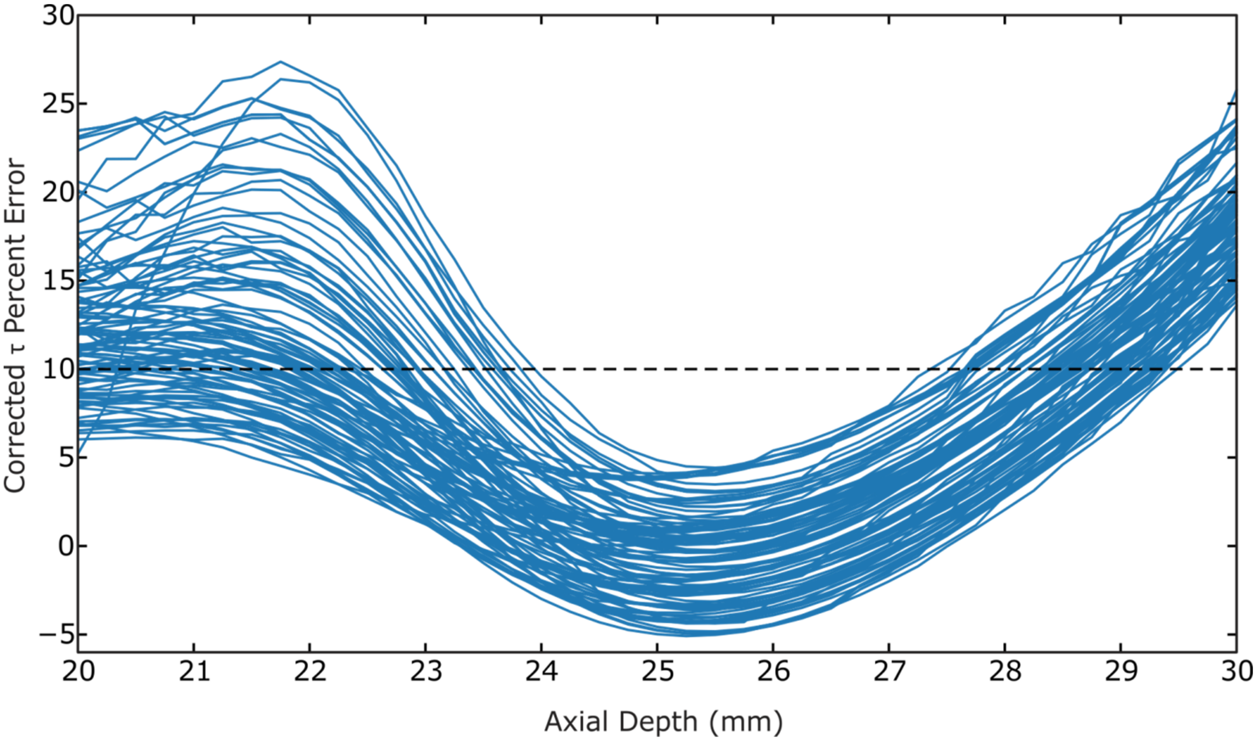

Figure 8.7: Corrected τ versus axial depth in the 200 simulated viscoelastic materials, where ARF excitations were focused at 25 mm. Corrected τ was within 10% of the material τ for 3.33 ± 2.43 mm above the focus and for 3.35 ± 0.54 mm below it.

materials was reduced to 5.1%. Error in the corrected τ measurement across axial depth is demonstrated in Figure 8.7. In the 200 simulated materials, corrected τ was within 10% of the true τ value for 6.68 ± 2.75 mm.

The results of performing k-fold validation with k=10 on the simulated measurements is shown in Figure 8.8. The coefficients of the best-fit 2D plane where evaluated in each fold: *a* ranged from 1.0516-1.0688 with a median of 1.0628 (panel a), *b* ranged from 2.5707- 2.6394 with a median of 2.6124 (panel b), and *c* ranged from 0.0162-0.0185 of 0.0174 (panel c). These values were all consistent with Equation (8.2), which was determined by fitting the surface to the full data set. The median error of the corrected τ in the validation subsets ranged from 8.1%-12.8% in the 10 different validation subsets (panel d).

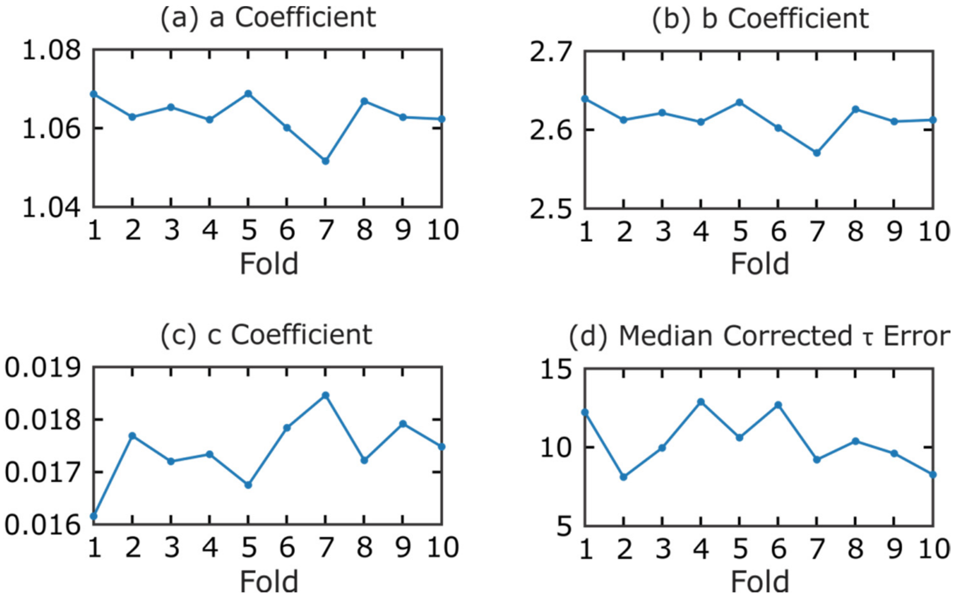

Figure 8.8: K-fold cross validation (k=10) on the dataset consisting of 200 (simulated) VisR τ and ω estimations and the real material τ. Panels (a)-(c) show the a, b, and c coefficients for the best-fit plane corresponding to Equation (8.1) for the data in the training set. In panel (d) the median error for the validation set in each fold ranged from 8.1%-12.8%.

8.3.2 Experimental Results

Figure 8.9 shows the experimental results of VisR in a gelatin phantom using a high-speed camera to optically track the ARF induced displacements. Panel a shows representative axial displacement profiles versus time using an F/1.5 (blue) and F/3.0 (red) focal configuration, and their associated MSD model fits. The uncorrected τ estimates averaged across the 10 optical beads were averaged and are shown in panel b. The estimates of τ when using an F/1.5 focal (blue) configuration for the ARF excitation were 0.568 ± 0.085 ms, which were statistically significantly smaller ($p<0.01$) than the τ estimates obtained using an F/3.0 focal (red) configuration, measured as 0.816 ± 0.037 ms. The effect of applying Equation (8.2) to account for error in the experimental τ measurements is shown in panel c. Corrected τ estimates using the F/1.5 configuration (0.418 ± 0.064 ms; blue) were consistent ($p>0.59$) with the F/3.0 corrected τ estimates (0.439 ± 0.046 ms; red).

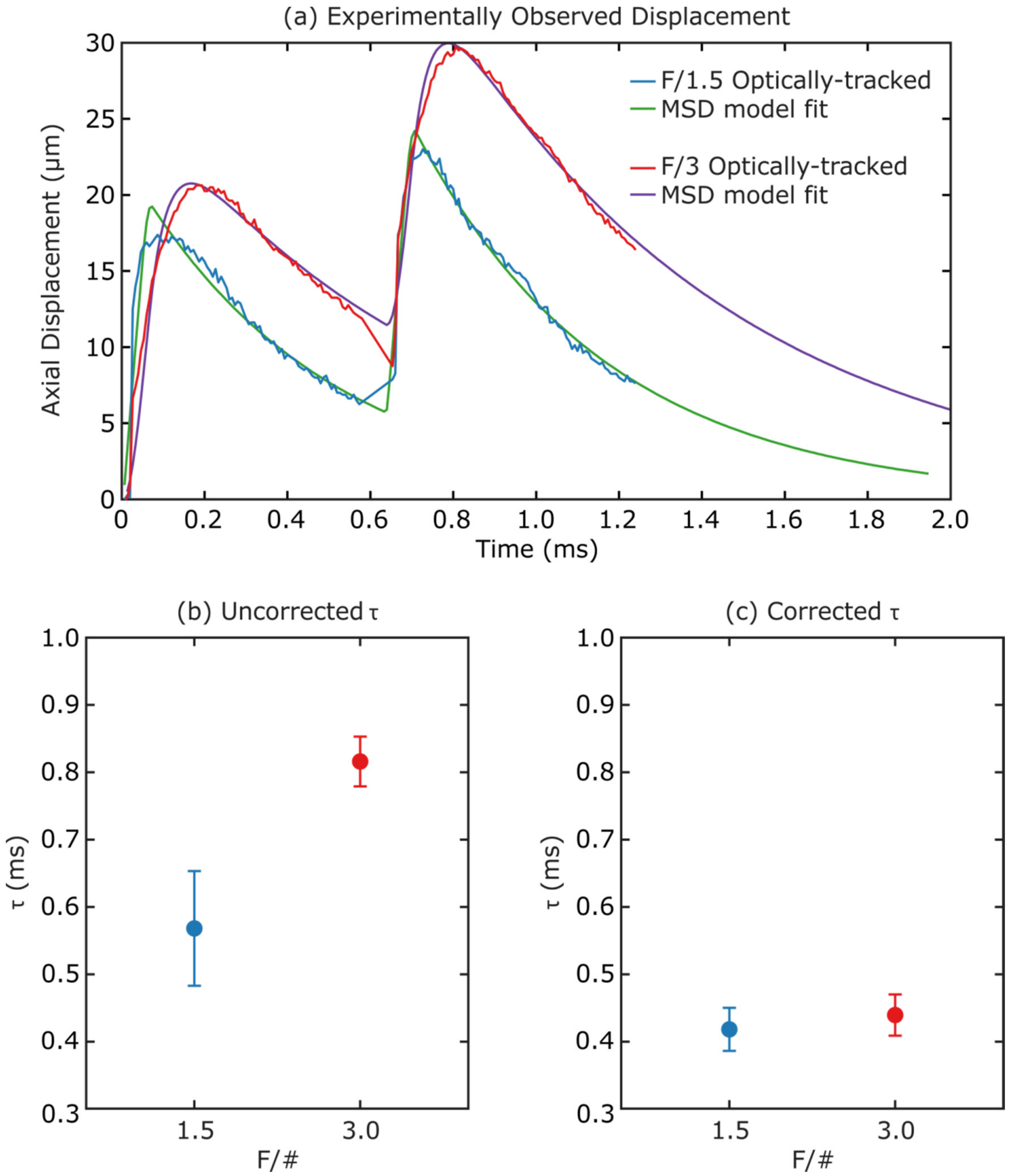

Figure 8.9: (a) Optically tracked displacement in a gelatin phantom using an F/1.5 (blue) or F/3 (red) focal configuration and the displacments predicted by the MSD model (F1.5-green, F/3-purple). (b) Uncorrected τ was 0.568 ± 0.085 ms and 0.816 ± 0.037 ms using the F/1.5 and F/3 focal configurations respectively. (c) After applying error correction function, estimated τ values were 0.418 ± 0.064 ms with the F/1.5 and 0.439 ± 0.046 ms using the F/3.

8.4 Discussion

The primary aim of this chapter was to determine whether VisR ultrasound could produce quantitative estimates of τ, the ratio of viscosity to elasticity, when using a volumetric ARF body force to induce displacement. Using FEM, VisR was simulated in 200 viscoelastic materials, and estimations of τ and ω were generated. These data showed that differences in the viscoelastic properties of tissues were reflected by differences in τ estimates (Figure 8.4). However, there was not a 1-to-1 correlation between the τ measurements estimated by VisR and the real τ values of the materials (Figure 8.4). In order for VisR estimates of τ to be quantitative, inaccuracy in the modeled forcing function was mitigated using an error correction function.

The error correction function was obtained by fitting a 2D plane to VisR estimates of τ and ω and the true material τ in 200 representative viscoelastic materials. The k-fold validation of the function, where the training and testing datasets were independent, produced consistent coefficients and only a modest increase in error (Figure 8.8). The mathematical reasoning for the form of the error correction function and the specific relationship between the three parameters is currently unknown. A more systematic approach of modeling the volumetric body force as a Gaussian with increasing height and width[155] may bridge the gap in understanding between the single node force from Chapter 7, which produced accurate estimates of τ without any correction, and the approximated ARF body force, which did not.

VisR with τ correction was demonstrated for proof of feasibility in a gelatin phantom. In order to obviate the confounding effects of acoustic tracking (see Chapter 9), optical tracking of the acoustically-induced displacements was performed. It was hypothesized that the increased volume of the F/3 configuration would be associated with more force propagation through the medium to the tracking focal position and, thus, greater extension of the excitation force, resulting in increased VisR estimated τ over the F/1.5 focal configuration. Indeed, uncorrected τ was estimated to be larger in the F/3.0 focal compared to the F/1.5 configuration. After applying the correction function, the estimates were consistent between the two configurations.

8.5 Conclusion

This chapter examined the effect of a volumetric ARF body force excitation on VisR estimates of τ. The magnitude of the error in τ measurements was assessed and the possibility for correction of this error was investigated. While correction of VisR estimated τ values was possible using the true ARF-induced displacement, VisR, when performed experimentally, will operate on acoustically tracked ARF displacements. The effect of ultrasonic tracking on VisR estimates of τ will be discussed in Chapter 9.

CHAPTER 9

Ultrasonic Tracking of Displacements in VisR Ultrasound

9.1 Introduction

Because VisR operates by fitting ARF-induced displacements to the mass-spring-damper (MSD) model, its ability to estimate τ is directly dependent on its ability to measure tissue displacement. Unfortunately, VisR, like other ARF-based applications, suffers from displacement underestimation errors.

Displacement underestimation is a result of using an acoustic pulse to generate force in tissue. As the applied force is proportional to the time-averaged acoustic intensity, the axial displacement generated by ARF is non-uniform and highly dependent on the focal configuration of the pulse.[156] When tracking ARF-induced motion using conventional B-Mode style pulses, the measured displacements will correspond to the average displacement of the scatterers within the tracking resolution cell. Because the scatterers centered within the pushing pulse will experience more force than the those at the resolution cell edges, the measured displacement will underestimate the full extent of the displacement experienced by the center scatterers.[151,157,158] Figure 9.1(a) depicts scatterers in the ROE within the tracking resolution cell at the time of peak displacement and the corresponding displacement estimate. Displacement underestimation error can be lessened by broadening the focus of the pushing beam relative to the tracking beam in order to achieve more uniform scatterer displacement

---

within the tracking resolution cell. However, due to the fixed elevation focus of linear array transducers, the focal configurations of the pushing and tracking beam will be matched in elevation, making it difficult to confine the tracking beam to a region of uniform scatterer displacement within the ROE.

Outside the ROE, displacements occur as a result of shear waves that propagate radially out from the ROE. As shear waves travel through a viscoelastic medium, the width of the wave will spread out laterally and elevationally[140] leading to more uniform scatterer displacement within the tracking resolution cell. Figure 9.1(b) depicts scatterers located lateral to ROE at the time of the elevational peak displacement of the shear wave. We hypothesize that monitoring

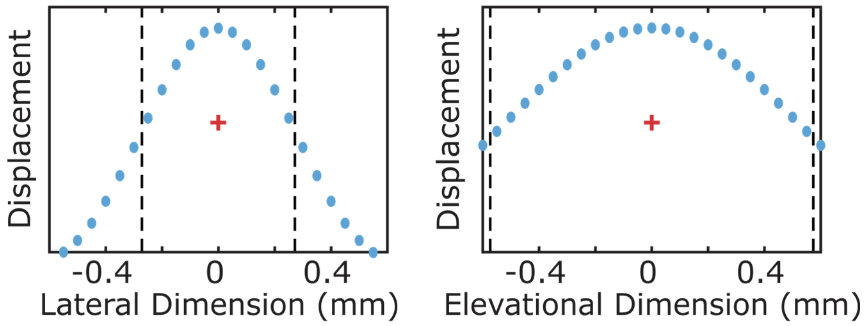
(a) Inside ROE

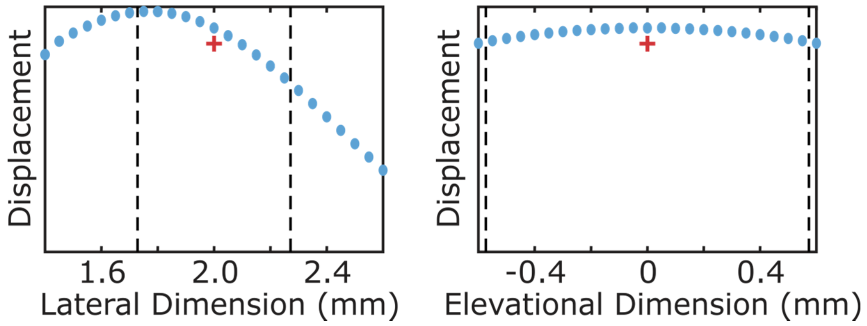
(b) Outside ROE

Figure 9.1: A depiction of the relationship between scatterer displacement and the ultrasound beam used to track the tissue inside the ROE (a) and outside the ROE (b). The scatterers are represented by the blue ellipses, the full-width-half-max of the tracking beam is represented by dashed black lines, and the measured displacement is represented by the red '+' symbol. Scatterer displacements are shown to be more uniform outside the ROE than inside the ROE, resulting in less peak displacement underestimation. Data generated by FEM and Field II simulation.

deformation outside the ROE will provide better estimates of the axial displacement and produce τ measurements that more closely represent the material. In this Chapter, ultrasonic displacement tracking is simulated in order to investigate the impact of displacement underestimation on VisR. In addition, a method of displacement underestimation correction using shear waves is demonstrated using FEM simulation and experiments in a tissue-mimicking phantom with optical validation.

9.2 Methods

9.2.1 Simulation of Ultrasonic Displacement Tracking

A uniform scattering phantom was represented as randomly positioned point targets of equal echogenicity. These point locations were taken as the initial, pre-displacement scatterer positions. A reference RF-data tracking line was generated from these scatterer locations, using Field II to model a VF7-3 linear array transducer with an F/1.5 focal configuration and transmitting at 6.15 MHz.[153]

Displacements from the FEM simulations presented in Chapter 8 were used to translate the scatterers in three dimensions to simulate the echoes generated following the ARF excitations. In order to simulate fully-developed speckle, more scatterers were needed than nodes in the FEM mesh. Thus, scatter motion was determined by linear interpolation from the displacements of the eight nearest nodes. After repositioning all scatterers, the corresponding RF line was simulated using Field II. The process was repeated for each time step in the simulation at a pulse repetition frequency (PRF) of 11 kHz. Normalized cross-correlation of the simulated RF signals was used to estimate the displacements as in normal VisR imaging.[139]

Error Assessment

As in Section 8.2.1, an error correction function for ultrasonically-tracked VisR was determined by plotting the material τ values as a function of VisR estimated τ and ω values and fitting the resulting 3D surface to Equation (8.1). The coefficient values were determined to be:

$$\tau_{material}(\tau_{estimated}, \omega_{estimated}) = 1.156 \times \tau_{estimated} - {}^{2.573}/_{\omega_{estimated}} - 0.0042 \qquad (9.1)$$

with an R^2 value of 0.999.

9.2.2 Displacement Underestimation Correction Using Shear Waves

FEM Simulations

The FEM mesh and point loads from Chapter 8 were used to simulate tissue displacement following ARF excitations in the ROE and 4 mm lateral to it. For this analysis, radiation force excitations were applied for 70 µs and separated by 0.4–2.0 ms in time. Four different Voigt materials were simulated with elasticities of 5, 10, and 50 kPa and viscosities of 1 and 3 Pa·s.

For each material, displacements were tracked in the ROE and 4 mm lateral to the ROE. To estimate τ for each simulated material and at each tracking location, the axial displacement at the focal depth was fit to the MSD model, and Equation (8.2) was used to correct for error and determine τ.

Experimental Validation

Displacement underestimation correction was experimentally validated using a Siemens Acuson Antares Scanner, specially equipped for research purposes, and a VF7-3 transducer (Siemens Medical Solutions, Inc. Ultrasound Division). VisR was implemented using two 300-cycle ARF excitations, separated by 0.6 ms in time and delivered to the same region of excitation. ARF-induced displacement was tracked using conventional 2-cycle A-lines centered at 6.15 MHz, with a pulse repetition frequency of 20 kHz. Displacement measurements were validated using optical tracking. The experimental setup used to achieve confocal optical and acoustic tracking is described in Chapter 8. Acoustic motion tracking was performed by one-dimensional normalized cross correlation applied to the raw RF data. Similarly, optical motion tracking was performed by two-dimensional normalized cross correlation.

Optical and acoustic data were captured for 3 different beads positioned at the confocal optical and acoustic foci and with the ARF impulses focused on the bead to track displacements in the ROE or 4.25 mm lateral to the bead to track shear wave-induced displacements. Axial displacement versus time profiles were fit to the MSD model to solve for τ. No error correction was applied.

9.3 Results

9.3.1 Ultrasonic Displacement Tracking Simulated Results

In Figure 9.2 (a), real τ values of the materials are plotted relative to the uncorrected ultrasonically-tracked τ values. Using ultrasonically-tracked displacements versus the true displacement increased the median error of τ increased from 373.7% to 435.9%. Standard deviation of uncorrected τ values relative to the axial distance overwhich it is evaluated are depicted in Figure 9.3, and are reported to range from 0.004 ± 0.002 ms over a 1 mm axial window to 0.190 ± 0.048 ms over a 20 mm axial window. Figure 9.2 (b) shows the effect of applying Equation (8.2) to the estimated τ values, reducing median error to 73.6%. Equation (9.1) reduced median error at the focus to 8.5% as shown in Figure 9.2 (c), and corrected τ to within 10% of the true τ of the material for 5.88 ± 3.91 mm as shown in Figure 9.4.

9.3.2 Displacement Underestimation Correction Results

Simulated Results

Figure 9.5 shows representative FEM displacement (dark blue lines) and acoustically tracked displacement (light blue lines) through time for the 10 kPa/1 Pa·s material with displacements tracked in the ROE (a) and 6 mm (b) lateral to the ROE. In the ROE, the tracked displacement underestimated the full extent of the axial displacement. The maximum

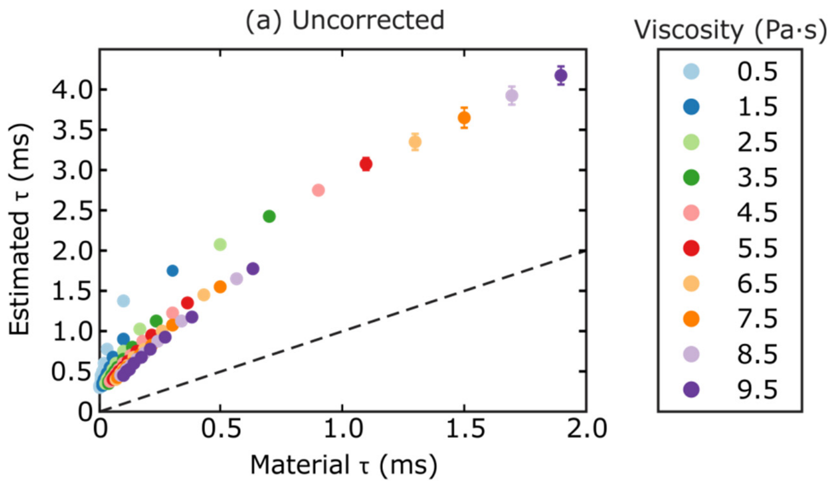
(a) Uncorrected

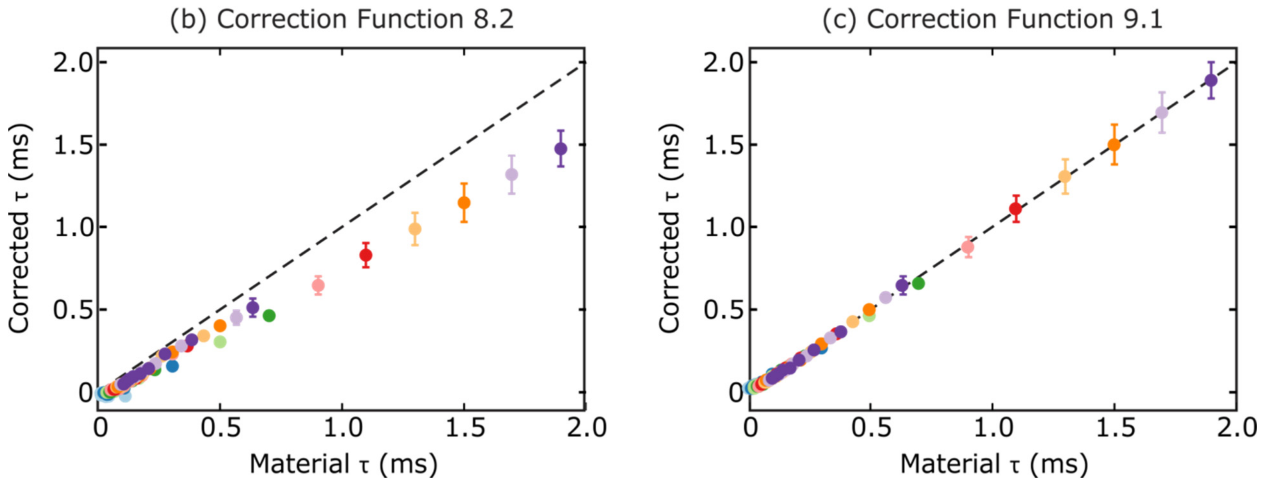
(b) Correction Function 8.2

(c) Correction Function 9.1

Figure 9.2: (a) Uncorrected τ estimates in the simulated viscoelastic materials averaged across speckle realizations and plotted relative to the real τ of the material. The viscosity of the material is indicated by color and the dashed black line indicates the line of equality. Uncorrected τ estimates were overestimated from the material τ and had a median error of 435.9%. (b) τ estimates in the simulated viscoelastic materials after applying Equation 8.2 plotted relative to the real τ of the material. Resulting τ estimates remained significantly different from true τ of the materials ($p<0.02$) with a median error of 73.6%. (c) τ estimates in the simulated viscoelastic materials after applying Equation 9.1 plotted relative to the real τ of the material. Resulting τ estimates were not significantly different from true τ of the materials ($p=0.9$) and had a median error of 8.5%.

acoustically tracked displacement following the first push was 67.21 ± 12.55% of the FEM displacement. When tracking shear wave-induced displacement outside the ROE, the acoustic tracking underestimation error was diminished. The percentage of maximum displacement following the first ARF excitation measured increased to 101.52 ± 9.84% outside the ROE.

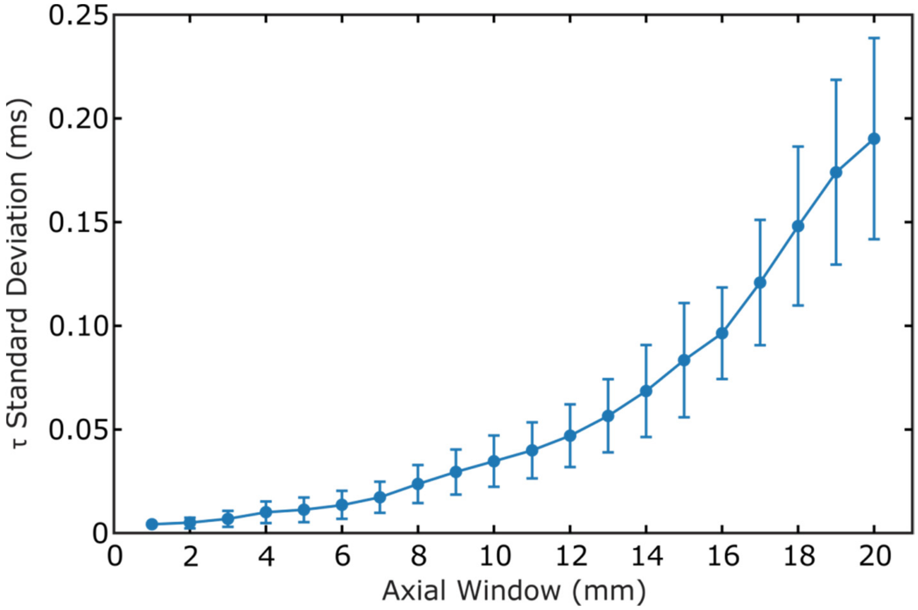

Figure 9.3: Standard deviation of uncorrected τ estimates evaluated at axial windows surrounding the focus and ranging from 1 mm to 20 mm. Standard deviation ranged from 0.004 ± 0.002 ms over a 1 mm axial window to 0.190 ± 0.048 ms over a 20 mm axial.

The effect of displacement underestimation is reflected in VisR-derived τ measurements, shown in Figure 9.6 (a). In all simulated materials, VisR-derived τ estimates from displacements in the ROE were higher than the true value. Error in τ measurements ranged from 0.041 ± 0.025 ms in the 50 kPa/1 Pa·s material to 0.251 ± 0.097 ms in the 5 kPa/3 Pa·s material. Figure 9.6 (b) shows the τ estimates when tracking displacements outside the ROE. Error in τ estimates was reduced to 0.006 ± 0.002 ms in the 50 kPa/1 Pa·s material and 0.019 ± 0.001 ms in the 5 kPa/3 Pa·s material.

Experimental Results

Figure 9.7 (a) shows the optically and acoustically tracked displacement profiles for the bead in the ROE. The acoustically tracked displacements were 64.30 ± 16.95% of the maximum displacement measured by the optical gold standard. Using the optically tracked displacements, τ values were 0.75 ± 0.07 ms, which were significantly smaller ($p<0.01$) than VisR τ estimates derived from acoustically tracked displacements (1.40 ± 0.03 ms).

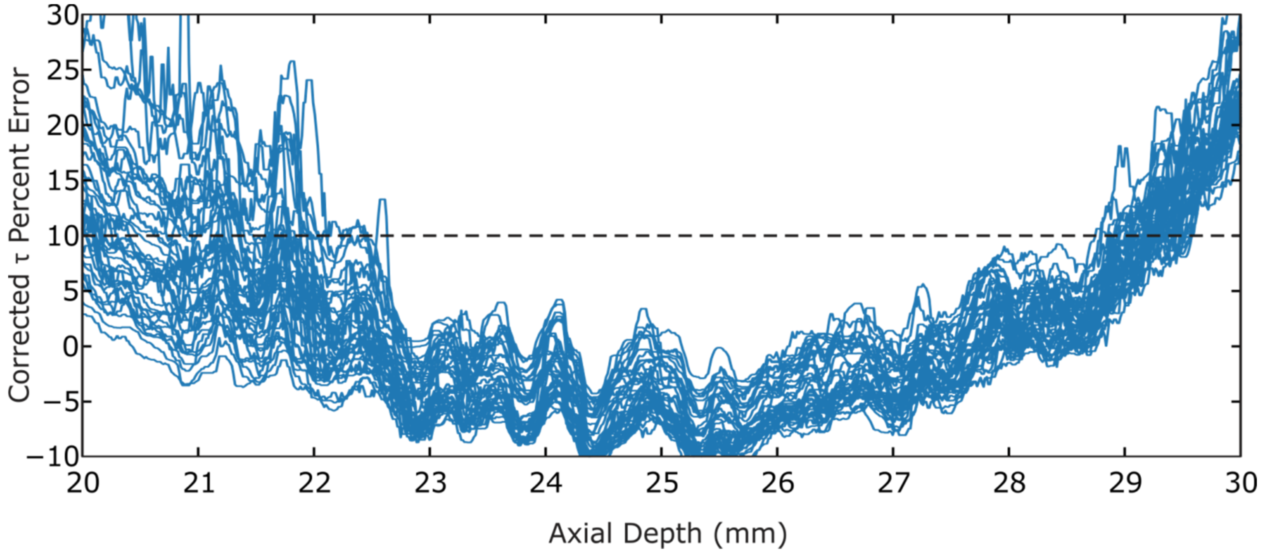

Figure 9.4: Corrected τ versus axial depth in the all simulated viscoelastic materials, where ARF excitations were focused at 25 mm. Corrected τ was within 10% of the material τ for 5.88 ± 3.91 mm.

Optically and acoustically tracked displacements induced by shear waves are plotted in Figure 9.7 (b). The acoustically tracked maximum displacement measured 4.25 mm outside the ROE were 98.044 ± 5.122% that of the optically tracked maximum displacement. Optically, τ was measured to be 0.76 ± 0.05 and acoustically measured to be 0.75 ± 0.09 ms. Not only are the optically- and acoustically-derived estimates of τ made outside the ROE consistent with each other (p=0.94), they are also consistent with the optically-derived τ measurement made in the ROE (p>.83) in the homogeneous phantom.

9.4 Discussion

This chapter investigated whether VisR ultrasound could produce quantitative estimates of τ when using a volumetric ARF body force to induce displacement and using ultrasound pulses to track displacements. Ultrasonic displacement tracking was simulated using Field II and was used to generate estimations of τ and ω. These data show that the error correction function generated in Chapter 8, can be adapted to correct for error in VisR τ estimates generated from ultrasonically-tracked data.

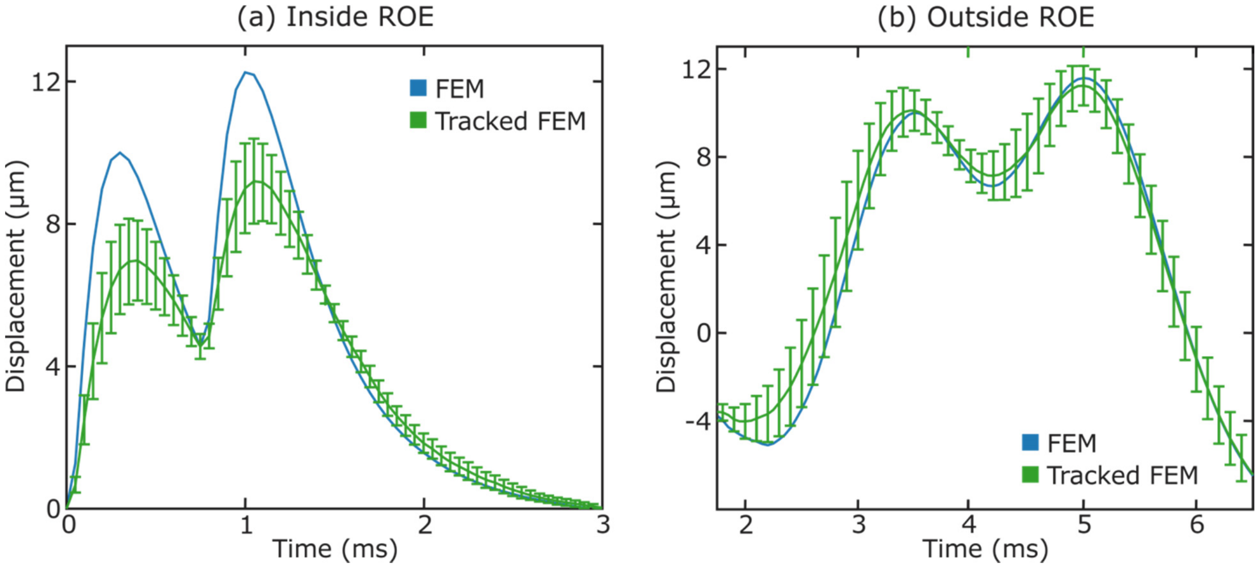

Figure 9.5: Displacement through time for the 10 kPa/1 Pa·s material with displacements tracked either in the ROE (a) or 4 mm outside the ROE (b). FEM displacements are represented by the blue lines, and acoustically tracked data are represented by the green lines. Note that displacement underestimation is larger when tracking displacements inside the ROE than outside it, and while larger, jitter is more constant through time when tracking displacements outside the ROE. Data generated by FEM and Field II simulations.

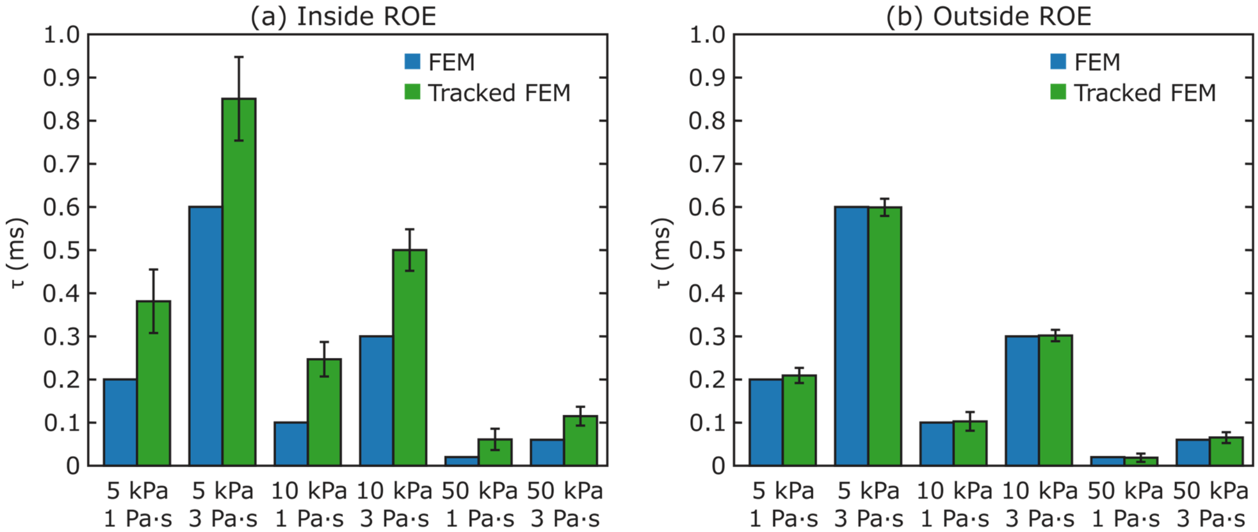

Figure 9.6: True τ of the modeled material (blue) compared to the VisR τ values (green) computed from displacement profiles tracked (a) inside and (b) outside the ROE. Error bars indicate one standard deviation. Values of τ generated inside the ROE were overestimated by at least 0.04 ms. Outside the ROE mean τ was within 0.01 ms of the true τ for all materials.
Data generated by FEM and Field II simulations.

While the correction function was shown to significantly reduce error at the focal depth, its use for correcting error τ above and below the axial focus is limited. As shown in Figure 9.4, there was a 5.88 ± 3.91 mm window over which corrected τ estimates were within 10% of the true material τ. While this may be relevant for applications where focal tissue characterization is meaningful, such as staging liver fibrosis,[159,160] it is not relevant for applications such as DMD, where 2D imaging is necessary to appreciate the heterogeneity of the disease process. In order to extend this correction function to 2D imaging, multiple focal depths would be needed.

Rather than correcting for both displacement underestimation and the inaccuracy in the modeled forcing function, this chapter also demonstrated displacement underestimation in, versus outside of, the ROE and the associated impact on VisR derived τ estimates. These data show that displacement underestimation leads to error in τ measurements in FEM simulations when tracking displacements in the ROE. However, tracking displacements outside the ROE improved both the displacement estimates and τ measurements. These FEM results were supported by results in the gelatin phantom with optical tracking.

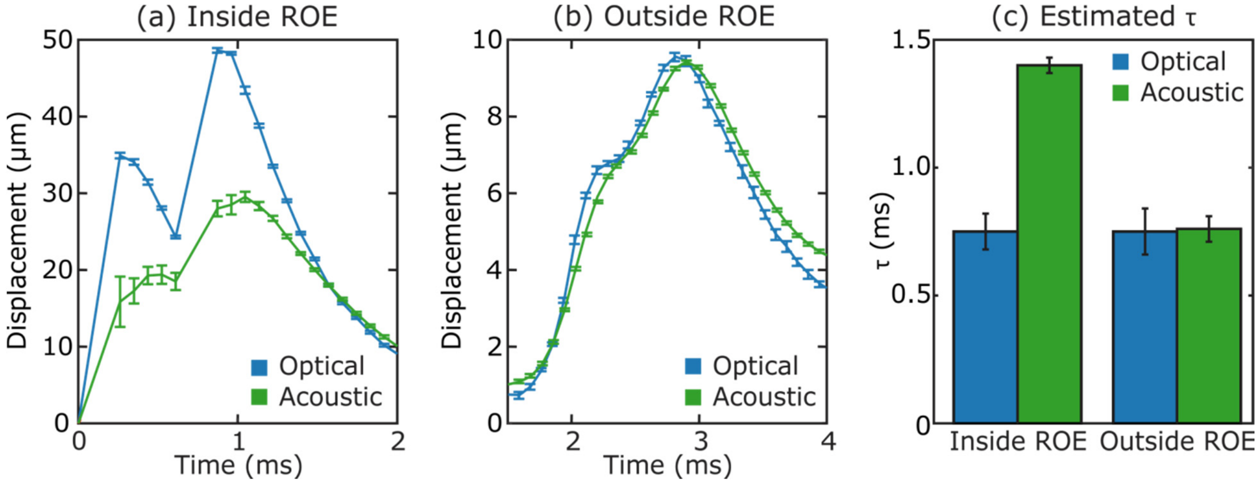

Figure 9.7: Displacement through time measured optically (blue) and acoustically (green) for displacements tracked (a) inside and (b) outside the ROE. The associated τ measurements inside and outside the ROE are shown in (c). Acoustically-derived τ estimates were significantly higher than the optically-derived τ estimates when displacements were tracked inside of the ROE but comparable when tracked outside of the ROE. Moreover, optically-derived τ estimates were consistent inside and outside the ROE in the homogeneous phantom. Data generated experimentally using confocal ultrasound and optical imaging.

One of the main challenges associated with performing VisR using shear waves involves the choice in distance from the ROE to monitor displacement. If shear waves are tracked too close to the ROE, they will not have time to spread out, and little improvement in displacement tracking will be appreciated. However, shear waves tracked too far from the ROE may suffer from low signal-to-noise ratios (SNR) due to attenuation, causing error in displacement estimates and the model fit. *A priori* knowledge of the approximate mechanical properties of the tissue may inform the choice of tracking location. Furthermore, this challenge could be addressed using plane wave tracking methods which are capable of monitoring the deformation response simultaneously across a large field of view.

9.5 Conclusion

Acoustic displacement underestimation in VisR was shown in FEM simulations. The magnitude of the error in τ measurements due to both ultrasonic displacement tracking and volumetric ARF impulses was assessed and the possibility for correction of this error was investigated. In addition, displacement underestimation was mitigated by tracking displacements induced by propagating shear waves outside the ROE.

In concert with inertia compensation (Chapter 7), quantitative assessment of τ can be achieved over a narrow axial range either by applying a correction function which accounts for both non-modeled force propagation and acoustic displacement underestimation, or by minimizing acoustic displacement underestimation by exploiting shear wave propagation and correcting for non-modeled force propagation (Chapter 8). Although τ, the ratio of viscosity coefficient to elastic modulus, may be quantitatively evaluated by VisR, *isolating* viscous and elastic material properties may only be qualitatively performed, which is the subject of Chapter 10.

CHAPTER 10

Distinguishing Viscous from Elastic Properties in VisR Ultrasound

10.1 Introduction

It has been demonstrated that VisR can be used to quantitatively estimate τ in viscoelastic material, but because τ is a ratio, it cannot differentiate changes in elasticity from changes in viscosity. To isolate elastic from viscous material properties, the MSD model may be fit to VisR displacement data to solve for the elasticity and viscosity of the material relative to the magnitude of the applied radiation force (μ/A and η/A, respectively). Because these parameters depend on the ARF amplitude (A), which is unknown but assumed to be constant over the measurement region, these parameters will herein be referred to as the 'relative elasticity' and 'relative viscosity.' It is hypothesized that, although qualitative, the relative elasticity and relative viscosity can provide greater differentiation of viscoelastic materials than τ measures alone. The significance of measuring relative elasticity and viscosity, in addition to τ, in VisR ultrasound is demonstrated in simulated and experimental data.

10.2 Methods

10.2.1 FEM Simulations

The FEM mesh and point loads that were presented in Chapter 8 were again used to simulate VisR in viscoelastic materials. ARF excitations were applied for 70 μs and separated by 0.8 ms in time.

The built-in material model *MAT_KELVIN_MAXWELL _VISCOELASTIC was used to model tissue as a viscoelastic, isotropic material. Elasticities were varied from 10 kPa to 100 kPa (steps of 10 kPa), and viscosities were varied from 2 Pa·s to 12 Pa·s (steps of 1 Pa·s) for a total of 110 simulated materials. Simulated materials were modeled as nearly incompressible, using a Poisson's ratio of 0.499, and had a density of 1.0 g/cm^3. For each simulated material, axial FEM displacements at the focus were fit to the MSD model, and error in τ was corrected for using Equation (8.2).

10.2.2 Experimental Validation in Gelatin Phantom

Experimentally, imaging was performed on a gelatin tissue-mimicking phantom containing a spherical inclusion. The spherical inclusion phantom was constructed by filling a latex balloon with 8.2% gelatin gel (by mass) and embedding it in a 10 cm diameter × 6 cm height cylinder of 16.5% gelatin gel.

Data was acquired using a Siemens Acuson Antares™ imaging system specially equipped for research purposes (Siemens Medical Solutions USA, Inc. Ultrasound Division) and a VF7-3 transducer. VisR was implemented using two ARF excitations of 300 cycles spaced 0.8 ms apart in time, with a center frequency of 4.21 MHz. Motion tracking was performed at 6.15 MHz with a pulse repetition frequency (PRF) of 11 kHz. Both ARF and tracking pulses were focused axially at 34 mm and used an F/1.5 focal configuration. This beam sequence was repeated in 40 lateral locations spanning a 2 cm lateral field of view to generate a two-dimensional image. Motion tracking was performed on the RF data using one-dimensional cross-correlation in the axial dimension between sequentially acquired tracking lines.

Statistical Analysis

Regions of interest spanning 5 mm laterally and 4 mm axially were selected inside and outside the inclusion. Descriptive statistics of the parameter are expressed as mean ± SD. Contrast-to-noise ratio (CNR) for the inclusion relative to the background was calculated as

$$CNR = \frac{|\mu_i - \mu_b|}{\sqrt{\sigma_i^2 + \sigma_b^2}} \tag{10.1}$$

where means are denoted by μ_i and μ_b, and standard deviations are denoted by $\sigma_i$and σ_b of the parameter inside and outside the lesion, respectively.

10.3 Results

10.3.1 FEM Results

VisR derived measurements of relative elasticity, relative viscosity, and τ in materials with the same elasticity and viscosities ranging from 2-12 Pa·s, are plotted against the material elasticity in Figure 10.1. Relative elasticities were statistically significantly different ($p<0.02$) between all material stiffnesses (panel a). Relative viscosity (panel b), however, were similar for all ten elasticities ($p>0.88$). In addition, due to the large range of viscosities, there was substantial overlap in τ measurements between materials with different elasticities (panel c).

In Figure 10.2, values were grouped according to the material viscosity. Measured relative elasticity (panel a) was consistent for all investigated viscosities ($p>.79$). Conversely, statistically significantly different relative viscosity (panel b) were measured in the measured in materials with different viscosities ($p<0.05$). Estimates of τ (panel c) could not differentiate between viscosities across the full range of elasticites ($p>0.02$).

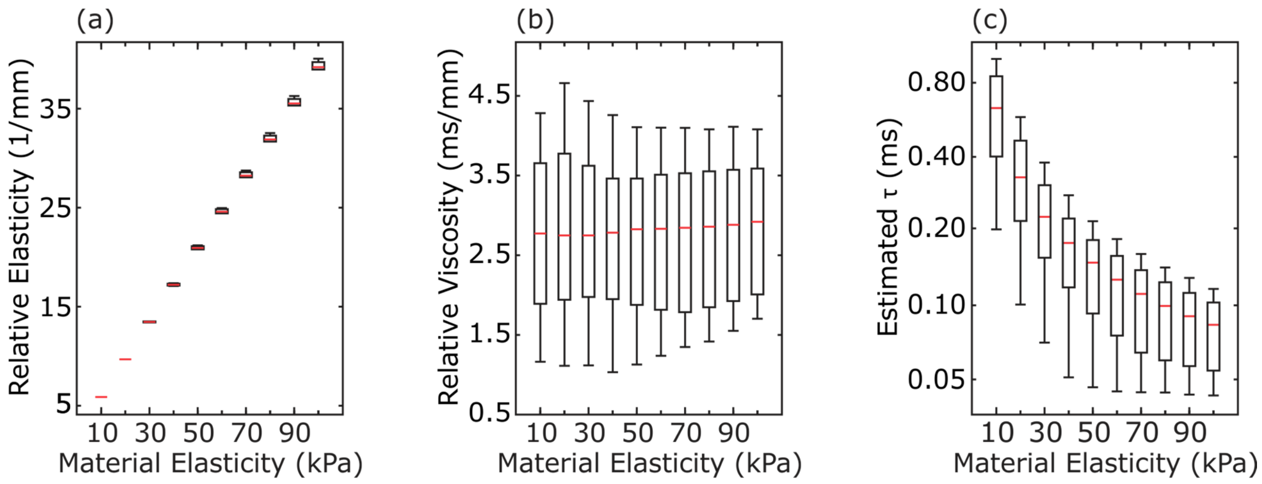

Figure 10.1: Box-and-whisker plots of measured (a) relative elasticity, (b) relative viscosity, and (c) τ for materials grouped by elasticity and with viscosities ranging from 2-12 Pa·s. The red horizontal line indicates the median, the box covers the 25-75% percentiles, and the whiskers span the range of the observed τ measurements. Relative elasticities were significantly different between materials with different elasticities ($p<0.05$), while relative viscosities were not ($p<0.05$). There is substantial overlap in τ values measured in materials with different elasticities relating to the large range of material viscosity.

10.3.2 Experimental Results

VisR derived τ, relative elasticity, and relative viscosity imaging results in the gelatin phantom are shown in Figure 10.3. In the estimated τ image (panel a) the inclusion is evident as the structure spanning 20 to 40 mm axially and -10 to -3 mm laterally. Estimated τ in the inclusion was 1.18 ± 0.13 ms compared to 0.78 ± 0.17 ms in the background. The inclusion is clearly delineated across its 20 to 40 mm axial range in the relative elasticity (panel b) image, with measurements in the inclusion of 40.95 ± 9.18 1/mm and outside of the inclusion of 56.63 ± 8.54 1/cm. In the relative viscosity image (panel c), the inclusion is not well distinguished from the background. Values of relative viscosity were 65.62 ± 11.56 ms/mm and 60.11 ± 20.13 ms/mm inside and outside the inclusion respectively. CNR of the lesion relative to the background was 1.15, 0.84, and 0.08 using τ, relative elasticity, and relative viscosity, respectively.

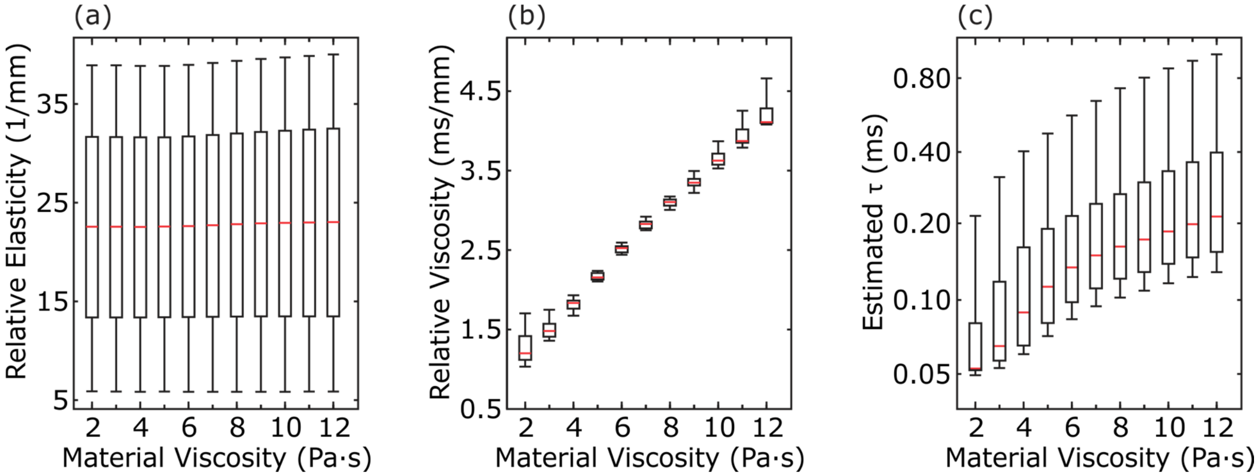

Figure 10.2: Box-and-whisker plots of measured (a) relative elasticity, (b) relative viscosity, and (c) τ for materials grouped by viscosity and with elasticities ranging from 10-100 kPa. The red horizontal line indicates the median, the box covers the 25-75% percentiles, and the whiskers span the range of the observed τ measurements. Relative elasticities were not significantly different ($p>0.05$), however, relative viscosities were significantly different between materials with the same range of elasticities and different viscosities ($p<0.05$). There was substantial overlap in τ values measured in materials with different viscosities attributable to the large range of material elasticities.

10.4 Discussion

Because it is a ratio, τ estimates will not be unique to a specific elasticity or viscosity. While differences in the viscoelastic properties of the material will manifest as differences in τ measurements, these changes cannot be attributable to either elasticity or viscosity. Relative elasticity and viscosity measurements can, however, differentiate materials based on their material elasticity and viscosity. It is important to remember that relative elasticity and viscosity are relative to the applied force magnitude and their values should only be used where the applied force can be assumed to be constant. In this sense, VisR estimates of relative elasticity and viscosity are qualitative.

Experimentally, the estimated τ values inside the spherical inclusion were higher than the τ estimates in the surrounding material. On its own, this would suggest that the inclusion had either higher viscosity, or lower elasticity than the background or some combination thereof. However, coupled with the lower relative elasticity and comparable relative viscosity

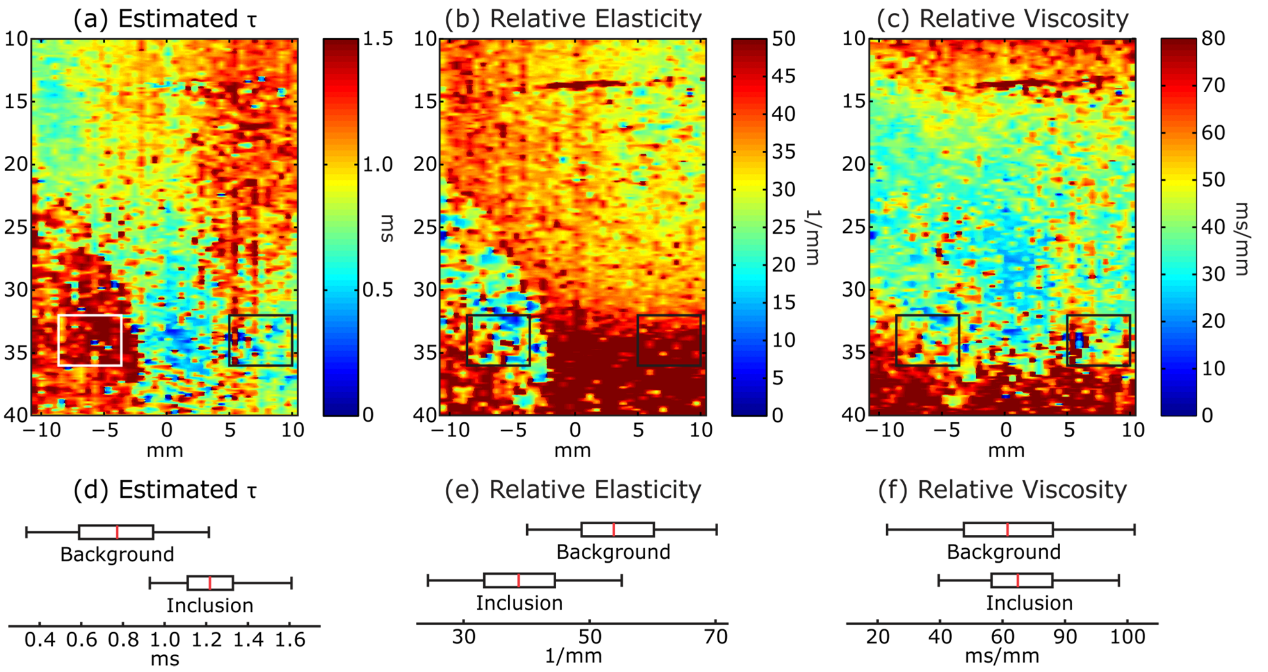

Figure 10.3: Parametric VisR images of (a) estimated τ, (b) relative elasticity, and (c) relative viscosity in a tissue-mimicking, gelatin phantom. The phantom contained a spherical inclusion with comparable viscosity but lower elasticity than the background material. Box-and-whisker plots show the median (red-line), 25th and 75th percentiles (box), and full range of observed (d) estimated τ, (e) relative elasticity, and (f) relative viscosity inside the spherical inclusion (rectangular ROI spanning from -9 to -4 mm laterally) and outside the inclusion (rectangular ROI spanning from 4 to 9 mm laterally). While VisR τ values contrast the inclusion (a & d), they do not suggest if the inclusion's mechanical property difference from the background is related to elasticity, viscosity, or both. VisR parametric relative elasticity values (b & e) reveal that there is disparity in the elastic properties of the inclusion and background, while relative viscosity values (d & f) suggests that the inclusion and background have similar viscous property.

measurements in the inclusion, the increased τ values in the inclusion can be attributed to lower elasticity of the inclusion rather than a difference in viscosity. This analysis is consistent with the higher concentration of gelation used in the formulation of the background and demonstrates the utility of separating elasticity and viscosity in order to interpret τ estimates.

10.5 Conclusion

Previous chapters have shown that VisR, an elastographic imaging method based on the MSD model, can estimate the relaxation time for constant stress (τ) in viscoelastic materials. One disadvantage to VisR (as demonstrated herein) is its inability to distinguish between the elastic and viscous contributions to τ. In this chapter, it was shown that VisR can be used to estimate the elasticity and viscosity of a material relative to the magnitude of the applied ARF. It was demonstrated in simulation and experimentally that these relative measures can be used to discriminate the viscous and elastic properties of materials.

CHAPTER 11

Noninvasive Discrimination of Muscle Degeneration in Canine Models of Duchenne Muscular Dystrophy by VisR Ultrasound

11.1 Introduction

As described in Chapter 2, Duchenne muscular dystrophy (DMD) is an X-linked disorder affecting approximately 1 of 3,500 newborn human males in whom absence of the protein dystrophin causes progressive degeneration of skeletal and cardiac muscle. [161–163] Muscle degeneration is accompanied by muscle fiber necrosis and subsequent progressive replacement of muscle by fibrous tissue and fat.[164] Because muscle mechanical properties are related to composition and structure,[165] interrogating the mechanical properties of muscle may be useful for stratifying degrees of functional muscle degeneration and support early detection of subtle degenerative changes in DMD.

In this Chapter, VisR ultrasound is applied for imaging the mechanical properties of dystrophic versus control muscles in the Golden retriever muscular dystrophy (GRMD) canine model of DMD.[56,57,166] VisR was performed in a cross-sectional study of 10 GRMD and 10 controls dogs age 3 to 60, and in a longitudinal study, where four littermates (2 GRMD, 2 control) were imaged serially over the course of 7.5 months. Imaging results were compared with MRI and morphometric histological findings.

11.2 Methods

All procedures were approved by the Institutional Animal Care and Use Committees of the University of North Carolina at Chapel Hill and Texas A&M University.

11.2.1 VisR Imaging

VisR imaging was performed *in vivo* on the rectus femoris (RF), cranial sartorius (CS), and vastus lateralis (VL) muscles. In the cross-sectional study, imaging was performed in 20 (n=10 control and 10 GRMD) age-matched dogs, with imaging time points at 3, 6, 12, 24, and 60 months of age. Because RF histology was not available for this population of dogs, results only will be presented for the CS and VL muscles. In the longitudinal study, imaging was performed serially in 4 (n=2 control and 2 GRMD) littermates over the course of a year, with imaging time points at 4.5, 6, and 12 months of age.

Dogs were sedated for ultrasound imaging using acepromazine (0.02 mg/kg IM) and butorphanol (0.4 mg/kg IM) and positioned in lateral recumbency. Imaging was performed using a Siemens Acuson Antares™ imaging system equipped for research purposes and a VF7-3 transducer (Siemens Medical Solutions USA, Inc. Ultrasound Division). One spatially registered B-Mode frame was automatically acquired immediately prior to each acquisition. VisR was implemented using two 300-cycle, F/1.5, ARF excitations (70 μs) administered 0.8 ms apart in time and delivered to the same region of excitation (ROE). Eight tracking lines were acquired between the two ARF excitations, and 48 tracking lines were acquired after the second excitation for a total of 56 tracking lines. This ensemble was repeated in 40 locations spaced 0.53 mm apart laterally for a 2.1 cm lateral field of view (FOV). The ensembles were collected using wiperblading, whereby successive ensemble acquisitions alternated from the left to the right side of the imaging FOV, to avoid motion interference. Data sets were acquired with three repeated acquisitions in immediate succession.

Acquired raw RF data was transferred to a computational workstation for processing and analysis. One-dimensional axial displacements were measured along each acquired ensemble using normalized cross-correlation.[139] The interpolation factor was 4, the search window length was 80 μm, and the kernel length was 3 times the center wavelength. Physiologic motion was rejected using a linear filter applied to the measured ARFI displacement profiles.[167]

Estimates of τ were calculated from VisR displacement profiles using the MSD model as in Section 7.2 using a custom-written C++ program. Images of τ were median filtered using a 0.29 mm (axial) by 1.06 mm (lateral) window. Analysis of VisR τ measurements were then performed by calculating the standard deviation (SD) of τ estimates within the hand-delineated muscle boundaries.

Statistical Analysis

In the cross-sectional study, SD of VisR τ estimates from the GRMD and control muscles were statistically compared using the Wilcoxon two-sample test. A p value of < 0.05 was defined as significant. Due to small sample size, no statistical analysis, was performed in the longitudinal study.

11.2.2 MR Imaging

MRI was performed at each imaging time point of the cross-sectional study and at the 6 and 12 month time points in the longitudinal study. Dogs were anesthetized and placed in ventral recumbency (prone position). The pelvic limbs were extended caudally and positioned in the head coil centered at midfemur. T2-weighted (T2w) imaging was performed using the sequencing outlined by Wang et al.[92,168] Measures of T2 inhomogeneity were also performed. Included in this chapter is run percentage (RP) which measures the number of ‘runs’, or groups of consecutive voxels of the same intensity. More heterogeneous tissue will yield a higher number of runs and a higher RP. Image analysis was performed by Dr. Jiahui Wang under the direction of Dr. Martin Styner at the University of North Carolina at Chapel Hill.

11.2.3 Histology

Muscle tissue samples of the CS and VL were acquired by open surgical biopsy at each time point in the cross-sectional study. For the longitudinal study, the RF, CS and VL muscles of the left limb were surgically biopsied at 6 months, and muscles of the right limb were harvested at necropsy (affected/carrier) or surgically biopsied (control) at 12 months of age.

Muscle sections were stained with Hemotoxylin and Eosin (H&E) and Masson's trichrome or picrosirius red for collagen. Microscopy of the stained sections was performed using an Aperio Scanscope microscope (Aperio Technologies, Vista, CA) at 20× magnification. The collagen percent and fat percent were calculated for each muscle section as demonstrated in Figure 11.1 using Aperio ImageScope software. Analysis was performed by Dr. Eric Snook under the direction of Dr. Joe Kornegay at Texas A&M University.

11.3 Results

Figure 11.2 shows representative parametric VisR τ images acquired in the rectus femoris (RF) muscle of a 12 month-old GRMD/control littermate pair and the histology harvested from the muscles shortly thereafter. Qualitatively, the VisR τ image in the GRMD RF muscle (panel a) appears more heterogeneous compared to the control RF muscle (panel b). Quantitatively, standard deviation (SD) of τ measurement was approximately 75% larger in the GRMD (panel a, 0.430 ms) than in the control RF (panel b, 0.245 ms). Histologically, the RF of GRMD dog (panel c) shows areas of necrosis, regeneration, collagen deposition (13.1%), and fat infiltration (1.5%). Conversely, the RF of control dog (panel d) appears more homogenous and with less collagen (3.2%) and fat infiltration (0.5%).

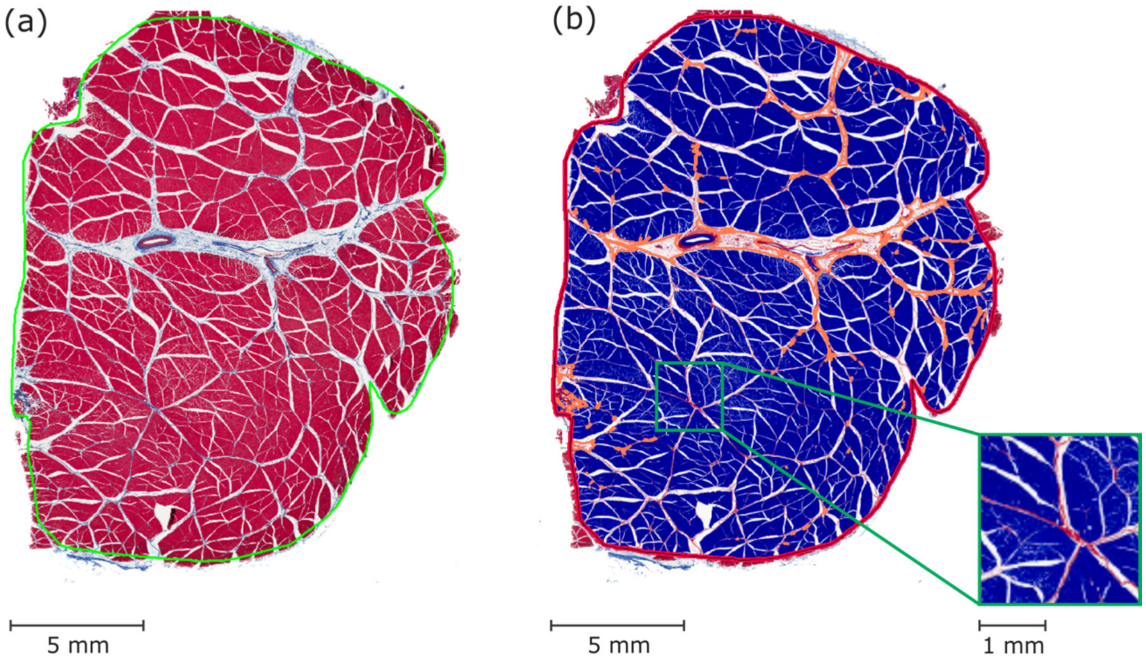

Figure 11.1: (a) Masson's trichrome stain in muscle section from a control dog at 12 months; muscle tissue is stained red and collagen blue. A hand drawn region of interest selecting the boundary for analysis is shown in green.

(b) Histological analysis was performed as the following:

1) The image was threshholded based on color to classify tissue as muscle or fat. Tissue identified as muscle is shown in blue and tissue identified as collagen is shown in red.
2) Fat was identified based on morphology and regions determined to be fat were hand-delineated, shown in orange.
3) The total area of the section was equal to the sum of the areas identified as muscle, collagen, and fat.
4) The calculations of collagen percent and fat percent for the tissue section were calculated as:

$$Collagen\ percent = \frac{Area_{collagen}}{Area_{total}} = \frac{Area_{collagen}}{Area_{muscle} + Area_{collagen} + Area_{fat}}$$

$$Fat\ percent = \frac{Area_{fat}}{Area_{total}} = \frac{Area_{fat}}{Area_{muscle} + Area_{collagen} + Area_{fat}}$$

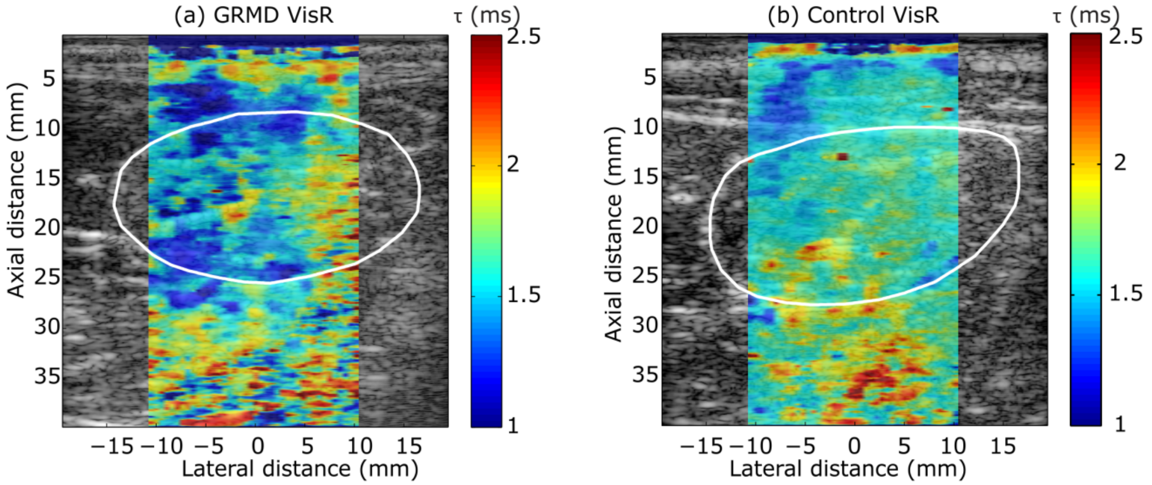

(c) GRMD Histology

(d) Control Histology

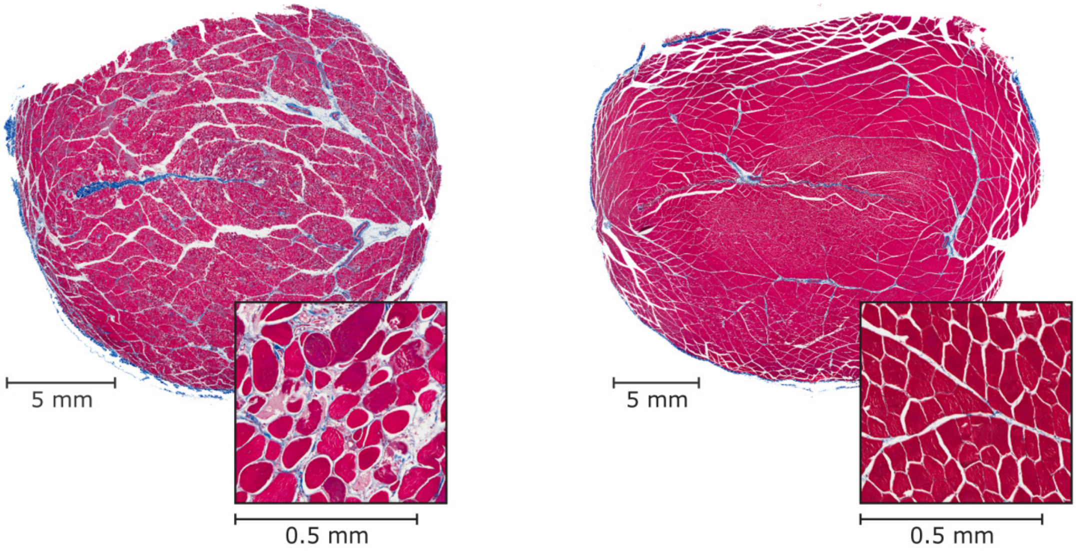

Figure 11.2: VisR τ images in the right rectus femoris (RF) muscles of (a) GRMD and (b) control littermate at 12 month of age, and corresponding histology from the (c) GRMD and the (d) control RF muscle. VisR imaging was performed in the plane transverse to muscle fibers and the white line indicates the RF muscle boundary. Standard deviation (SD) of τ was higher in the GRMD (0.430 ms) relative to the control RF (0.245 ms) indicating a higher degree of heterogeneity in τ values. Histologically, collagen and fat deposition was higher in the GRMD RF (13.1 vs .32% and 1.5 vs 0.5% respectively) compared to the control RF.

11.3.1 Cross-Sectional Study

Figure 11.3 reports τ SD measured in the VL muscles of the cross-sectional study. Measurements in the control VL muscle are shown as blue squares and the GRMD VL muscles are red circles. SD of τ was consistently larger in the GRMD versus the control VL at each age group. Averaged across age, SD of τ showed significant group differences between control and GRMD VL muscles (p=0.001).

The histological analysis and MRI results in the VL muscles are shown in Figure 11.4. At each age, GRMD dogs were shown to exhibit a higher percent of collagen (panel) in VL muscle biopsies than their age matched controls. VL muscle biopsies also showed a low percentage of fat (panel b). MRI T2 values in the VL (panel c) were generally higher and more heterogeneous, as measured by the RP (panel d), in the GRMD dogs relative to the age matched controls. Because fat percentages were generally low, the increased T2 values in the GRMD VL muscles are likely due to inflammation associated with necrosis.

SD of τ measurements in the CS muscle is shown in Figure 11.5. With the exception of a 60 month control which fell between the two GRMD measurements, τ SD was larger in GRMD versus the control CS at each time point. The difference between control and GRMD averaged across time was significant (p=0.001).

Figure 11.5 shows the histological analysis and MRI results in the CS muscles. GRMD dogs consistently exhibited a higher percentage of collagen (panel a) in CS muscle biopsies than their age matched controls. In the majority of dogs, less than 7% of the tissue was identified as fat (panel b), however, 12% fat was measured in one 24 month control CS biopsy. MRI results showed higher T2 (panel c) in the 3-6 month old GRMD relative to the control CS; in dogs older than 6 months T2 values were not correlated with phenotype. Likewise, MRI heterogeneity (panel d) in the CS did not exhibit a trend between GRMD and control.

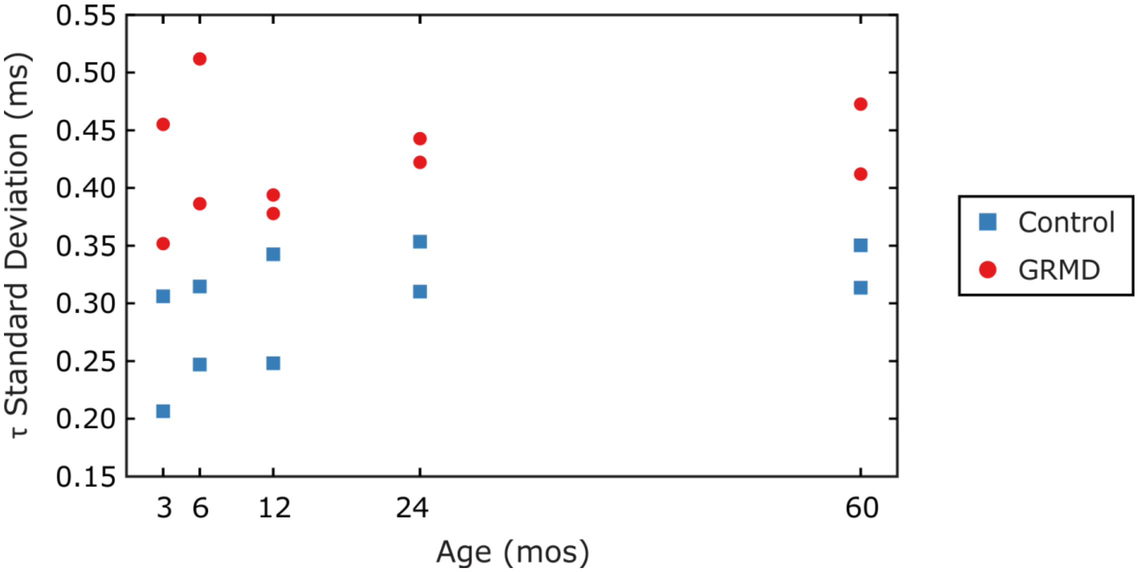

Figure 11.3: VisR imaging results in the cross-sectional VL muscles. Scatter plot illustrating the standard deviation (SD) of τ estimates versus the age of the dog at the time of imaging. Control VL muscles are indicated by blue squares and GRMD by red circles. SD of τ was larger in the GRMD compared to control VL in each age group. Averaged across age groups, SD of τ was significantly larger (p=0.001, Wilcoxon two-sample test) in the GRMD (0.423 ± 0.049 ms) relative to the control (0.299 ± 0.048 ms) VL muscle.

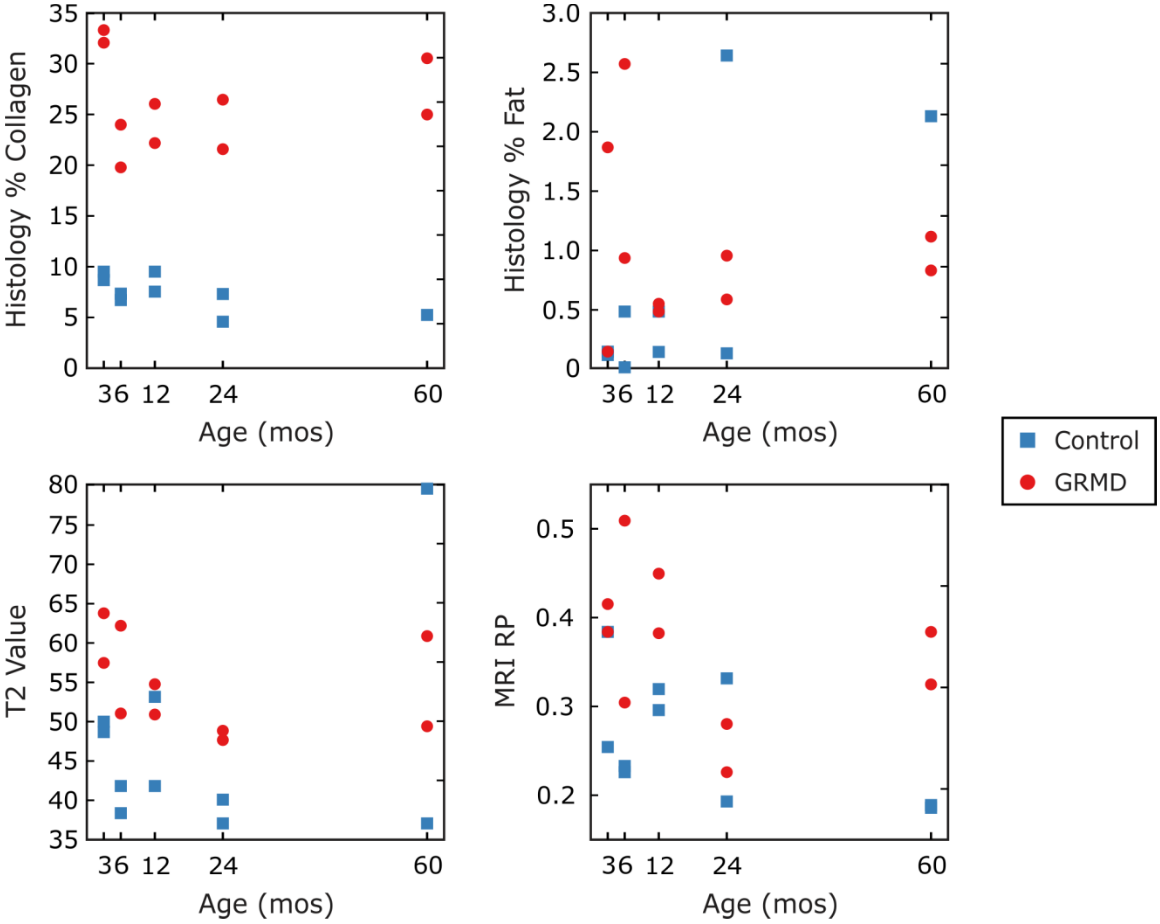

Figure 11.4: Histology and MRI results in the cross-sectional VL muscles. Control VL muscles are indicated by blue squares and GRMD by red circles. The percentage of the biopsy samples that stained for collagen (panel a) was high in the GRMD relative to the control VL muscles at all ages. Averaged across age groups, percentage of collagen by histology was 26.13% ± 4.63 and 7.61% ± 5.39 in the GRMD and control VL respectively ($p<0.001$, Wilcoxon two-sample test). No significant differences ($p=0.24$) in fat percentage (panel b) was measured between the control (0.93% ± 1.14) and GRMD groups (1.01% ± 0.72). T2-values assessed with MRI (panel c) were higher in the GRMD relative to control VL at 3, 6, and 24 months indicating increased fat/water signal. Averaged across time, T2 values were significantly higher ($p=0.01$) in the GRMD (53.82 ± 6.54) than in the control (45.17 ± 12.94). MRI run percentage (RP) (panel d), were also significantly higher ($p=0.007$) in the GRMD (0.366 ± 0.084) versus control VL (0.256 ± 0.065) averaged across time.

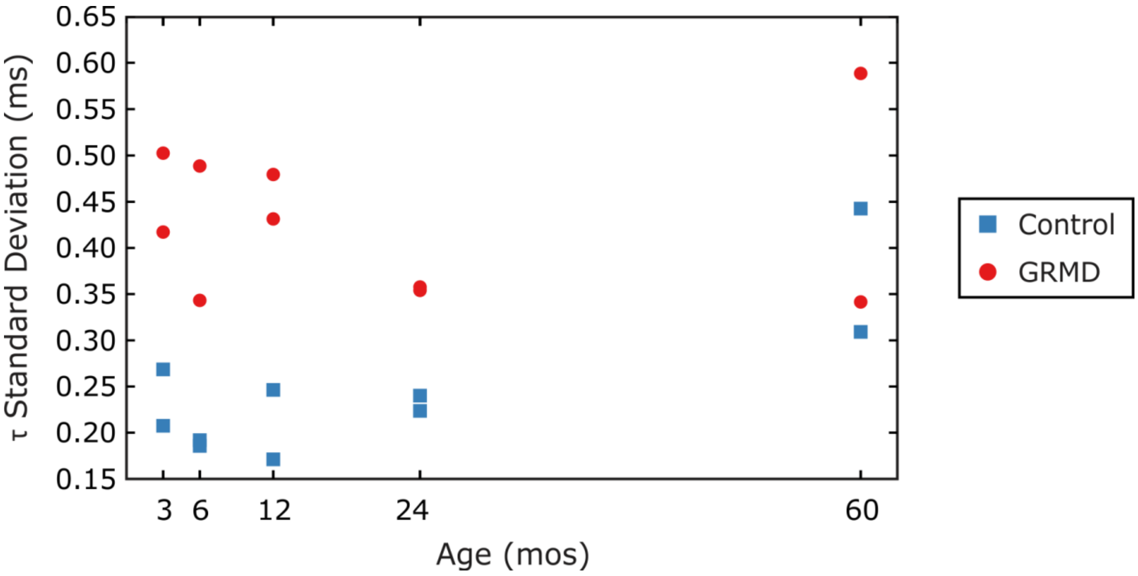

Figure 11.5: VisR imaging results in the cross-sectional CS muscles. Scatter plot illustrating the standard deviation (SD) of τ estimates versus the age of the dog at the time of imaging. Blue squares indicate control CS muscles and red circles indicate GRMD CS muscles. With the exception of one 60-month-old control, SD of τ was larger in the GRMD compared to control CS at each age. Averaged across age groups, SD of τ was significantly larger (p=0.001, Wilcoxon two-sample test) in the GRMD (0.432 ± 0.082 ms) relative to the control (0.249 ± 0.080 ms) CS muscle.

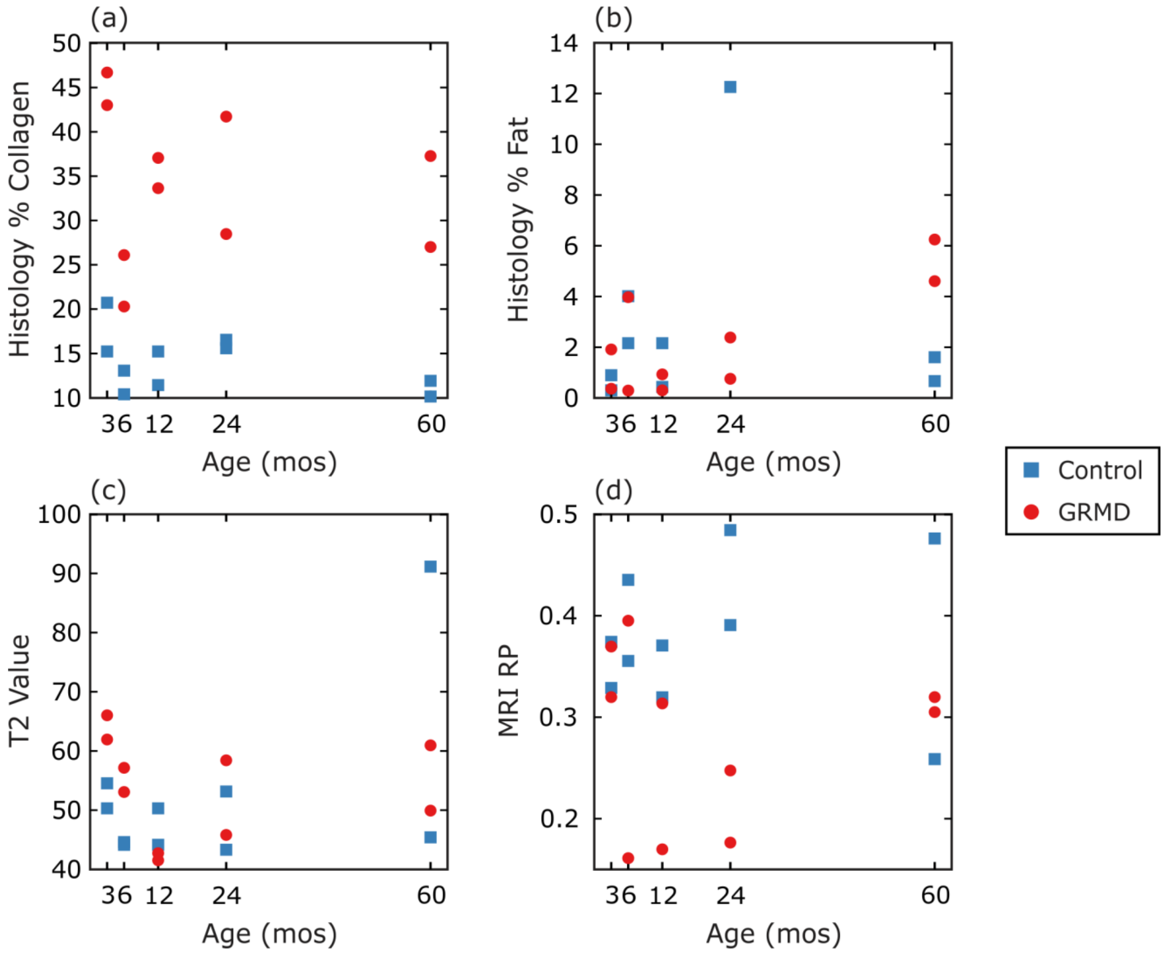

Figure 11.6: Histology and MRI results in the cross-sectional CS muscles. Control CS muscles are indicated by blue squares and GRMD by red circles. The percentage of the biopsy samples that stained for collagen (panel a) was high in the GRMD relative to the control CS muscles at all ages. Averaged across age groups, percentage of collagen by histology was 34.10% ± 8.50 and 13.59% ± 3.68 in the GRMD and control CS respectively ($p<0.001$, Wilcoxon two-sample test). Fat percentage (panel b) of histology did not appear to be corrected to phenotype ($p=.89$). 2.85% ± 4.01 fat was measured in the control CS, compared to 2.13% ± 2.15 fat in the GRMD CS. T2-values assessed with MRI (panel c) did not show significant group differences ($p=0.31$) between control CS (51.46 ± 14.63) and GRMD CS muscles (53.76 ± 8.51). Group differences were measured by MRI RP (panel d, $p=0.01$, control: 0.38 ± 0.07, GRMD: 0.28 ± 0.08).

11.3.2 Longitudinal Study

SD of τ measurements in the RF muscle through time for the four dogs included in the longitudinal study are shown in Figure 11.1. Values were higher in the two GRMDs relative to the two control RF muscles. The histology and MRI measurements in the RF are shown in Figure 11.8. Histology was not obtained for GRMD2 (purple) at 12 months. In addition, the RF biopsy sample of Control2 (green) at 6 months could not be processed. Collagen percentages (panel a) were higher in the GRMD compared to the control RF. Intramuscular fat percentages were small in all samples (panel b), but were higher in the GRMD RF samples. T2 values (panel c) in the GRMD RF were higher than in the control RF and were also more heterogeneous (panel d). The highest SD of τ measurements were measured for GRMD2 (purple) at each time point, consistent with high percentages of collagen and fat relative to the other dogs at the 6 month time point.

Figure 11.9 shows τ SD measured in the VL muscle through time. In both GRMD dogs, τ SD measurements were higher than for the control VLs. Histological and MRI results in the VL are shown in Figure 11.10. GRMD1 (red) exhibited the highest percentages of collagen (panel a) and fat (panel b) at both time points. T2 values (panel c) were also high in GRMD1 (red) at both time points, relative to the other three dogs. Heterogeneity (panel d) of the T2 values was largest in GRMD1 (red) at 6 months and in GRMD2 (purple) at 12 months. Larger SD of τ in the VL of GRMD1 (red) at 6 mos is consistent with higher percentages of collagen and fat, higher T2 values (suggesting inflammation associated with necrosis), and higher RP values in GRMD1 at 6 months. At 12 months SD of τ was higher in GRMD2 than GRMD1, and the same was true of RP.

VisR imaging results in the CS muscle through time is illustrated in Figure 11.11. SD of estimated τ was highest in the two control CS muscles at 4.5 months. After 4.5 months τ SD was highest the two GRMD CS muscles. Figure 11.12 shows the histological analysis and MRI results in the CS muscles. GRMD CS muscles exhibited a higher percent of collagen (panel a) and higher T2 values (panel c) relative to the control CS muscle. The largest fat percentage (panel b) was seen in Control1 (blue), closely followed by GRMD1 (red). Control1 (blue) also exhibited the highest heterogeneity of MRI signal (panel d). SD of τ in the CS was highest in GRMD1 at 6 and 12 months, consistent with collagen and T2 measurements.

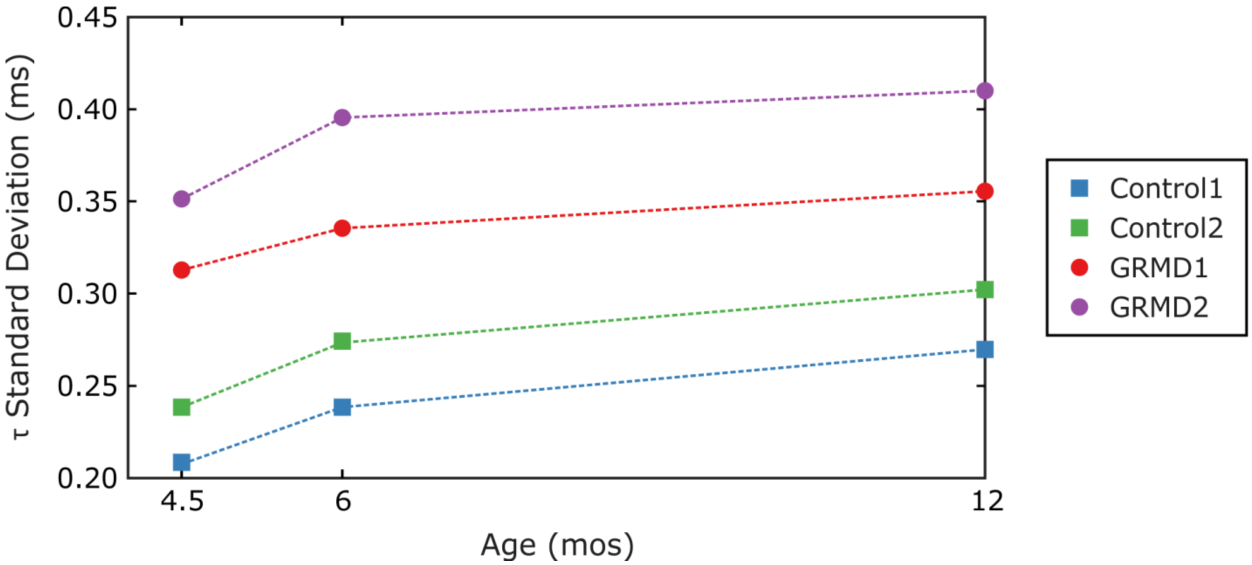

Figure 11.7: VisR imaging results in the longitudinal RF muscles. Plot shows standard deviation (SD) of τ estimates versus dog age at the time of imaging. Control RF muscles are indicated by squares and GRMD by circles, individual dog results are indicated by color. SD of τ was larger in the GRMD compared to control RF at each point in time.

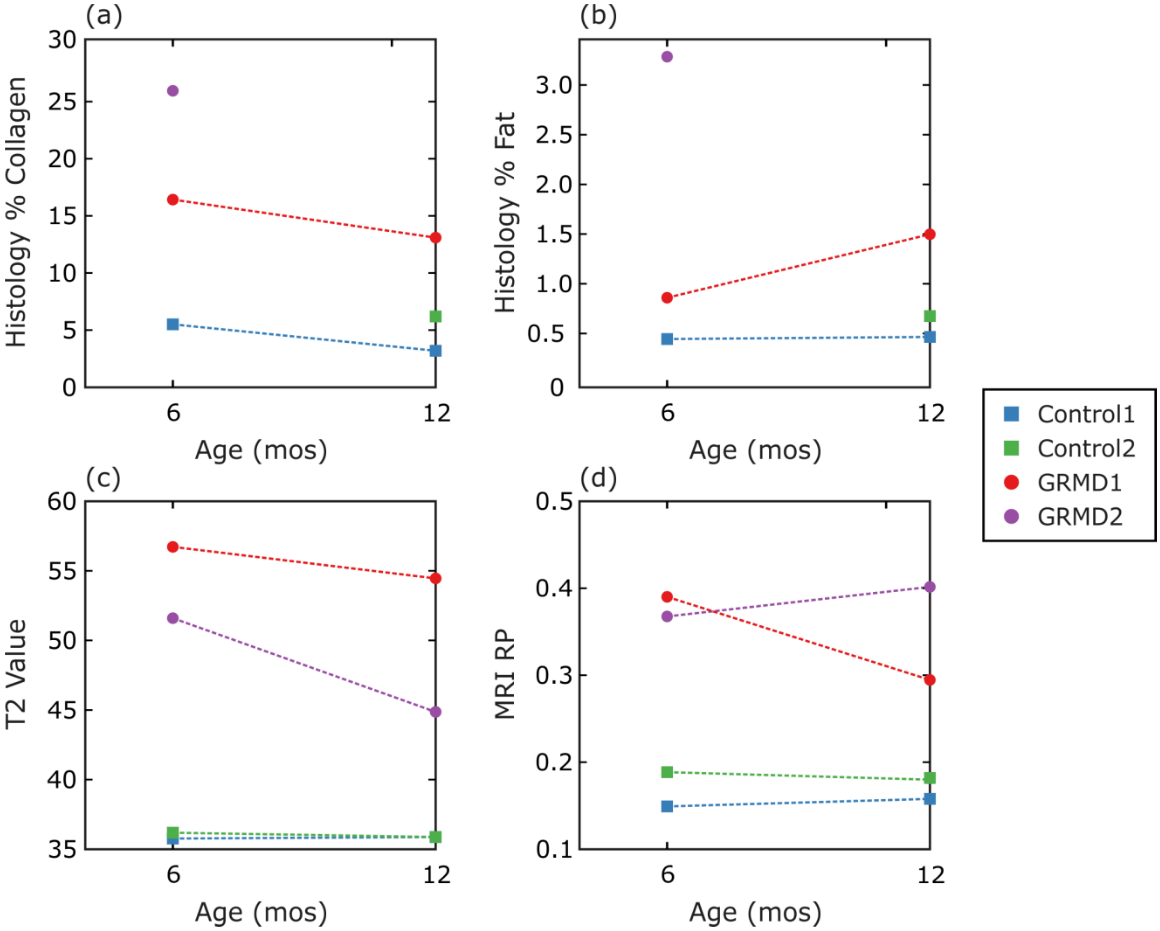

Figure 11.8: Histology and MRI results in the longitudinal RF muscles at 6 and 12 months of age. Plots show percent of collagen (a) and fat (b) from histology; and T2 value (c) and RP (d) from MRI. Available histology showed higher collagen and fat percentages in the two GRMD dogs at both time points. T2 values and RP were also larger in the two GRMD dogs at both times.

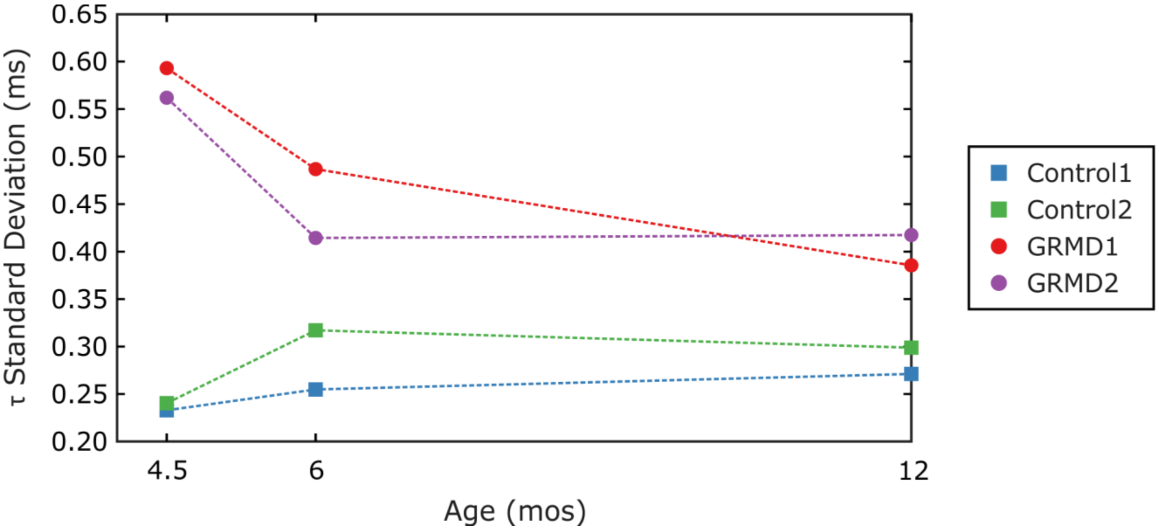

Figure 11.9: VisR imaging results in the longitudinal VL muscles. Plot shows standard deviation (SD) of τ estimates versus dog age at the time of imaging. Control VL muscles are indicated by squares and GRMD by circles, individual dog results are indicated by color. SD of τ was larger in both GRMD compared to control VL at each point in time.

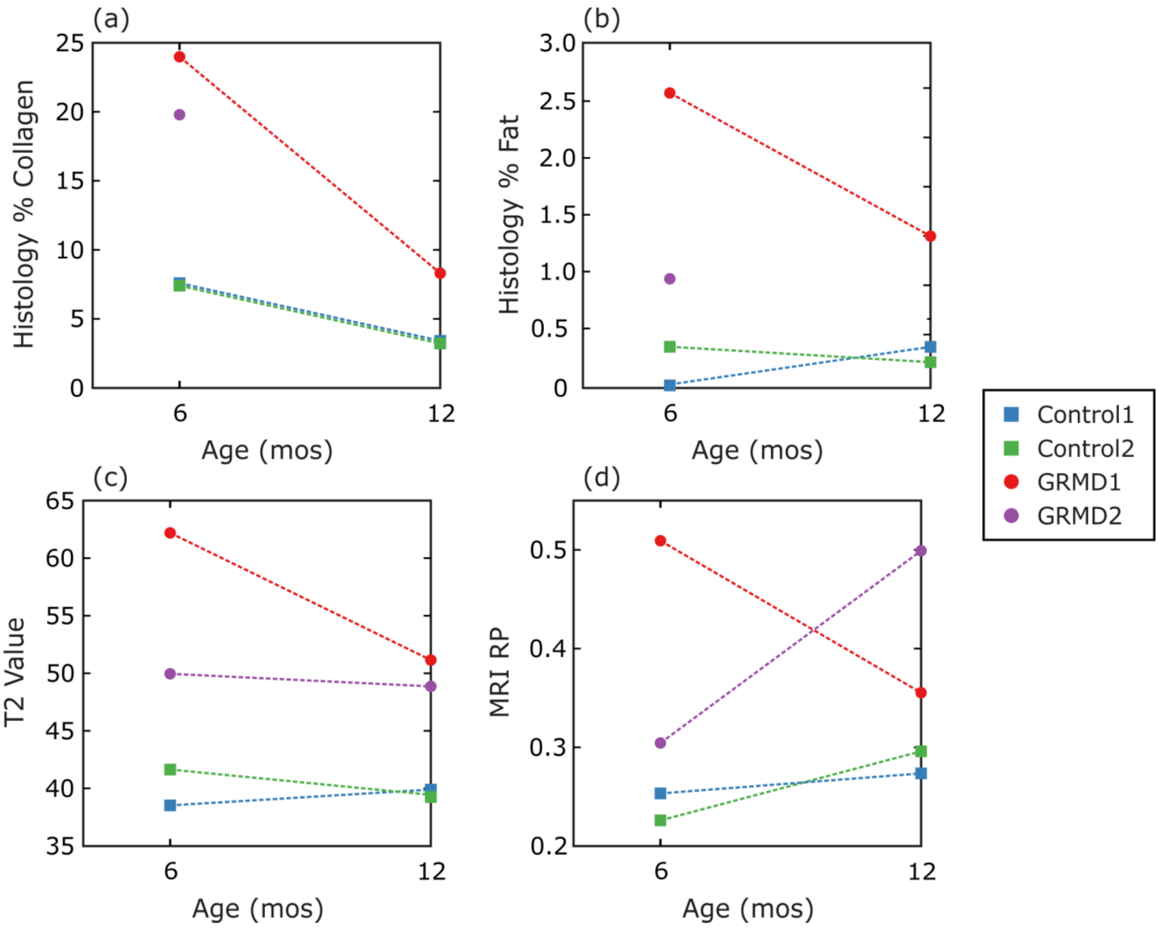

Figure 11.10: Histology and MRI results in the longitudinal VL muscles at 6 and 12 months of age. Plots show percent of collagen (panel a) and fat (panel b) from histology; and T2 value (panel c) and RP (panel d) from MRI. Histology showed higher collagen and fat percentages in the GRMD VL relative to control at both time points. The two GRMDs also exhibited higher T2 RP than the control VL muscles.

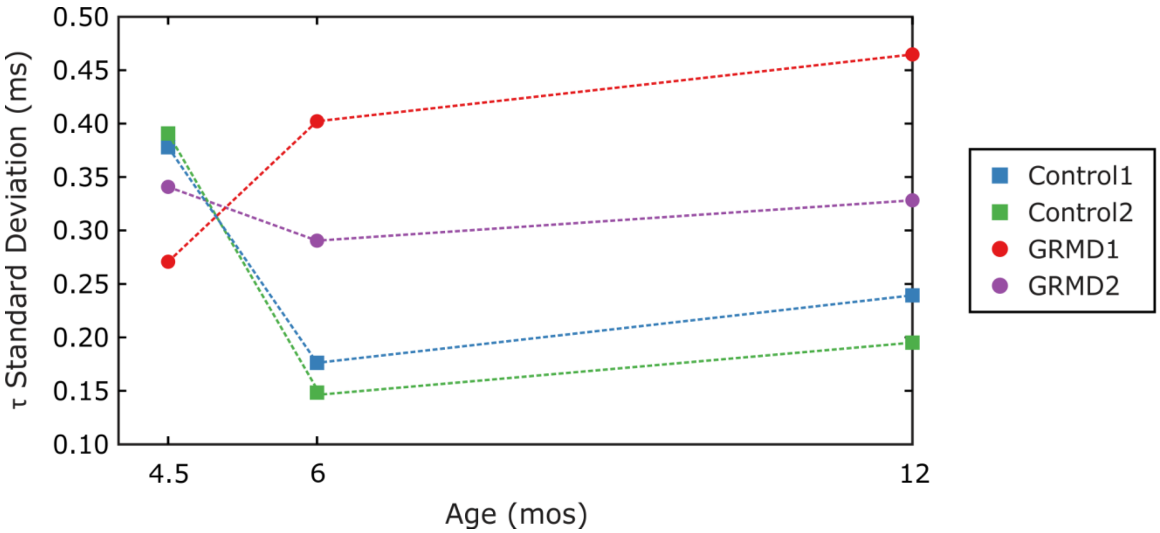

Figure 11.11: VisR imaging results in the longitudinal CS muscles. Plot shows standard deviation (SD) of τ estimates versus dog age at the time of imaging. Control CS muscles are indicated by squares and GRMD by circles, individual dog results are indicated by color. SD of τ was larger in the GRMD compared to control CS at each point in time at 6 and 12 months, but smaller in the 4.5 month time point.

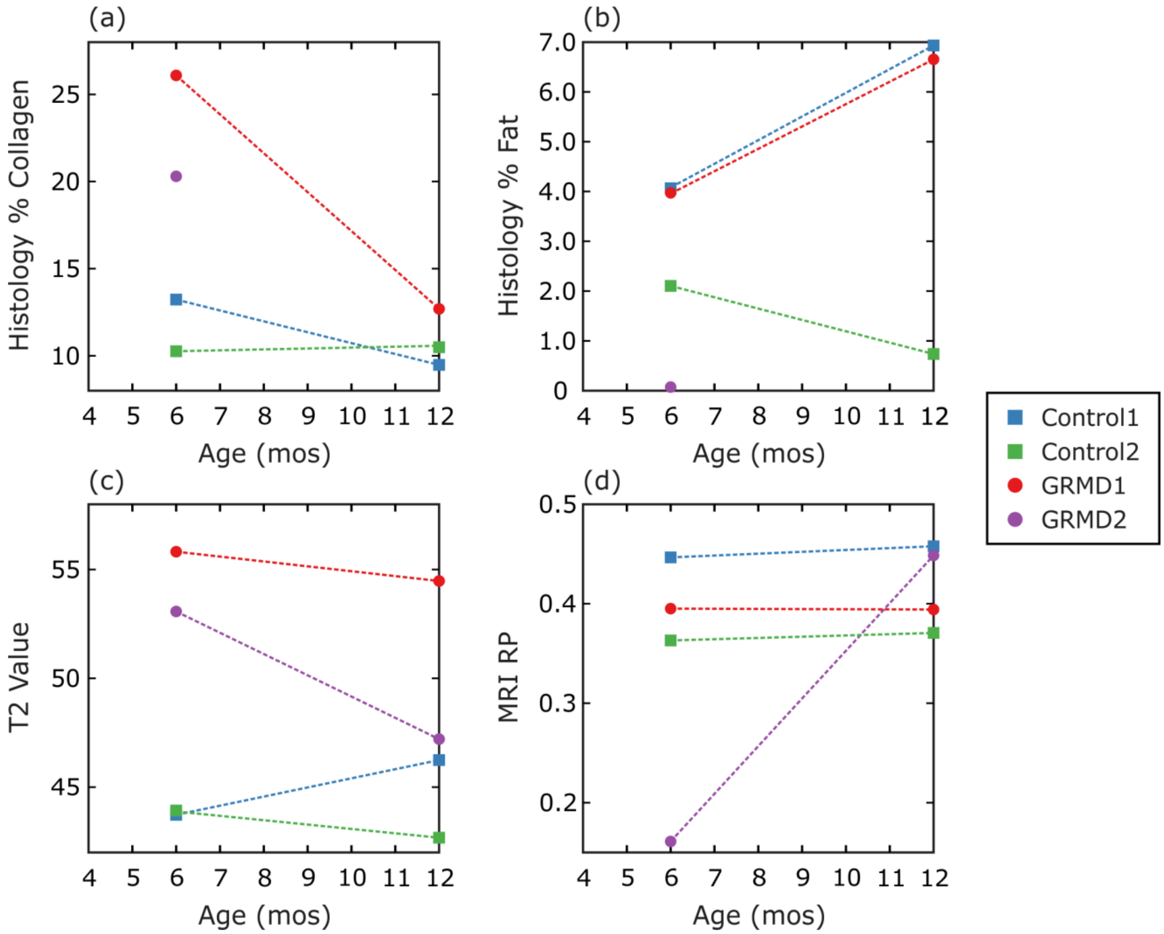

Figure 11.12: Histology and MRI results in the longitudinal CS muscles at 6 and 12 months of age. Plots show percent of collagen (panel a) and fat (panel b) from histology; and T2 value (panel c) and RP (panel d) from MRI. Collagen percentage and T2 values were high in both GRMD CS muscles relative to the control CS. Fat percentage and RP, however, were high in the Control1 CS relative to the other 3 CS muscles.

11.4 Discussion

Dystrophin-deficient muscles express variable pathologic changes, presumably due to their function over the course of life. Flexor muscles, such as the CS, tend to have earlier changes, perhaps due to their role in crawling, [67] while extensor muscles, including the RF, demonstrate somewhat delayed changes associated with eccentric contractions during weight bearing.[162] In particular, the CS muscle has been shown to undergo hypertrophy, whereas the quadriceps (including the RF and VL) atrophies.[59] CS enlargement initially occurs due to an increase in muscle (true hypertrophy) followed by connective tissue and fat (pseudohypertrophy). We expect that necrosis could lead to decreased tissue stiffness and increased τ, while collagen deposition will be associated with increased tissue stiffness and decreased τ. Because the pathologic changes of DMD and GRMD occur as multifocal areas of small group muscle fiber necrosis and regeneration,[169] these compositional changes should increase the SD of the estimates of τ made within a muscle. Furthermore, we predict that an increase in contractile tissue and disordered muscle regeneration in true hypertrophy will result in higher variations in estimated τ values.

Our expectations for the impact of dystrophic changes on the SD of τ are generally realized in these initial results. In the cross-sectional study, with the exception of one 60 month old control CS, SD of τ was larger in all GRMD VL and CS muscles relative to the age matched controls; this was consistent with higher percentages of collagen measured by histology.

In the longitudinal study, SD of τ was high in the GRMD RF and VL relative to the control muscles for all time points. In the CS, SD of τ was higher in the control CS than the GRMD at 4.5 months. After 4.5 months, SD of τ was high in the GRMD CS relative to control. While we would not expect SD of τ to be larger in the control muscle than in the GRMD muscle, the difference between the two groups is small compared to the difference between the groups at 6 and 12 months, and we appreciate that given more samples it may not be significant.

A potential confounding factor in this analysis is the error in τ estimates as discussed in Chapter 8 and 9. Because we are not accounting or correcting for error in τ due to misrepresenting the physical excitation force experienced by the tissue, we do not expect τ measurements to represent the true τ of the tissue. In addition, the effects of non-modeled force propagation will introduce error into τ measurements over axial depth. On average the muscles imaged in this chapter spanned 11.95 ± 4.35 mm. According to Figure 9.3, an axial window of 12 mm will result in 0.047 ± 0.015 ms of deviation. Because all measured standard deviations of τ were greater than 0.15 ms, we believe that the observed variations in τ were due to compositional variations rather than an effect of unmitigated error in τ measurements.

In this current analysis, only VisR images acquired at the midplane of muscle were considered, correlating to the approximate location of the biopsy site. VisR images were also acquired approximately one- and three-quarters distance between the hip and knee; including these images will provide future analyses with more data points on which to draw conclusions. Also, data collection is ongoing. Additional longitudinal cohorts will allow for a more thorough discussion of disease progression in GRMD. Furthermore, the SD statistic used in this chapter is based only the absolute values of τ within the muscle; textural analysis techniques, such as those employed in the MRI processing, take into account both the value and spatial distribution of measurements. Using these techniques, it may be possible to improve the discrimination between control and GRMD dogs.

11.5 Conclusion

In this chapter VisR was demonstrated for delineating dystrophic muscle degeneration. These preliminary results showed more variation in VisR τ estimates in dystrophic versus control VL and CS muscles, consistent with inflammation, fibrosis, and fat deposition. VisR results were corroborated by MRI and histological processing and substantiate further investigation of VisR in dystrophic muscles and other viscoelastic tissue imaging applications. In Chapter 12, VisR is demonstrated clinically in boys with DMD.

CHAPTER 12

VisR Ultrasound Assessment of Viscoelastic Properties in Human Duchenne Muscular Dystrophy, *In Vivo*

12.1 Introduction

The current outcome measurements in DMD are suboptimal. Muscle biopsy is invasive and limited by specimen size. Various functional and muscle strength assessments require subjective effort and are susceptible to rater variation. [170] Moreover, loss of muscle function in DMD occurs against the background of normal childhood growth and development, this may manifest as an improvement in physical ability despite progressive muscle impairment.[69]

In the previous Chapter, VisR ultrasound was applied to a preclinical dog model of muscular dystrophy; in this Chapter VisR clinical feasibility is demonstrated in two boys with DMD.

12.2 Methods

12.2.1 Subjects

This study was approved by the Institutional Review Board (IRB) at the University of North Carolina at Chapel Hill. Written informed consent was obtained from the participants' parents. VisR imaging and physical testing was performed in two subjects with a clinical diagnosis of DMD. Subject 1 was 6.2 years old at the start of the study and was imaged three times over the course of 15 months. Subject 2 was imaged once at 8 years old. Subject 2 was on corticosteroid treatment at the time of imaging, while Subject 1 had never used corticosteroids.

12.2.2 VisR Imaging

VisR images of the right sartorius (SART) and gastrocnemius (GAST) muscles were acquired *in vivo*. Imaging was performed using a Siemens Acuson Antares imaging system equipped for research purposes and a VF7-3 linear array transducer (Siemens Medical Solutions USA, Inc. Ultrasound Division). In patient 1, a 2 cm, non-attenuating, stand-off pad was placed between the transducer and skin to optimize the depth of the target muscle. ARF excitations were 300 cycles (70 μs) in duration and centered at 4.21 MHz with an F/3 focal configuration. Tracking pulses were centered at 6.15 MHz with an F/1.5 focal configuration and 11 kHz pulse repetition frequency. VisR beam sequences consisted of two reference tracking lines preceding a first ARF excitation, then 4 tracking lines followed by a second ARF excitation and 52 tracking lines. Two-dimensional imaging was achieved by administering the VisR beam sequence in 40 lateral locations evenly spaced across a 2.1 cm lateral field of view. The ensembles were collected using wiperblading, whereby successive ensemble acquisitions alternated from the left to the right side of the imaging FOV, to avoid motion interference. One spatially registered B-Mode frame was acquired immediately prior to each VisR acquisition. VisR images acquired at the midplane of muscle (medial) and halfway between midplane and the hip (proximal).

Acquired raw RF data was transferred to a computational workstation for processing and analysis. One dimensional cross-correlation was applied to the acquired RF data to measure induced axial displacements, and the data was processed with a linear filter to reject physiologic motion. Parametric images of τ were rendered from the acquired VisR data. Muscles were hand delineated in B-Mode images, and the delineations were applied to the corresponding matched VisR images.

12.2.3 Physical Testing

Following ViSR imaging, the subjects underwent quantitative muscle testing (QMT) , the 6-minute walk test (6MWT), and timed function tests (TFT) (see Section 3.1). QMT was perfomed using a PowerTrack II Commander hand-held dynamometer (JTech Medical Industries, Salt Lake City, UT) according to the standardized positions listed in Table 11.1, and was averaged across two repeated trials. TFTs included time to stand (5 times sit to stand) and time to walk 30-feet time.[75,171,172]

Table 12.1: Standardized Patient Positioning for QMT

Muscle/Muscle groups	Standardized Position
RF	Sitting with knee at 90° flexion, HHD at distal lower leg
Hip flexors	Supine with hip/knee at 90° flexion, HHD proximal to knee
Hip abductors	Supine with hip neutral, leg stays on table, HHD proximal to knee
GAST	Supine with ankle at neutral dorsiflexion, HHD at medial head

12.3 Results

12.3.1 VisR Imaging

Figure 12.1 shows the parametric VisR τ images acquired in the right SART muscles of Subject 1 at (a) 6.2 years of age and (b) 15 months later when the boy was 7.4 years old. Images were acquired with the transducer perpendicular to the muscle fibers, in the proximal imaging plane. VisR τ values ranged from 1.399 ± 0.539 ms and 1.674 ± 0.487 ms at 6.2 and 7.4 years, respectively. Median τ was 1.3203 ms at 6.2 years and 1.6412 ms at 7.4 years.

VisR τ images in the GAST muscle of Subject 1 at 6.2 years of age at shown in Figure 12.2(a). VisR τ values ranged from 1.033 ± 0.340 ms with a median of 1.0170 ms. In Figure

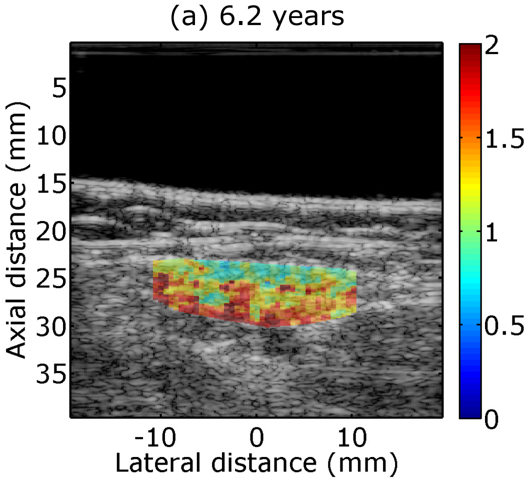

Figure 12.1: VisR τ estimates overlaid on B-Mode images in the right sartorius (SART) muscle of Subject 1 at (a) 6.2 years and (b) 7.4 years. Median τ was 1.3203 ms at 6.2 years and 1.6412 ms at 7.4 years.

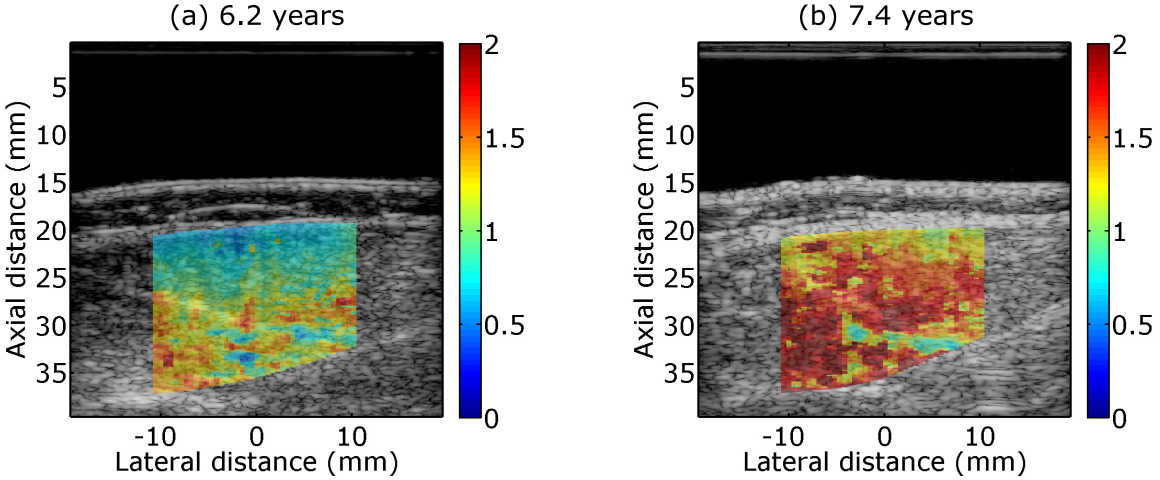

Figure 12.2: VisR τ estimates overlaid on B-Mode images in the right gastrocnemius (GAST) muscle of Subject 1 at (a) 6.2 years and (b) 7.4 years. Median τ was 1.0170 ms at 6.2 years and 1.6012 ms at 7.4 years.

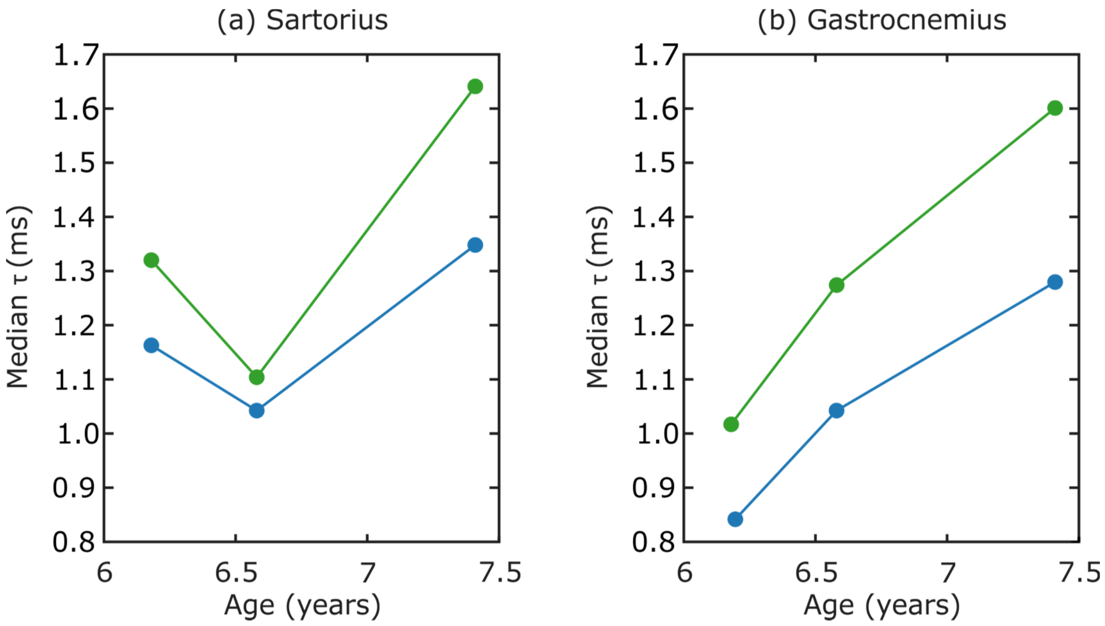

Figure 12.3: Median τ measurements in the (a) sartorius (SART) and (b) gastrocnemius (GAST) of Subject 1 over time in the proximal (green) and medial (blue) imaging planes. Estimates of τ in the SART increased from the first to third time point by 19.5% and 13.7% in the proximal and medial imaging planes respectively. Estimates of τ in the GAST increased from the first to third time point by 36.5% in the proximal and 35.9% in the medial imaging planes.

12.2(b), Subject 1 was 7.4 years old with τ values ranging from 1.629 ± 0.471 ms, with a median of 1.6012 ms. Median τ values are depicted in Figure 12.3 for the (a) SART and (b) GAST muscles at the three imaging time points. VisR imaging in the proximal plane are shown in green, and the medial plane in blue.

Figure 12.4 shows the parametric VisR τ images acquired in the right SART and GAST muscles of the Subject 2 at 8 years of age. In the SART τ ranged from 1.535 ± 0.271 ms with a median τ of 1.5432 ms. VisR τ values of 1.649 ± 0.284 ms and a median of 1.6556 ms, were measured in the GAST of Subject 2.

Figure 12.5 shows the median τ values in the (a) SART and (b) GAST muscles of Subject 1 at baseline (6.2 years) compared to Subject 2 (6.2 years). Estimates of τ in the SART of Subject 1 were 86% and 73% of those measured in Subject 2, in the proximal (green) and medial planes

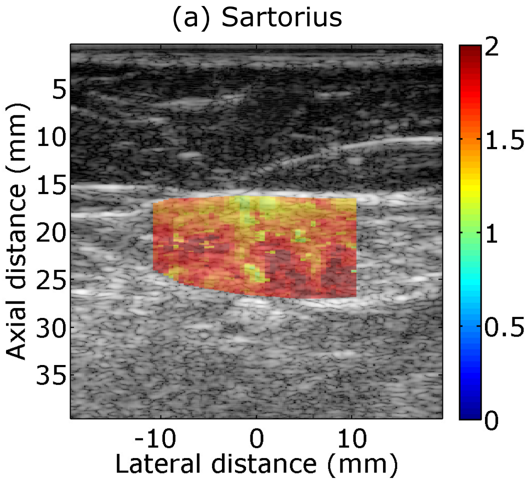

Figure 12.4: VisR τ estimates overlaid on B-Mode images in the (a) sartorius (SART) and (b) gastrocnemius (GAST) muscle of Subject 2. Median τ was 1.5432 ms in the SART and 1.6556 ms in the GAST.

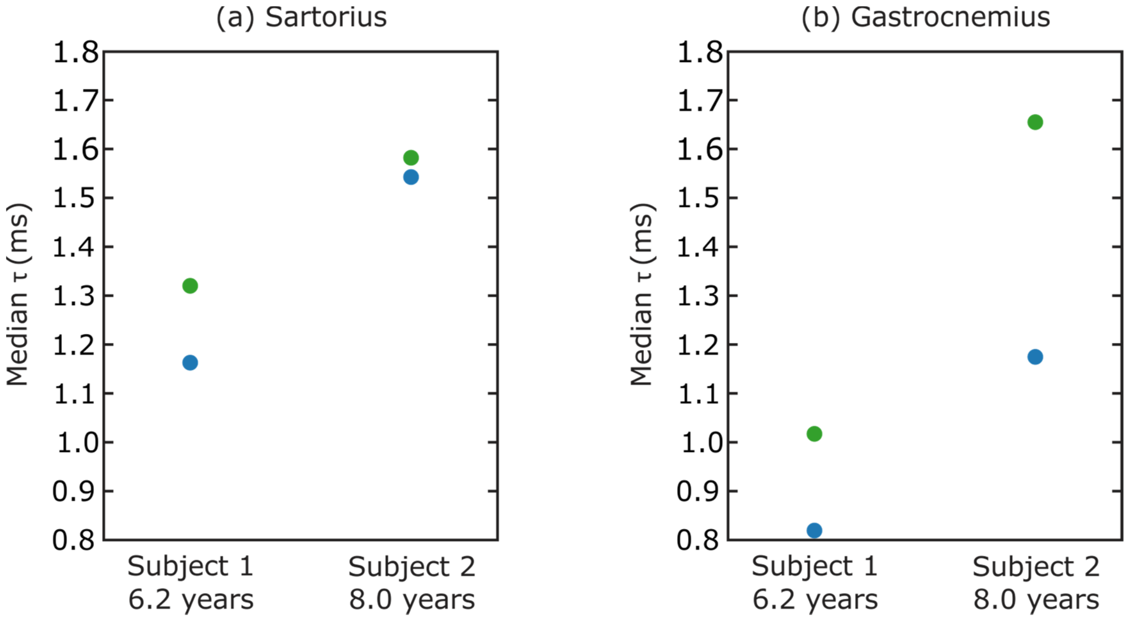

Figure 12.5: Median τ values in the (a) SART and (b) GAST muscles of Subject 1 at baseline and Subject 2. In the SART, median τ values were 1.163 and 1.3203 ms in the medial (blue) and proximal (green) imaging planes respectively for Subject 1, and 1.543 and 1.5825 ms for Subject 2. Median τ values in the GAST were 0.819 and 1.017 ms in the medial and proximal imaging planes respectively for Subject 1, and 1.175 and 1.656 ms for Subject 2.

(blue) respectively. In the GAST, τ values in Subject 1 were 61% of Subject 2 in the proximal plane (green), and 69% of Subject 2 in the medial plane.

12.3.2 Physical Testing

QMT for Subject 1 is shown in Figure 12.6 for the (a) RF, (b) hip flexors, (c) hip abductors, and (d) GAST. Of the four muscle/muscle groups, the hip flexors were the only muscle group which showed a diminished ability to produce force from baseline testing. The 6MWT and TFT results are shown in Figure 12.7. Over the course of 15 months, Subject 1 exhibited improvements in 6MWT and time to walk 30 feet. However, the time it took him to rise from a chair five times increased by 300%.

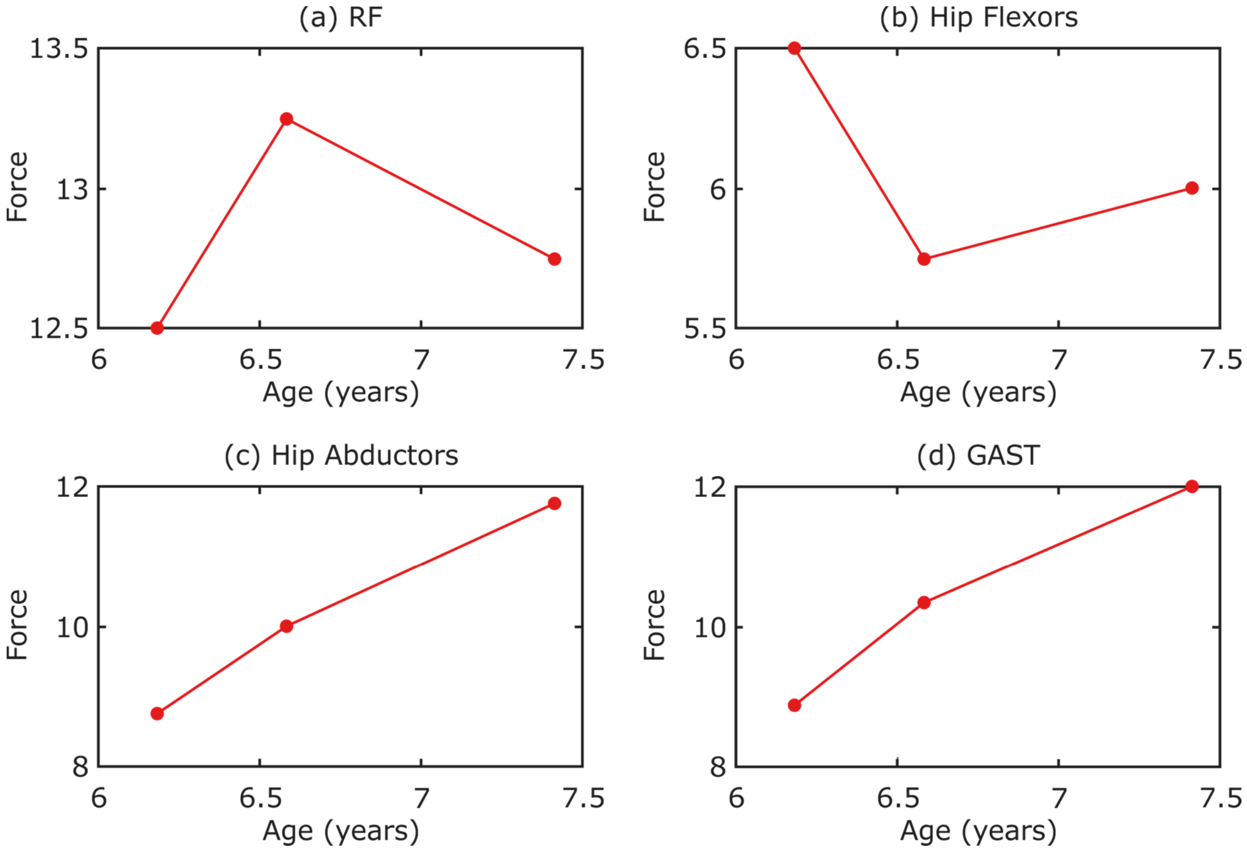

Figure 12.6: QMT testing in Subject 1 in the (a) rectus femoris (RF), (b) hip flexors, (c) hip abductors, and (d) gastrocnemius (GAST).

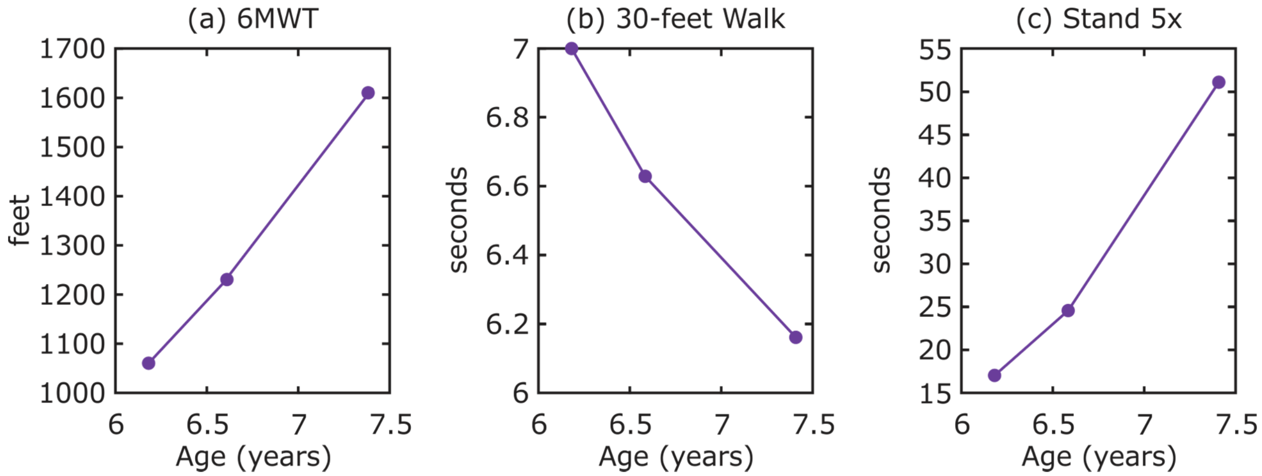

Figure 12.7: 6MWT and TFT results for Subject 1. An increase in distance in the (a) 6MWT and a decrease in the time needed to (b) walk 30-feet are both associated with increased physical abilities. However, the time Subject 1 needed to (c) rise from a chair (x5) increased from 17 seconds to 51 seconds over the course of the study.

In Figure 12.7, QMT in Subject 1 at baseline is compared to Subject 2. Subject 2, the 8-year-old boy, had higher mean force measurements in all four muscles/muscle groups than Subject 1, produced higher forces than Subject 1 in all four muscles/muscle groups. The 6MWT and TFT results for the two boys are shown in Figure 12.8. Subject 1 walked 23% further in 6 minutes and performed the 30-foot walk 24% faster than Subject 2. In addition, Subject 1 completed the sit to stand test in 17 seconds, whereas Subject 2 could not stand from a seated position without the use of his arms and was therefore unable to perform the test.

12.4 Discussion

As in GRMD, there is phenotypic variation among muscles in human DMD. The SART muscle is thought to be relatively spared,[173] while the GAST undergoes pseudohypertrophy, whereby muscle enlargement is due, at least in part, to an excess of adipose and connective tissue.[33,174] MRI studies have shown significant intramuscular fat in the GAST.[175,176]

In Subject 1, median τ value in the GAST muscle increased by 36.5% and 35.9% over the course of 15 months in the proximal and medial imaging planes respectively. This increase in τ would suggest an increase in viscosity and/or decrease in stiffness of the muscle over time, both

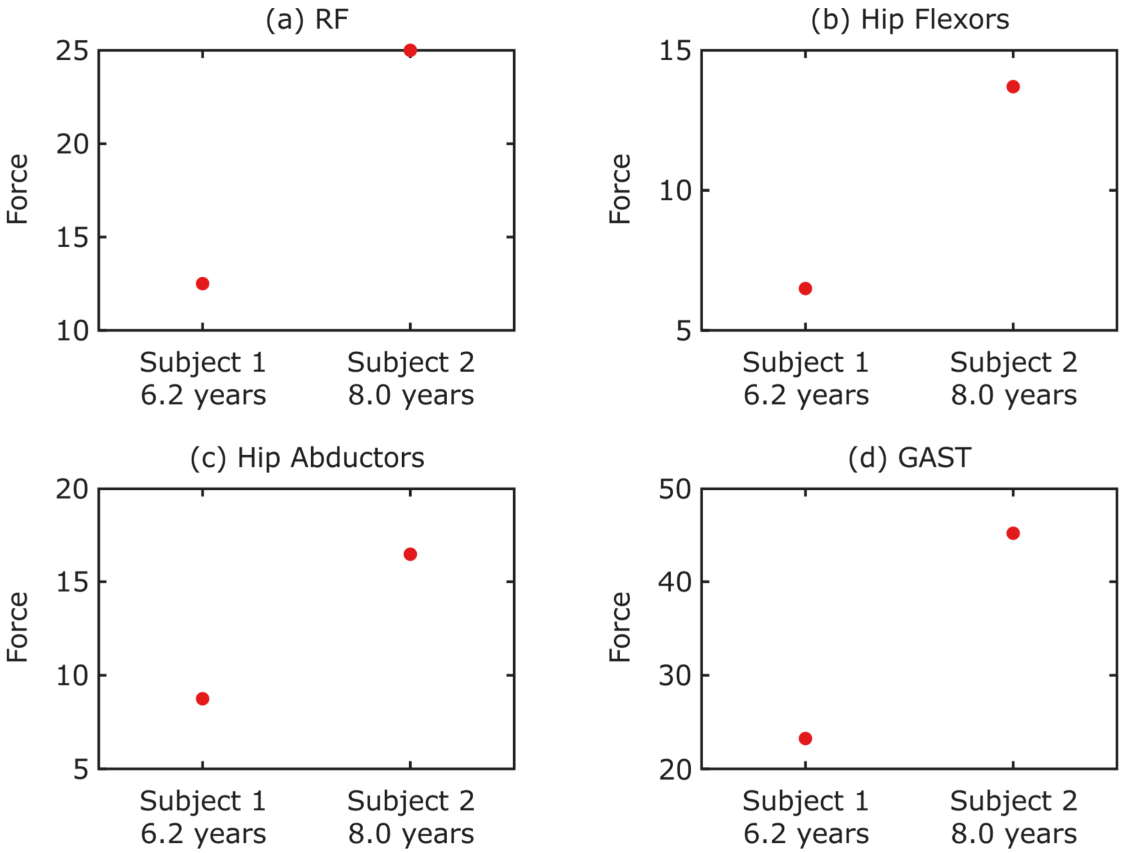

Figure 12.8: QMT testing in Subject 1 at baseline and Subject 2 in the (a) rectus femoris (RF), (b) hip flexors, (c) hip abductors, and (d) gastrocnemius (GAST).

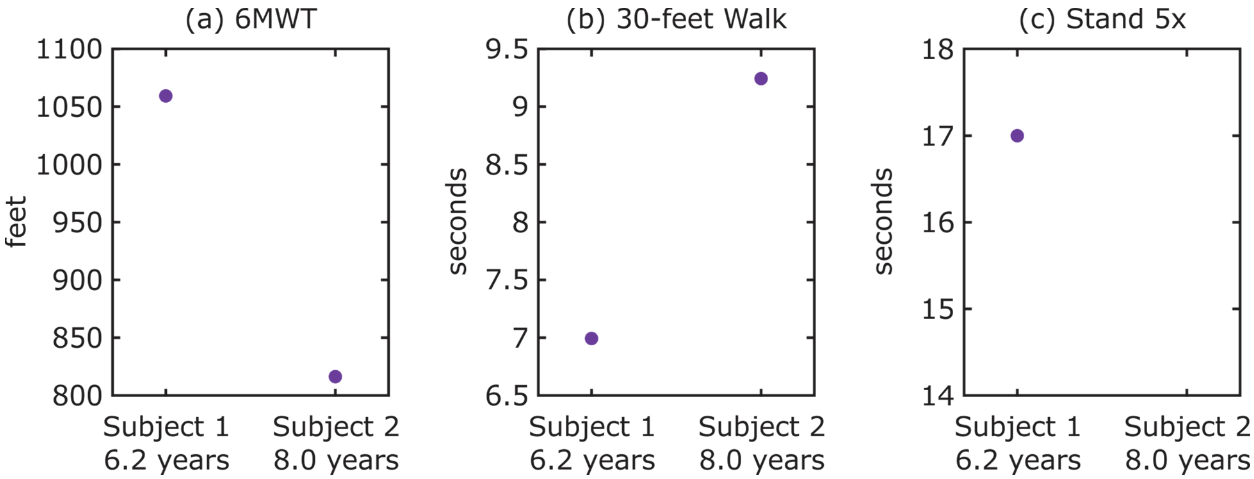

Figure 12.9: 6MWT and TFT results for Subject 1 at baseline and Subject 2. In the (a) 6MWT, Subject 1 walked 1060 feet versus 817 feet walked by Subject 2. Subject 1 performed the (b) time to walk 30-feet in 6.16 seconds versus 9.25 seconds for Patient 2. In the time to stand test (c), Subject 1 needed 17 seconds. Subject 2 was unable to rise from the chair without using the armrests to assist him, and thus he could not perform the test.

consistent with an increase in fat. Meanwhile, τ values in the SART increased by 19.5% in the proximal plane and 13.7% in the medial plane. This higher degree of change in the GAST versus the SART is consistent with the expected phenotypes of the muscles.

Despite increasing τ values suggesting compositional changes in his muscles, Subject 1 experienced improvements in QMT, 6MWT, and the time to walk 30 feet test. This is not surprising, as functional decline in motor performance, such as reduced distance walked in the 6MWT, is often not observed in DMD until after age seven due to normal growth and development.[177] Furthermore, time to rise from a chair, which is one of the first functional abilities lost in DMD boys, increased by 300% between 6.2 years of age and 7.4 years of age suggesting loss of muscle function.

Subject 2 performed slower in the TFTs and covered less distance in the 6MWT than Subject 1. These results, in conjunction with the higher τ values estimated in both of Subject 2's muscles, suggest that an increase in fatty deposition may be associated with a decline in physical performance.

12.5 Conclusion

This *in vivo* study demonstrated the feasibility of VisR imaging for delineating dystrophic muscle degeneration in two boys with DMD. Consistent with the known, distinct phenotypic response of the two muscles, our results suggested larger changes in composition of the GAST relative to the SART muscle both longitudinally and cross-sectionally. Further, a larger percentage of high τ values were associated with lower functional testing scores. These findings suggest VisR may be relevant as a novel outcome measure for diagnostics and clinical trials in DMD. Importantly, VisR measured changes in muscle composition, while degeneration was masked by growth and degeneration in physical testing.

Chapter 13

Conclusions and Future Work

13.1 Conclusions

The goal of this dissertation was to evaluate the hypothesis that Viscoelastic Response (VisR) ultrasound can noninvasively characterize the viscoelastic properties of soft tissue *in vivo*. A number of key accomplishments were made.

First, the deformation of a viscoelastic material in response to an impulsive force was modeled using FEM. From these simulations it was determined that inertial contributions are not insignificant and must be accounted for by the mechanical model. Further FEM simulations revealed, however, that using an ARF excitation to generate the force will result in error in the measurement of the relaxation time constant, τ. A correction function was generated which supports quantitative imaging of τ, but only over a narrow axial range. The effects of acoustic displacement underestimation on VisR were also demonstrated, and it was shown that by tracking displacements induced by propagating shear waves outside the region of excitation (ROE), displacement underestimation can be reduced; applying the correction function allows for quantitative assessment of τ in an acoustically tracked material. It was also shown that, using VisR, the viscous and elastic materials properties of tissues can be isolated relative to the magnitude of the ARF excitations.

Secondly, VisR was demonstrated for delineating dystrophic muscle degeneration in a dog model of Duchenne muscular dystrophy (DMD). Results showed more variation in VisR τ estimates in dystrophic versus control muscles and were corroborated by MRI and histology. A clinical feasibility study was also completed in two boys with DMD. VisR estimated τ was shown to increase with time suggesting increasing muscle degradation. Cross-sectionally, increased τ was associated with lower functional testing scores. These preclinical and clinical results, while preliminary, were consistent with previously reported MRI results[92,93,168,175,176] and suggest that VisR can be used to assess the local composition of individual dystrophic muscles. In addition, the reduced time and cost of VisR ultrasound compared to MRI, makes it a pertinent outcome measure in the evaluation of DMD.

13.2 Future Work

The results in this dissertation warrant continued development. In particular, a more accurate description of the ARF excitation that accounts for the volumetric nature of the impulse and allows for wave propagation from the surrounding medium would facilitate quantitative VisR imaging. Developing this description is complicated by the material dependence of the wave propagation, and will likely rely on *a priori* knowledge of the mechanical properties of the surrounding medium. This may be accomplished by leveraging other imaging techniques, such as shear wave velocity measurements, to provide additional information about the material. Failing to develop a better model for describing the forcing function, it may be possible to improve the error correction function. Incorporating additional parameters, such as estimated relative elasticity, into the function may provide for error correction over a larger axial distance, extending the relevance for 2D imaging.

Chapter 6 shows that by using a symmetric ARF excitation, VisR measurements can be made independent of muscle fiber orientation. However, this study was completed after the VisR data was being acquired in the dog model presented in Chapter 11. Therefore, VisR imaging was performed only with an F/1.5 focal configuration in the presented pre-clinical studies. As shown in Chapter 6, not only was τ more consistent across angles, which we anticipate will benefit longitudinal measurements, but standard deviation of τ at each angle was reduced. VisR imaging in additional longitudinal cohorts is ongoing, and is currently being performed with an F/3 focal configuration. We hypothesize that with the larger focal configuration, standard deviations in τ measurements due to fiber orientations will be reduced. This should improve the discrimination between control and GRMD dogs.

Future analysis of the preclinical dog data presented in Chapter 11 and the clinical human data presented in Chapter 12 should look at other parameters in addition to τ, such as relative elasticity and relative viscosity. We believe that when used in concert with τ, these force-dependent parameters will help achieve our goal of differentiating and identifying normal muscle, fibrotic, and fatty tissue.

Other future work involves developing real-time VisR imaging. Using custom C++ code, we have reduced the time to generate a VisR τ image to an average of 3 minutes. We believe that leveraging GPU processors and other optimizations, we can further reduce the computation time. Real-time VisR would allow sonographers and clinicians to further optimize imaging, by utilizing feedback to perfect alignment of the muscle with the imaging plane. Real-time feedback would also allow the sonographer to visualize the quality of the VisR images and determine objectively when images are corrupted due to low correlation or large motion artifacts. Currently in the clinic, acquisitions are repeated if patient motion is suspected. Knowing whether repeat acquisitions are necessary could reduce unnecessary exposure. Additionally, an adaptive scheme to automatically alter the imaging parameters during the experiment could optimize the VisR sequence for specific tissue.

Lastly, VisR imaging will benefit from 2D matrix arrays capable of focusing in both lateral and elevational dimensions. These arrays will allow for better concentration of the excitation pulses and increased focal displacements. Two-dimensional arrays would also support reduction of the tracking beam's elevational dimension relative to the pushing dimension so that displacement underestimation may be reduced. In addition, a symmetric PSF in the lateral-elevational plane could be achievable with a smaller focal configuration. This would improve mechanical resolution of VisR, while still maintaining insensitivity to muscle fiber orientation.

Although substantial work remains before it can be translated into wide clinical use, this work suggests that discrimination of muscle degeneration in DMD is possible with VisR ultrasound.

APPENDIX A

Validation of Voigt Material Model

A.1 Introduction

As described in this dissertation, Viscoelastic Response (VisR) ultrasound assesses the viscoelastic properties of tissue using two successive ARF impulses and monitoring induced displacements in the region of ARF excitation. The mass-spring-damper (MSD) model, which consists of the Voigt model connected in serial with a mass component, is used to determine the relaxation time constant for constant stress (τ) of the material. In order to simulate VisR in FEM, a Voigt model of a nonzero density material is needed. While LS- DYNA (Livermore Software Technology Corp., Livermore, CA) does not include a Voigt material model, it has implemented a material model of the Zener model. We hypothesize that through the use of the appropriate material parameters the Zener model can be used to simulate a Voigt model in compression. In this chapter, the Voigt model and the Zener model will be described, and the response of these models under creep compression will be defined. It will also demonstrate that a Voigt material can be simulated in LS-DYNA over a range of elastic and viscous properties.

A.2 Background

A.2.1 Voigt Model

The Voigt model, which is illustrated in Figure A.1, consists of a spring (with elastic constant μ_1) and damper (with coefficient of viscosity η) in parallel. The governing equation for this model is given by:

$$\sigma(t) = \mu_1 \varepsilon(t) + \eta \frac{d\varepsilon(t)}{dt} \tag{A.1}$$

where σ is the stress and ε is the strain.

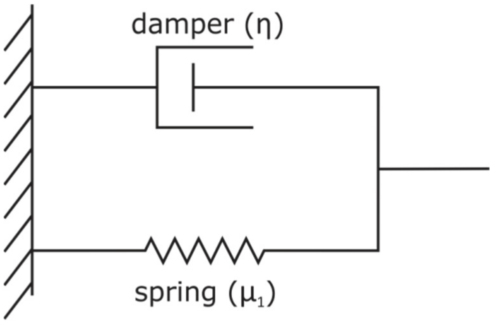

Figure A.10: A schematic of the Voigt model

When a stress of σ_0 is applied instantaneously and held constant, the Voigt model predicts an exponential behavior approaching a steady-state strain of ε_{ss} represented by the following equation:

$$\varepsilon(t) = \frac{\sigma_0}{\mu_1}\left(1 - e^{-t/(\eta/\mu_1)}\right) \tag{A.2}$$

$$\varepsilon_{ss} = \frac{\sigma_0}{\mu_1}. \tag{A.3}$$

The exponential term, ${}^{\eta}/_{\mu_1}$, is the relaxation time parameter, τ, of the material. The τ parameter is the time required for the Voigt material to deform to 63.21% (or 1-1/e) of its total deformation.

A.2.2 Zener Model

The Zener model, which is illustrated in Figure A.2, consists of the Voigt model in series with an additional spring (elastic constant μ_2). The governing equation for this model is given by:

$$(\mu_1 + \mu_2)\sigma(t) \;+\; \eta\frac{d\sigma(t)}{dt} = \mu_1\mu_2\varepsilon(t) + \eta\mu_2\frac{d\varepsilon(t)}{dt}. \tag{A.4}$$

When a stress of σ_0 is applied instantaneously and held constant, the Zener model predicts an instantaneous deformation followed by an exponential behavior approaching a steady-state

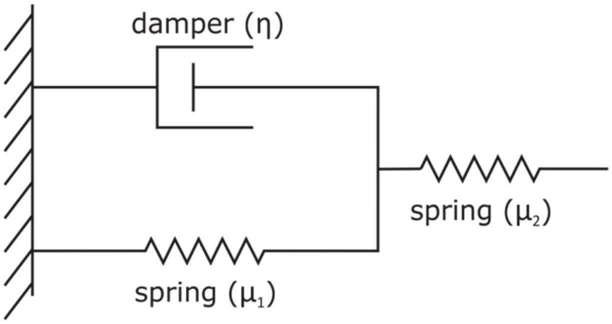

Figure A.2: A schematic of the Zener model

strain of ε_{ss}, and is represented by the following equation:

$$\varepsilon(t) = \frac{\sigma_0}{\mu_2} + \frac{\sigma_0}{\mu_1}\left(1 - e^{-t/\tau}\right) \tag{A.5}$$

$$\varepsilon(0) = \frac{\sigma_0}{\mu_2} \tag{A.6}$$

$$\varepsilon_{ss} = \frac{\sigma_0}{\mu_1} + \frac{\sigma_0}{\mu_2} \tag{A.7}$$

where $\tau = {}^{\eta}/_{\mu_1}$. It can be shown by evaluating Equation (A.5), that if μ_2 approaches infinity, $\varepsilon(t)$ reduces to the Voigt creep compliance (Equation A.2):

$$\lim_{\mu_2 \to \infty} \frac{\sigma_0}{\mu_2} + \frac{\sigma_0}{\mu_1}\left(1 - e^{-t/\tau}\right) = \frac{\sigma_0}{\mu_1}\left(1 - e^{-t/\tau}\right). \tag{A.8}$$

A.3 Methods

Compression Test

LS-PREPOST (Livermore Software Technology Corp., Livermore, CA) was used to generate a three-dimensional, rectangular, solid mesh consisting of 125 nodes and 64 elements. The spatial extent of the mesh was 0.4 mm (x), by 0.4 mm (y), by 0.2 mm (z). The bottom surface of the mesh was fully constrained. A stress of 0.1 Pa was applied to top surface of the mesh at time t=0 and held constant for 10 ms. Displacement of the top surface was measured (Δz) and used to calculate strain through time as:

$$\varepsilon(t) = \frac{\Delta z}{z} = \frac{\Delta z}{0.2} \tag{A.8}$$

where z is the original height of the mesh and was equal to 0.2 mm.

After 10 ms, the material was assumed to have reached steady-state strain (ε_{ss}), which was used to validate the elasticity of the simulated material as:

$$\mu_1 = \frac{\sigma_0}{\varepsilon_{ss}} = \frac{0.1\ \text{Pa}}{\varepsilon_{ss}} \tag{A.9}$$

The τ of the material was validated as the time at which strain reached 63.21% of ε_{ss}, as illustrated in Figure A.3.

Material Properties

In LS-DYNA, the MAT_KELVIN-MAXWELL_VISCOELASTIC material describes a Zener model with elasticities of μ_1 and μ_2, and viscosity η. In order to determine the value of μ_2 necessary for the model to behave as a Voigt material, compression tests were performed on a material with a μ_1 of 10 kPa, η of 1 Pa·s, and μ_2 ranging from μ_1 to $1000 \times \mu_1$. Percent error in τ and computational time were measured for each value of μ_2, and the μ_2 where error in τ fell below 1% was considered sufficiently large for modeling a Voigt material. Compression tests

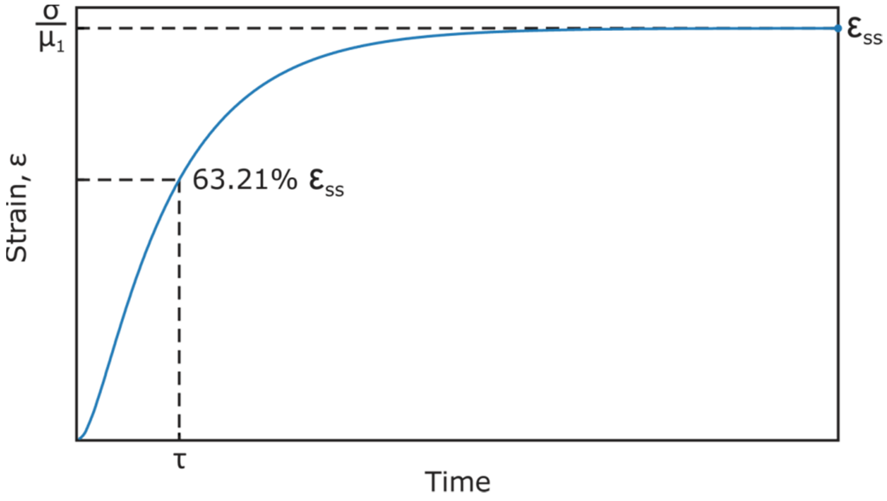

Figure A.3: Diagram showing strain versus time curve of a Voigt material under constant stress. Steady-state strain (ε_{ss}) is measured as the strain at t=10 ms and τ is measured as the time needed for the strain to reach 63.21% ε_{ss}.

were then performed on materials with elasticities of 5 and 100 kPa and viscosities of 1 and 10 Pa·s in order to validate the range of materials utilized throughout this dissertation. A density of 1.0 g/cm^3 and a Poisson's ratio of 0.499 were used for all simulations.

A.4 Results

Figure A.4 shows the results of compression simulations in a material with μ_1 of 10 kPa and an η of 1 Pa·s, with the ratio of ${}^{\mu_2}/_{\mu_1}$ ranging from 1 to 1000. Panel (a) shows that as μ_2 is increased the percent error in measured τ was reduced, with error falling below 1% when $\mu_2 = 200 \times \mu_1$. Computational time for each simulated value of μ_2 is shown in panel (b).

Strain curves for materials under constant stress are shown in Figure A.5 for materials with $\mu_2 = 200 \times \mu_1$ and (a) μ_1 of 5 kPa and η of 1 Pa·s, (b) μ_1 of 5 kPa and η of 10 Pa·s, (c) μ_1 of 100 kPa and η of 1 Pa·s, and (d) μ_1 of 100 kPa and η of 10 Pa·s. Elasticity and τ of the simulated materials were measured from the observed strain profiles and are summarized in Table A.1. In

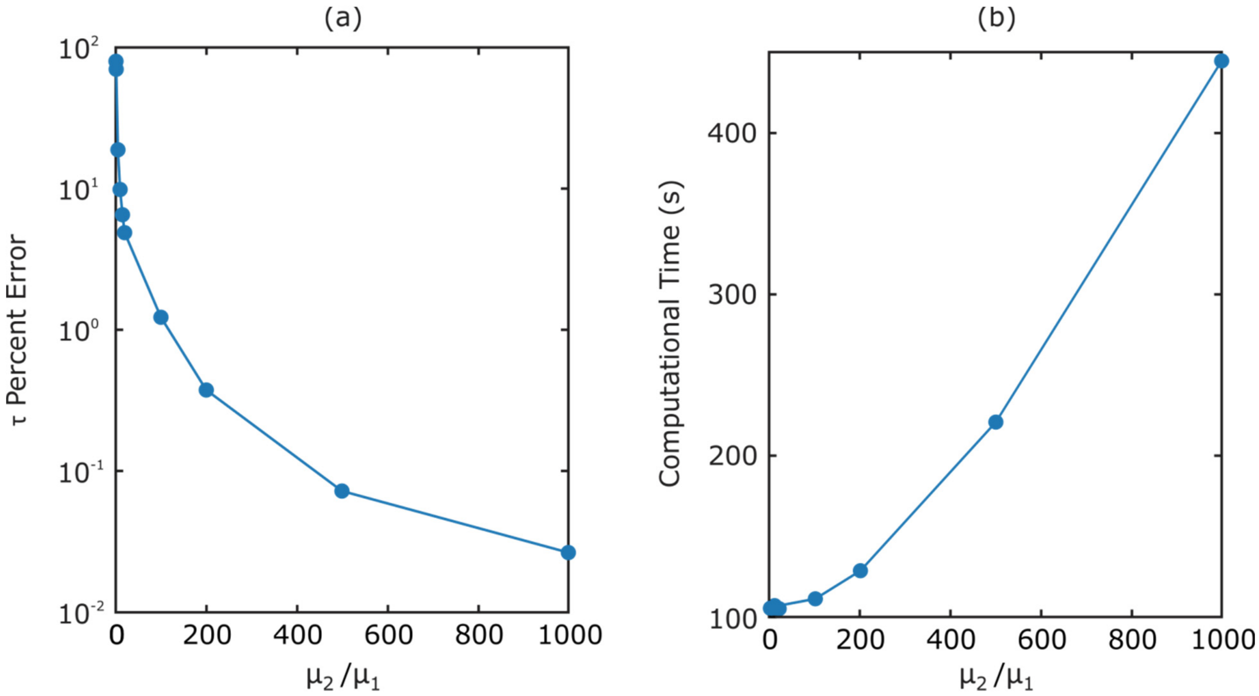

Figure A.4: (a) Error in measured τ and (b) computational time of simulation versus ratio of μ_2 to μ_1

all four cases error in elasticity measurements was less than 0.1%. Furthermore, all τ measurements were within 0.02 ms of the material τ with error in τ less than or equal to 2%.

Table A.1: Comparison of simulated and measured material parameters

Simulated Parameters				**Measured Parameters**	
μ_1 (kPa)	μ_2 (kPa)	η (Pa·s)	τ (ms)	μ_1 (kPa)	τ (ms)
5	1,000	1	0.20	5.000	0.2023
5	1,000	10	2.00	5.003	1.9890
100	20,000	1	0.01	100.000	0.0102
100	20,000	10	0.10	100.000	0.1010

A.5 Discussion and Conclusion

The aim of this chapter was to determine whether the Zener model can be used to simulate a Voigt material in LS-DYNA, and whether this model was valid over the range of material properties employed in this dissertation. These results suggest that as the stiffness of μ_2 increases, the creep response of the Zener model approaches that of the Voigt model as indicated by the decrease in τ error. Greater values of μ_2, however, require a smaller explicit time step, resulting in increased simulation computation times. This results in run times that are approximately 72% longer for the $\mu_2 = 200 \times \mu_1$ model than for $\mu_2 = 500 \times \mu_1$. Therefore, a $\mu_2 = 200 \times \mu_1$ was chosen for all materials.

The FEM material model presented in this chapter allows for the simulation of a Voigt material in response to an applied stress. This material model can be used in simulations of VisR ultrasound to simulate a Voigt material with density.

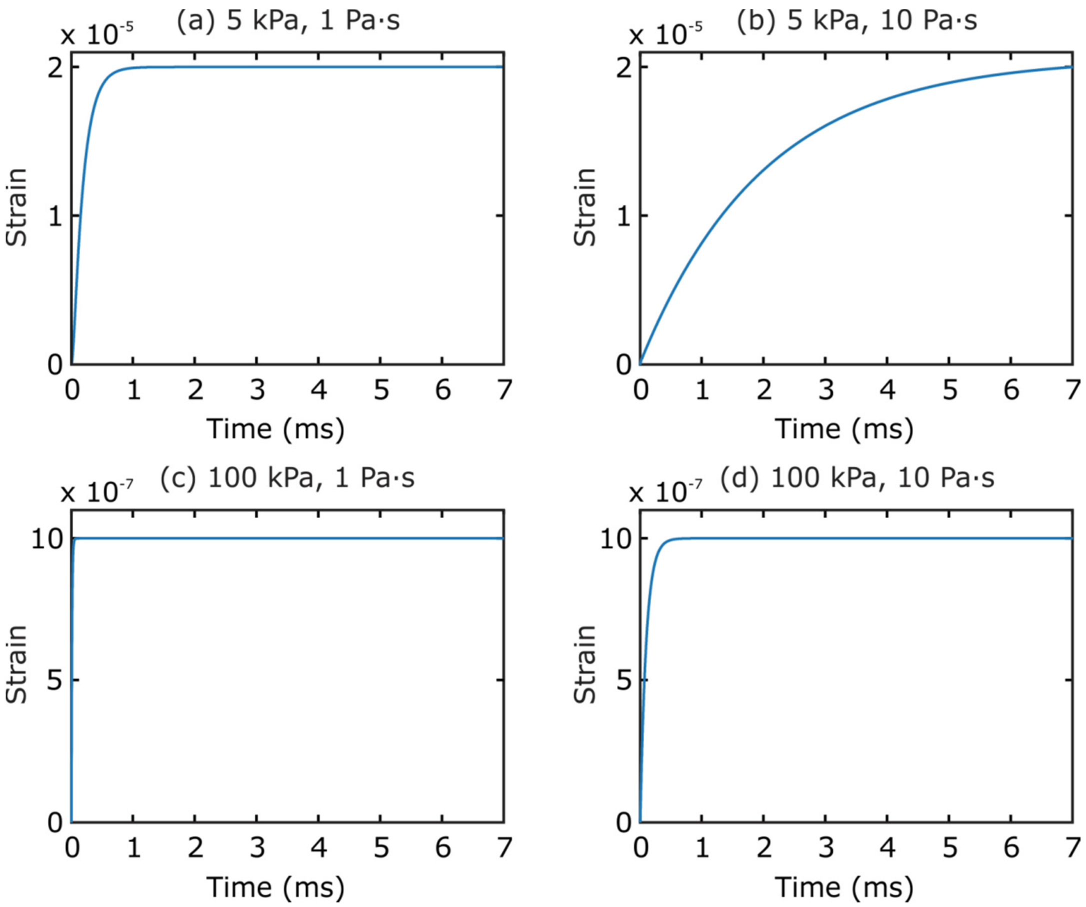

Figure A.5: Strain profiles for simulated materials under constant stress of 0.1 Pa. Materials were simulated with elasticities of 5 kPa (panels a & b) and 100 kPa (panels c & d) and viscosities of 1 Pa·s (panels a & c) and 10 Pa·s (panels b & c).

REFERENCES

1. Mendell, J. R., Sahenk, Z. & Prior, T. W. The Childhood Muscular Dystrophies: Diseases Sharing a Common Pathogenesis of Membrane Instability. *J. Child Neurol.* 10, 150–159 (1995).

2. Kornegay, J. N. *et al.* The Paradox of Muscle Hypertrophy in Muscular Dystrophy. *Phys. Med. Rehabil. Clin. N. Am.* 23, 149–172 (2012).

3. Bushby, K. *et al.* Diagnosis and management of Duchenne muscular dystrophy, part 1: diagnosis, and pharmacological and psychosocial management. *Lancet Neurol.* 9, 77–93 (2010).

4. Strober, J. B. Therapeutics in duchenne muscular dystrophy. *NeuroRx* 3, 225–34 (2006).

5. Mendell, J. R. *et al.* Challenges in drug development for muscle disease: a stakeholders' meeting. *Muscle Nerve* 35, 8–16 (2007).

6. Hall, J. E. *Guyton and Hall Textbook of Medical Physiology*. 71–82 (Saunders, 2011).

7. Petrof, B. J., Shrager, J. B., Stedman, H. H., Kelly, A. M. & Sweeney, H. L. Dystrophin protects the sarcolemma from stresses developed during muscle contraction. *Proc. Natl. Acad. Sci. U. S. A.* 90, 3710–3714 (1993).

8. Hill, J. A. & Olson, E. N. *Muscle: Fundamental Biology and Mechanisms of Disease*. 3–9 (Academic Press, 2012).

9. Kinali, M. *et al.* Muscle histology vs MRI in Duchenne muscular dystrophy. *Neurology* 76, 346–53 (2011).

10. Stone, M. H. *Principles and practice of resistance training*. (Human Kinetics, 2007).

11. Fukunaga, T., Kawakami, Y., Kuno, S., Funato, K. & Fukashiro, S. Muscle architecture and function in humans. *J. Biomech.* 30, 457–463 (1997).

12. Lieber, R. Skeletal muscle adaptability. I: Review of basic properties. *Dev. Med. Child Neurol.* (1986).

13. Morgan, J. E. & Partridge, T. A. Muscle satellite cells. *Int. J. Biochem. Cell Biol.* 35, 1151–1156 (2003).

14. Grounds, M. D. Towards understanding skeletal muscle regeneration. *Pathol. Res. Pract.* 187, 1–22 (1991).

15. Hoffman, E. P., Brown, R. H. & Kunkel, L. M. Dystrophin: the protein product of the Duchenne muscular dystrophy locus. *Cell* 51, 919–928 (1987).

16. Matsumura, K. & Campbell, K. Dystrophin–glycoprotein complex: its role in the molecular pathogenesis of muscular dystrophies. *Muscle Nerve* (1994).

17. Ervasti, J. M. & Sonnemann, K. J. Biology of the Striated Muscle Dystrophin-Glycoprotein Complex. *Int. Rev. Cytol.* 265, 191–225 (2008).

18. Rando, T. A. The dystrophin-glycoprotein copmlex, cellular signaling, and the regulation of cell survival in the muscular dystrophies. *Muscle and Nerve* 24, 1575–1594 (2001).

19. Dooley, J., Gordon, K. E., Dodds, L. & MacSween, J. Duchenne muscular dystrophy: a 30-year population-based incidence study. *Clin. Pediatr. (Phila).* 49, 177–9 (2010).

20. Lochmüller, H. & Bushby, K. Becker and Duchenne muscular dystrophy: a two-way information process for therapies. *J. Neurol. Neurosurg. Psychiatry* 85, 5–6 (2014).

21. Prior, T. W. & Bridgeman, S. J. Experience and strategy for the molecular testing of Duchenne muscular dystrophy. *J. Mol. Diagn.* 7, 317–326 (2005).

22. Jejurikar, S. S. & Kuzon, W. M. Satellite cell depletion in degenerative skeletal muscle. *Apoptosis* 8, 573–8 (2003).

23. Relaix, F. & Zammit, P. S. Satellite cells are essential for skeletal muscle regeneration: the cell on the edge returns centre stage. *Development* 139, 2845–2856 (2012).

24. Kunkel, L. & Hoffman, E. Duchenne/Becker muscular dystrophy: a short overview of the gene, the protein, and current diagnostics. *Br. Med. Bull.* 45, 630–643 (1989).

25. Haslett, J. N. *et al.* Gene expression comparison of biopsies from Duchenne muscular dystrophy (DMD) and normal skeletal muscle. *Proc. Natl. Acad. Sci. U. S. A.* 99, 15000–15005 (2002).

26. Bell, C. & Conen, P. Histopathological changes in Duchenne muscular dystrophy. *J. Neurol. Sci.* 529–544 (1968).

27. Holmes, G. *Pediatric Neurology.* 50–53 (Oxford University Press, 2010).

28. Manzur, a Y., Kinali, M. & Muntoni, F. Update on the management of Duchenne muscular dystrophy. *Arch. Dis. Child.* 93, 986–90 (2008).

29. Pearce, J. M. S., Pennington, R. J. T. & Walton, J. N. Serum enzyme studies in muscle disease: Part III Serum creatine kinase activity in relatives of patients with the Duchenne type of muscular dystrophy. *J. Neurol. Neurosurg. Psychiatry* 27, 181–185 (1964).

30. Zellweger, H. & Antonik, A. Newborn screening for Duchenne muscular dystrophy. *Pediatrics* 55, 30–34 (1975).

31. Ciafaloni, E. *et al.* Delayed Diagnosis in Duchenne Muscular Dystrophy: Data from the Muscular Dystrophy Surveillance, Tracking, and Research Network (MD STARnet). *J. Pediatr.* 155, 380–385 (2009).

32. Kakulas, B. a. Problems and potential for gene therapy in Duchenne muscular dystrophy. *Neuromuscul. Disord.* 7, 319–24 (1997).

33. Cros, D., Harnden, P., Pellissier, J. & Serratrice, G. Muscle hypertrophy in duchenne muscular dystrophy. *J. Neurol.* 43–47 (1989).

34. Brooke, M. H. *et al.* Clinical investigation in Duchenne dystrophy: 2. Determination of the "power" of therapeutic trials based on the natural history. *Muscle Nerve* 6, 91–103 (1983).

35. Vuillerot, C. *et al.* Monitoring changes and predicting loss of ambulation in Duchenne muscular dystrophy with the Motor Function Measure. *Dev. Med. Child Neurol.* 52, 60–5 (2010).

36. Moxley, R. T. *et al.* Practice parameter: corticosteroid treatment of Duchenne dystrophy: report of the Quality Standards Subcommittee of the American Academy of Neurology and the Practice Committee of the Child Neurology Society. *Neurology* 64, 13–20 (2005).

37. Moxley, R. T., Pandya, S., Ciafaloni, E., Fox, D. J. & Campbell, K. Change in natural history of Duchenne muscular dystrophy with long-term corticosteroid treatment: implications for management. *J. Child Neurol.* 25, 1116–29 (2010).

38. Bushby, K. *et al.* Diagnosis and management of Duchenne muscular dystrophy, part 2: implementation of multidisciplinary care. *Lancet Neurol.* 9, 177–89 (2010).

39. Gozal, D. Pulmonary manifestations of neuromuscular disease with special reference to Duchenne muscular dystrophy and spinal muscular atrophy. *Pediatr. Pulmonol.* 29, 141–150 (2000).

40. Finsterer, J. & Stöllberger, C. The heart in human dystrophinopathies. *Cardiology* 99, 1–19 (2003).

41. Eagle, M. *et al.* Survival in Duchenne muscular dystrophy: Improvements in life expectancy since 1967 and the impact of home nocturnal ventilation. *Neuromuscul. Disord.* 12, 926–929 (2002).

42. Prosser, E. J., Murphy, E. G. & Thompson, M. W. Intelligence and the gene for Duchenne muscular dystrophy. *Arch. Dis. Child.* 44, 221–30 (1969).

43. Cotton, S. M., Voudouris, N. J. & Greenwood, K. M. Association between intellectual functioning and age in children and young adults with Duchenne muscular dystrophy: further results from a meta-analysis. *Dev. Med. Child Neurol.* 47, 257–65 (2005).

44. Boland, B. J., Silbert, P. L., Groover, R. V., Wollan, P. C. & Silverstein, M. D. Skeletal, cardiac, and smooth muscle failure in Duchenne muscular dystrophy. *Pediatr. Neurol.* 14, 7–12 (1996).

45. Manzur, A., Kuntzer, T., Pike, M. & Swan, A. Glucocorticoid corticosteroids for Duchenne muscular dystrophy. *Cochrane Database Syst. Rev.* CD003725 (2008).

46. Mavrogeni, S. *et al.* Effect of deflazacort on cardiac and sternocleidomastoid muscles in Duchenne muscular dystrophy: a magnetic resonance imaging study. *Eur. J. Paediatr. Neurol.* 13, 34–40 (2009).

47. McNeil, D. E. *et al.* Duchenne muscular dystrophy: Drug development and regulatory considerations. *Muscle Nerve* 41, 740–5 (2010).

48. Fairclough, R. J., Wood, M. J. & Davies, K. E. Therapy for Duchenne muscular dystrophy: renewed optimism from genetic approaches. *Nat. Rev. Genet.* 14, 373–8 (2013).

49. Jarmin, S., Kymalainen, H., Popplewell, L. & Dickson, G. New developments in the use of gene therapy to treat Duchenne muscular dystrophy. *Expert Opin. Biol. Ther.* 14, 209–30 (2014).

50. Fairclough, R. J., Wood, M. J. & Davies, K. E. Therapy for Duchenne muscular dystrophy: renewed optimism from genetic approaches. *Nat. Rev. Genet.* 14, 373–8 (2013).

51. Pichavant, C. *et al.* Current status of pharmaceutical and genetic therapeutic approaches to treat DMD. *Mol. Ther.* 19, 830–40 (2011).

52. Rodino-Klapac, L. R., Mendell, J. R. & Sahenk, Z. Update on the treatment of Duchenne muscular dystrophy. *Curr. Neurol. Neurosci. Rep.* 13, 332 (2013).

53. Harris, J. & Slater, C. Animal models: what is their relevance to the pathogenesis of human muscular dystrophy? *Br. Med. Bull.* 36, 193–197 (1980).

54. Nakamura, A. & Takeda, S. Mammalian models of Duchenne Muscular Dystrophy: pathological characteristics and therapeutic applications. *J. Biomed. Biotechnol.* 2011, 1–8 (2011).

55. Blake, D. J., Weir, A., Newey, S. E. & Davies, K. E. Function and genetics of dystrophin and dystrophin-related proteins in muscle. *Physiol. Rev.* 82, 291–329 (2002).

56. Kornegay, J., Bogan, J. & Bogan, D. Canine models of Duchenne muscular dystrophy and their use in therapeutic strategies. *Mamm. Genome* 23, 85–108 (2012).

57. Kornegay, J. N., Tuler, S. M., Miller, D. M. & Levesque, D. C. Muscular dystrophy in a litter of golden retriever dogs. *Muscle Nerve* 11, 1056–64 (1988).

58. Childers, M. K. *et al.* Eccentric contraction injury in dystrophic canine muscle. *Arch. Phys. Med. Rehabil.* 83, 1572–1578 (2002).

59. Kornegay, J. N., Cundiff, D. D., Bogan, D. J., Bogan, J. R. & Okamura, C. S. The cranial sartorius muscle undergoes true hypertrophy in dogs with golden retriever muscular dystrophy. *Neuromuscul. Disord.* 13, 493–500 (2003).

60. Kornegay, J. N. *et al.* Contraction force generated by tarsal joint flexion and extension in dogs with golden retriever muscular dystrophy. *J. Neurol. Sci.* 166, 115–121 (1999).

61. Marsh, A. P., Eggebeen, J. D., Kornegay, J. N., Markert, C. D. & Childers, M. K. Kinematics of gait in golden retriever muscular dystrophy. *Neuromuscul. Disord.* 20, 16–20 (2010).

62. Ambrosio, C. E. *et al.* Identification of three distinguishable phenotypes in golden retriever muscular dystrophy. *Genet. Mol. Res.* 8, 389–396 (2009).

63. Mead, A. F. *et al.* Diaphragm remodeling and compensatory respiratory mechanics in a canine model of Duchenne muscular dystrophy. *J. Appl. Physiol.* 116, 807–15 (2014).

64. Kornegay, J. N. *et al.* NBD delivery improves the disease phenotype of the golden retriever model of Duchenne muscular dystrophy. *Skelet. Muscle* 4, 18 (2014).

65. DeVanna, J. C. *et al.* Respiratory dysfunction in unsedated dogs with golden retriever muscular dystrophy. *Neuromuscul. Disord.* 24, 63–73 (2014).

66. Sharp, N. J. *et al.* An error in dystrophin mRNA processing in golden retriever muscular dystrophy, an animal homologue of Duchenne muscular dystrophy. *Genomics* 13, 115–21 (1992).

67. Valentine, B. A. *et al.* Canine X-linked muscular dystrophy as an animal model of Duchenne muscular dystrophy: a review. *Am. J. Med. Genet.* 42, 352–356 (1992).

68. Mayhew, J. E. *et al.* Reliable surrogate outcome measures in multicenter clinical trials of Duchenne muscular dystrophy. *Muscle Nerve* 35, 36–42 (2007).

69. Jones & Stratton, G. Muscle function assessment in children. *Acta Paediatr.* 89, 753–61 (2000).

70. Helms, C. A., Major, N. M., Anderson, M. W., Kaplan, P. & Dussault, R. in *Musculoskelet. MRI* (Saunders, 2009).

71. Smith, R. & Newcombe, R. Assessment of locomotor function in young boys with Duchenne muscular dystrophy. *Muscle Nerve* 462–469 (1991).

72. Mendell, J. R. *et al.* Eteplirsen for the treatment of Duchenne muscular dystrophy. *Ann. Neurol.* 74, 637–47 (2013).

73. Geiger, R. *et al.* Six-minute walk test in children and adolescents. *J. Pediatr.* 150, 395–9, 399.e1–2 (2007).

74. Lynn, S. *et al.* Measuring clinical effectiveness of medicinal products for the treatment of duchenne muscular dystrophy. *Neuromuscul. Disord.* (2014).

75. McDonald, C. M. *et al.* The 6-minute walk test and other clinical endpoints in duchenne muscular dystrophy: reliability, concurrent validity, and minimal clinically important differences from a multicenter study. *Muscle Nerve* 48, 357–68 (2013).

76. Guyatt, G. H. *et al.* The 6-minute walk: A new measure of exercise capacity in patients with chronic heart failure. *Can. Med. Assoc. J.* 132, 919–921 (1985).

77. Govoni, A. *et al.* Ongoing therapeutic trials and outcome measures for Duchenne muscular dystrophy. *Cell. Mol. Life Sci.* 70, 4585–602 (2013).

78. Wu, B. *et al.* Exon skipping restores dystrophin expression, but fails to prevent disease progression in later stage dystrophic dko mice. *Gene Ther.* 1–9 (2014).

79. Stuberg, W. a & Metcalf, W. K. Reliability of quantitative muscle testing in healthy children and in children with Duchenne muscular dystrophy using a hand-held dynamometer. *Phys. Ther.* 68, 977–82 (1988).

80. Escolar, D. M. *et al.* Clinical evaluator reliability for quantitative and manual muscle testing measures of strength in children. *Muscle Nerve* 24, 787–93 (2001).

81. Henricson, E. K. *et al.* The cooperative international neuromuscular research group Duchenne natural history study: glucocorticoid treatment preserves clinically meaningful functional milestones and reduces rate of disease progression as measured by manual muscle testing and othe. *Muscle Nerve* 48, 55–67 (2013).

82. Fullerton, G. Magnetic resonance imaging signal concepts. *RadioGraphics* 579–596 (1987).

83. Plewes, D. B. & Kucharczyk, W. Physics of MRI: a primer. *J. Magn. Reson. Imaging* 35, 1038–54 (2012).

84. Keevil, S. Magnetic resonance imaging in medicine. *Phys. Educ.* 476, (2001).

85. Weber, M. *Magnetic Resonance Imaging of the Skeletal Musculature*. (Springer, 2014).

86. Garrood, P. *et al.* MR imaging in Duchenne muscular dystrophy: quantification of T1-weighted signal, contrast uptake, and the effects of exercise. *J. Magn. Reson. Imaging* 30, 1130–8 (2009).

87. Matsumura, K. *et al.* Proton spin-lattice relaxation time of Duchenne dystrophy skeletal muscle by magnetic resonance imaging. *Muscle Nerve* 11, 97–102 (1988).

88. Bryant, N. Noninvasive characterization of skeletal muscle damage and repair in murine models of muscular dystrophy. (2009).

89. McIntosh, L. M., Baker, R. E. & Anderson, J. E. Magnetic resonance imaging of regenerating and dystrophic mouse muscle. *Biochem. Cell Biol.* 76, 532–541 (1998).

90. Mathur, S. *et al.* Age-Related Differences in Lower-Limb Muscle Cross-Sectional Area and Torque Production in Boys With Duchenne Muscular Dystrophy. *Arch. Phys. Med. Rehabil.* 91, 1051–1058 (2010).

91. Akima, H. *et al.* Relationships of thigh muscle contractile and non-contractile tissue with function, strength, and age in boys with Duchenne muscular dystrophy. *Neuromuscul. Disord.* 22, 16–25 (2012).

92. Wang, J. *et al.* A computerized MRI biomarker quantification scheme for a canine model of Duchenne muscular dystrophy. *Int. J. Comput. Assist. Radiol. Surg.* (2013).

93. Fan, Z. *et al*. Characteristics of magnetic resonance imaging biomarkers in a natural history study of golden retriever muscular dystrophy. *Neuromuscul. Disord.* 24, 178–91 (2014).

94. Schulte-Uentrop, L. & Goepfert, M. S. Anaesthesia or sedation for MRI in children. *Curr. Opin. Anaesthesiol.* 23, 513–7 (2010).

95. Hayes, J., Veyckemans, F. & Bissonnette, B. Duchenne muscular dystrophy: an old anesthesia problem revisited. *Paediatr. Anaesth.* 18, 100–6 (2008).

96. Degardin, A. *et al*. Morphologic imaging in muscular dystrophies and inflammatory myopathies. *Skeletal Radiol.* 39, 1219–27 (2010).

97. Christensen, D. *Ultrasonic Bioinstrumentation*. (John Wiley & Sons, 1988).

98. Cobbold, R. S. C. *Foundations of Biomedical Ultrasound. Oxford Univ. Press* 45–51 (2007).

99. Jansen, M. *et al*. Quantitative muscle ultrasound is a promising longitudinal follow-up tool in Duchenne muscular dystrophy. *Neuromuscul. Disord.* 22, 306–17 (2012).

100. Zaidman, C. M., Connolly, A. M., Malkus, E. C., Florence, J. M. & Pestronk, A. Quantitative ultrasound using backscatter analysis in Duchenne and Becker muscular dystrophy. *Neuromuscul. Disord.* 20, 805–9 (2010).

101. Wallace, K. D. *et al*. Sensitive ultrasonic delineation of steroid treatment in living dystrophic mice with energy-based and entropy-based radio frequency signal processing. *IEEE Trans. Ultrason. Ferroelectr. Freq. Control* 54, 2291–9 (2007).

102. Hughes, M. S. *et al*. Sensitive ultrasonic detection of dystrophic skeletal muscle in patients with duchenne muscular dystrophy using an entropy-based signal receiver. *Ultrasound Med. Biol.* 33, 1236–43 (2007).

103. Greenleaf, J. F., Fatemi, M. & Insana, M. Selected methods for imaging elastic properties of biological tissues. *Annu. Rev. Biomed. Eng.* 5, 57–78 (2003).

104. Garra, B. S. Imaging and estimation of tissue elasticity by ultrasound. *Ultrasound Q.* 23, 255–268 (2007).

105. Drakonaki, E. E. & Allen, G. M. Magnetic resonance imaging, ultrasound and real-time ultrasound elastography of the thigh muscles in congenital muscle dystrophy. *Skeletal Radiol.* 391–396 (2010).

106. Greenleaf, J. F., Fatemi, M. & Insana, M. Selected methods for imaging elastic properties of biological tissues. *Annu. Rev. Biomed. Eng.* 5, 57–78 (2003).

107. Ophir, J. *et al*. Elastography: Ultrasonic estimation and imaging of the elastic properties of tissues. *Proc. Inst. Mech. Eng. Part H J. Eng. Med.* 213, 203–233 (1999).

108. Torr, G. R. The acoustic radiation force. *Am. J. Phys.* 52, 402 (1984).

109. Nightingale, K. R., Kornguth, P. J. & Trahey, G. E. The use of acoustic streaming in breast lesion diagnosis: a clinical study. *Ultrasound Med. Biol.* 25, 75–87 (1999).

110. Nightingale, K., Soo, M. S., Nightingale, R. & Trahey, G. Acoustic radiation force impulse imaging: In vivo demonstration of clinical feasibility. *Ultrasound Med. Biol.* 28, 227–235 (2002).

111. Palmeri, M. L., Sharma, A. C., Bouchard, R. R., Nightingale, R. W. & Nightingale, K. R. A finite-element method model of soft tissue response to impulsive acoustic radiation force. *IEEE Trans. Ultrason. Ferroelectr. Freq. Control* 52, 1699–712 (2005).

112. Palmeri, M. L., McAleavey, S. A., Fong, K. L., Trahey, G. E. & Nightingale, K. R. Dynamic mechanical response of elastic spherical inclusions to impulsive acoustic radiation force excitation. *IEEE Trans Ultrason Ferroelectr Freq Control* 53, 2065–2079 (2006).

113. Nightingale, K. Acoustic radiation force impulse (ARFI) imaging: a review. *Curr. Med. Imaging Rev.* 7, 328–339 (2011).

114. Meng, W. *et al.* Preliminary results of acoustic radiation force impulse (ARFI) ultrasound imaging of breast lesions. *Ultrasound Med. Biol.* 37, 1436–43 (2011).

115. Behler, R. H., Nichols, T. C., Zhu, H., Merricks, E. P. & Gallippi, C. M. ARFI imaging for noninvasive material characterization of atherosclerosis. Part II: toward in vivo characterization. *Ultrasound Med. Biol.* 35, 278–295 (2009).

116. Palmeri, M. L. *et al.* Acoustic radiation force impulse (ARFI) imaging of the gastrointestinal tract. *Ultrason Imaging* 27, 75–88 (2005).

117. Fahey, B. J. *et al.* In vivo visualization of abdominal malignancies with acoustic radiation force elastography. *Phys. Med. Biol.* 53, 279–293 (2008).

118. Zhai, L. *et al.* Acoustic Radiation Force Impulse Imaging of Human Prostates: Initial In Vivo Demonstration. *Ultrasound Med. Biol.* 38, 50–61 (2012).

119. Nightingale, K., Nightingale, R., Stutz, D. & Trahey, G. Acoustic radiation force impulse imaging of in vivo vastus medialis muscle under varying isometric load. *Ultrason. Imaging* 24, 100–108 (2002).

120. Sarvazyan, A. P., Rudenko, O. V, Swanson, S. D., Fowlkes, J. B. & Emelianov, S. Y. Shear wave elasticity imaging: a new ultrasonic technology of medical diagnostics. *Ultrasound Med Biol* 24, 1419–1435 (1998).

121. Bercoff, J., Tanter, M. & Fink, M. Supersonic shear imaging: a new technique for soft tissue elasticity mapping. *IEEE Trans Ultrason Ferroelectr Freq Control* 51, 396–409 (2004).

122. Athanasiou, A. *et al.* Breast lesions: quantitative elastography with supersonic shear imaging--preliminary results. *Radiology* 256, 297–303 (2010).

123. Wang, M. H. *et al.* In vivo quantification of liver stiffness in a rat model of hepatic fibrosis with acoustic radiation force. *Ultrasound Med. Biol.* 35, 1709–1721 (2009).

124. Arnal, B., Pernot, M. & Tanter, M. Monitoring of thermal therapy based on shear modulus changes: II. Shear wave imaging of thermal lesions. *IEEE Trans. Ultrason. Ferroelectr. Freq. Control* 58, 1603–1611 (2011).

125. Gennisson, J.-L., Catheline, S., Chaffaı¨, S. & Fink, M. Transient elastography in anisotropic medium: Application to the measurement of slow and fast shear wave speeds in muscles. *J. Acoust. Soc. Am.* 114, 536 (2003).

126. Lacourpaille, L. *et al.* Non-invasive assessment of muscle stiffness in patients with duchenne muscular dystrophy. *Muscle Nerve* 51, 284–6 (2015).

127. Dastgir, J. *et al.* P.13.9 Acoustic radiation force impulse imaging for the differentiation of muscle tissue stiffness in neuromuscular disorders. *Neuromuscul. Disord.* 23, 811 (2013).

128. Zhu, Y. *et al.* The Role of Viscosity Estimation for Oil-in-gelatin Phantom in Shear Wave Based Ultrasound Elastography. *Ultrasound Med. Biol.* 41, 601–9 (2015).

129. Chen, S. *et al.* Shearwave dispersion ultrasound vibrometry (SDUV) for measuring tissue elasticity and viscosity. *IEEE Trans. Ultrason. Ferroelectr. Freq. Control* 56, 55–62 (2009).

130. Catheline, S. *et al.* Measurement of viscoelastic properties of homogeneous soft solid using transient elastography: An inverse problem approach. *J. Acoust. Soc. Am.* 116, 3734–3741 (2004).

131. Deffieux, T., Montaldo, G., Tanter, M. & Fink, M. Shear wave spectroscopy for in vivo quantification of human soft tissues visco-elasticity. *IEEE Trans. Med. Imaging* 28, 313–22 (2009).

132. Chen, S., Fatemi, M. & Greenleaf, J. F. Quantifying elasticity and viscosity from measurement of shear wave speed dispersion. *J. Acoust. Soc. Am.* 115, 2781 (2004).

133. Mauldin, F. W. *et al.* Monitored steady-state excitation and recovery (MSSER) radiation force imaging using viscoelastic models. *IEEE Trans Ultrason Ferroelectr Freq Control* 55, 1597–1610 (2008).

134. Mainardi, F. & Spada, G. Creep, relaxation and viscosity properties for basic fractional models in rheology. *Eur. Phys. J. Spec. Top.* 193, 133–160 (2011).

135. Fung, Y. C. *Biomechanics: mechanical properties of living tissues*. (Springer-Verlag, 1993).

136. Gennisson, J.-L. *et al.* Viscoelastic and anisotropic mechanical properties of in vivo muscle tissue assessed by supersonic shear imaging. *Ultrasound Med. Biol.* 36, 789–801 (2010).

137. Aimedieu, P., Mitton, D., Faure, J. P., Denninger, L. & Lavaste, F. Dynamic stiffness and damping of porcine muscle specimens. *Med. Eng. Phys.* 25, 261; author reply 263 (2003).

138. Deffieux, T., Montaldo, G., Tanter, M. & Fink, M. Shear Wave Spectroscopy for In Vivo Quantification of Human Soft Tissues Visco-Elasticity. *IEEE Trans. Med. Imaging* 28, 313–322 (2009).

139. Pinton, G. F., Dahl, J. J. & Trahey, G. E. Rapid tracking of small displacements with ultrasound. *IEEE Trans. Ultrason. Ferroelectr. Freq. Control* 53, 1103–1117 (2006).

140. Bercoff, J., Tanter, M., Muller, M. & Fink, M. The role of viscosity in the impulse diffraction field of elastic waves induced by the acoustic radiation force. *IEEE Trans. Ultrason. Ferroelectr. Freq. Control* 51, 1523–36 (2004).

141. Cannon, M. S. & Puchalski, S. M. Ultrasonographic evaluation of normal canine iliopsoas muscle. *Vet Radiol Ultrasound* 49, 378–382 (2008).

142. Namani, R. *et al.* Elastic characterization of transversely isotropic soft materials by dynamic shear and asymmetric indentation. *J. Biomech. Eng.* 134, 061004 (2012).

143. Feng, Y., Okamoto, R. J., Namani, R., Genin, G. M. & Bayly, P. V. Measurements of mechanical anisotropy in brain tissue and implications for transversely isotropic material models of white matter. *J. Mech. Behav. Biomed. Mater.* 23, 117–132 (2013).

144. Cobbold, R. *Foundations of Biomedical Ultrasound.* (Oxford University Press, 2007).

145. Fahey, B. J., Nightingale, K. R., Wolf, P. D. & Trahey, G. E. ARFI imaging of thermal lesions in ex vivo and in vivo soft tissues. *IEEE Symp. Ultrason.* 562–567 (2003).

146. Nightingale, K., Soo, M. S., Nightingale, R. & Trahey, G. Acoustic radiation force impulse imaging: in vivo demonstration of clinical feasibility. *Ultrasound Med Biol* 28, 227–235 (2002).

147. Sharma, A., Soo, M., Trahey, G. E. & Nightingale, K. R. Acoustic radiation force impulse imaging of in vivo breast masses. *Proc. 2004 IEEE Ultrason. Symp.* 728–731 (2004).

148. Elegbe, E. C. & McAleavey, S. A. Single Tracking Location Methods Suppress Speckle Noise in Shear Wave Velocity Estimation. *Ultrason. Imaging* 35 , 109–125 (2013).

149. Hall, T. J., Bilgen, M., Insana, M. F. & Krouskop, T. A. Phlantom Materials for Elastography. *IEEE Trans. Ultrason. Ferroelectr. Freq. Control* 44, (1997).

150. Walker, W. F. & Trahey, G. E. A fundamental limit on delay estimation using partially correlated speckle signals. *IEEE Trans. Ultrason. Ferroelectr. Freq. Control* 42, 301–308 (1995).

151. Czernuszewicz, T. J., Streeter, J. E., Dayton, P. A. & Gallippi, C. M. Experimental validation of displacement underestimation in ARFI ultrasound. *Ultrason. Imaging* 35, 196–213 (2013).

152. Basu, U. Explicit finite element perfectly matched layer for transient three-dimensional elastic waves. *Int. J. Numer. Methods Eng.* 77, 151–176 (2009).

153. Jensen, J. A. & Svendsen, N. B. Calculation of pressure fields from arbitrarily shaped, apodized, and excited ultrasound transducers. *IEEE Trans. Ultrason. Ferroelectr. Freq. Control* 39, 262–267 (1992).

154. Arlot, S. & Celisse, A. A survey of cross-validation procedures for model selection. *Stat. Surv.* 4, 40–79 (2010).

155. Rouze, N. C., Wang, M. H., Palmeri, M. L. & Nightingale, K. R. Parameters affecting the resolution and accuracy of 2-D quantitative shear wave images. *IEEE Trans. Ultrason. Ferroelectr. Freq. Control* 59, 1729–1740 (2012).

156. Sarvazyan, A. P., Rudenko, O. V. & Nyborg, W. L. Biomedical applications of radiation force of ultrasound: Historical roots and physical basis. *Ultrasound Med. Biol.* 36, 1379–1394 (2010).

157. Palmeri, M. L., McAleavey, S. A., Trahey, G. E. & Nightingale, K. R. Ultrasonic tracking of acoustic radiation force-induced displacements in homogeneous media. *IEEE Trans. Ultrason. Ferroelectr. Freq. Control* 53, 1300–1313 (2006).

158. McAleavey, S. a, Nightingale, K. R. & Trahey, G. E. Estimates of echo correlation and measurement bias in acoustic radiation force impulse imaging. *IEEE Trans. Ultrason. Ferroelectr. Freq. Control* 50, 631–41 (2003).

159. Tsui, P.-H. *et al.* Use of nakagami statistics and empirical mode decomposition for ultrasound tissue characterization by a nonfocused transducer. *Ultrasound Med. Biol.* 35, 2055–68 (2009).

160. Ho, M. C. *et al.* Using ultrasound Nakagami imaging to assess liver fibrosis in rats. *Ultrasonics* 52, 215–222 (2012).

161. Cheung, J. Y., Bonventre, J. V, Malis, C. D. & Leaf, A. Calcium and ischemic injury. *N. Engl. J. Med.* 314, 1670–6 (1986).

162. Edwards, R. H., Newham, D. J., Jones, D. A. & Chapman, S. J. Role of mechanical damage in pathogenesis of proximal myopathy in man. *Lancet* 1, 548–552 (1984).

163. Hoffman, E., Jr, R. B. & Kunkel, L. Dystrophin: the protein product of the Duchenne muscular dystrophy locus. *Cell* 51, 919–928 (1987).

164. Deconinck, N. & Dan, B. Pathophysiology of Duchenne Muscular Dystrophy: Current Hypotheses. *Pediatr. Neurol.* 36, 1–7 (2007).

165. Rudenko, O. V. & Sarvazyan, a. P. Wave biomechanics of the skeletal muscle. *Acoust. Phys.* 52, 720–732 (2006).

166. Sharp, N. J. *et al.* An error in dystrophin mRNA processing in golden retriever muscular dystrophy, an animal homologue of Duchenne muscular dystrophy. *Genomics* 13, 115–121 (1992).

167. Behler, R. H., Nichols, T. C., Merricks, E. P. & Gallippi, C. M. A rigid wall approach to physiologic motion rejection in arterial radiation force imaging. *Proc. 2007 IEEE Ultrason. Symp.* 359–364 (2007).

168. Wang, J. *et al.* Statistical texture analysis based MRI quantification of Duchenne muscular dystrophy in a canine model. in *SPIE Med. Imaging* 8672, (International Society for Optics and Photonics, 2013).

169. Dubowitz, V. *Muscle biopsy: a modern approach.* (W. B. Saunders, 1973).

170. Brooke, M. H. *et al.* Clinical trial in Duchenne dystrophy. I. The design of the protocol. *Muscle Nerve* 4, 186–97 (1981).

171. Mayhew, J. E. *et al.* Reliable surrogate outcome measures in multicenter clinical trials of Duchenne muscular dystrophy. *Muscle Nerve* 35, 36–42 (2007).

172. Mazzone, E. *et al.* North Star Ambulatory Assessment, 6-minute walk test and timed items in ambulant boys with Duchenne muscular dystrophy. *Neuromuscul. Disord.* 20, 712–6 (2010).

173. Marden, F. a, Connolly, A. M., Siegel, M. J. & Rubin, D. a. Compositional analysis of muscle in boys with Duchenne muscular dystrophy using MR imaging. *Skeletal Radiol.* 34, 140–8 (2005).

174. Jones, D. A., Round, J. M., Edwards, R. H. T., Grindwood, S. R. & Tofts, P. S. Size and composition of the calf and quadriceps muscles in Duchenne muscular dystrophy: A tomographic and histochemical study. *J. Neurol. Sci.* 60, 307–322 (1983).

175. Torriani, M. *et al.* Lower leg muscle involvement in Duchenne muscular dystrophy: An MR imaging and spectroscopy study. *Skeletal Radiol.* 41, 437–445 (2012).

176. Forbes, S. C. *et al.* Magnetic Resonance Imaging and Spectroscopy Assessment of Lower Extremity Skeletal Muscles in Boys with Duchenne Muscular Dystrophy: A Multicenter Cross Sectional Study. *PLoS One* 9, e106435 (2014).

177. Henricson, E. *et al.* Percent-predicted 6-minute walk distance in duchenne muscular dystrophy to account for maturational influences. *PLoS Curr.* 4, RRN1297 (2012).